NTNU – Trondheim
Norwegian University of
Science and Technology

TEM Characterization of $LaFeO_3$ Thin Films on $SrTiO_3$ (111) Substrates

Emil Christiansen

MSc in Physics
Submission date: May 2015
Supervisor: Randi Holmestad, IFY

Norwegian University of Science and Technology
Department of Physics

Summary

In this thesis transmission electron microscopy (TEM) was used to study the atomic structure of $LaFeO_3$ (LFO) thin films grown on (111) oriented $SrTiO_3$ (STO) substrates by pulsed laser deposition. To prepare TEM samples both tripod polishing and focused ion beam (FIB) techniques were used, and samples of cross sectional (CS) and plan view (PV) geometries were studied. The films studied had a thickness of ≈ 20 nm, except for one which measured ≈ 55 nm. Tripod polishing yielded fair PV samples, but poor CS samples as the tripod is suspected of altering the film structure of these samples. FIB was used to prepare CS samples by lift-out, and to improve tripod PV samples. Even better TEM samples prepared by FIB than the ones studied in the present work are achievable, if more time can be devoted to TEM sample preparation.

By electron diffraction, dark field (DF) imaging, high resolution TEM (HRTEM), and scanning TEM (STEM) the LFO thin film is found to be orthorhombic, with one of the shorter unit cell vectors lying in the STO (111) plane (in-plane) and the other two axes pointing out of this plane. Because of the six-fold symmetry of the substrate surface, the film exhibits three distinguishable domains, labelled A, B, and C. These domains are equally likely to nucleate on the substrate and are found in equal shares. They have no regular shape or boundary, and range in sizes from some tens to some thousands square nanometres. Internal domain boundaries (IDBs) are found in A, B, and C domains alike, and are credited to the long orthorhombic $\vec{c}$ axis of two adjacent domains being antiparallel.

A set of straight lines following crystallographic directions of high symmetry is found. These lines are credited to the substrate, their origin might be due to surface polishing and eventual miscut effects. They are not found to affect A, B, and C domains differently, indeed no connection between these lines and domain configuration is observed.

The film is found to couple to the substrate in certain areas, causing an out-of-plane elongation of the substrate unit cell. In these disturbed areas the cubic symmetry is lost and the STO unit cell is thought to be rhombohedral, orthorhombic, or monoclinic. This effect is found where boundaries of orientational domains meet the substrate, which might be a way to engineer strain-induced properties for use in future devices.

Sammendrag

I denne masteroppgaven har transmisjonselektronmikroskopi (TEM) vært anvendt for å studere den atomære strukturen til $LaFeO_3$ (LFO) tynnfilmer grodd på (111) orienterte $SrTiO_3$ substrater ved hjelp av pulsertlaserdeponering (PLD). Tripodpolering og fokusert ionestråle (FIB) ble benyttet for å preparere TEM prøver. Både tverssnitt- og plane-prøver (CS og PV) ble studert. Tynnfilmene hadde en tykkelse på ≈ 20 nm, foruten en som hadde en tykkelse på ≈ 55 nm. Tripod polering gav tilfredsstillende plane prøver tatt i betrakting den enkle og billige metoden. Tverssnitts prøver derimot var mye vanskligere å preparere og kun en av disse ble tynn nok for TEM undersøkelser. Av denne tverrsnitts prøven ble det konkludert med at tripod polering kan påvirke filmens krystallstruktur. Ved å benytte FIB ble mye bedre tverrsnitts prøver oppnådd, med unntak av enkelte som ble ødelagt av ionestrålen. FIB ble også benyttet for å forbedre plane prøver. Det antas at enda bedre FIB prøver (både tverrsnitt og plane prøver) enn de som ble benyttet i denne oppgaven kan bli oppnådd.

Ved hjelp av elektron diffraksjon, mørkefelt (DF) avbildning, høyoppløsning TEM (HRTEM) og skanning TEM (STEM) ble LFO tynnfilmene funnet til å beholde sin orthorhombiske krystallstruktur. En av de korte aksene ble observert å ligge i $(111)_{STO}$ planet, mens de to andre aksene peker med ikke-rette vinkler ut av dette planet. Det ble funnet at denne orthorhombiske enhetscellen har tre observerbare måter å orientere seg på substratets overflate, hviklet skyldes dets seksfoldige symmetri. Disse tre orienteringene (domenene) ble kalt A, B og C, som hver har like muligheter for å dannes på substratets overflate. Formen på domenene er irregulære og det ble ikke funnet noen fast og bestemt grense mellom de tre. Størrelsen på domenene varierer fra noen få titalls kvadrat nanometer til flere tusener. Interne domene grenser (IDBs) ble observert i bde A, B, og C domener. Det er antatt at slike grenser skyldes en rotasjon p 180° om overflatenormalen.

Langs krystallografiske retninger av høy symmetri ble det funnet lange og rette streker. Disse strekene kan kun skyldes substratet, og det antas at de skyldes stegkanter indusert via feilskjæring av substratoverflaten. Ingen kobling mellom domenekonfigurasjon og stegkanter ble observert.

Tynnfilmene ble funnet å kople sterkt til substratet i visse områder, hvilket forårsaket en forlengelse av substratets enhetscelle ut av $(111)_{STO}$ planet. I disse områdene ble den kubiske sturkturen til STO tapt og enhetscellen antas å være rhobohedrisk, orthorhombisk eller monklinsk. Denne effekten blir sett i sammenheng med domenegrenser innad i tynnfilmen, og de resulterende trippelpunktene mellom grensene og substratet antas å være årsaken. De resulterende funksjonelle egenskapene i disse trippelpunktene forventes å være forskjellig fra bulk strukturene, og kan derfor ha mulige anvendelser innen teknologiske enheter i fremtiden.

Preface

This thesis is the product of my studies toward the degree of MSc in Physics at the Department of Physics of the Norwegian University of Science and Technology (NTNU). It is submitted as the conclusion of this degree. Two years have been spent on this work, starting August 2013 with May 2015 as the normed deadline. During the first year much time was divided to preparing samples and getting to know the newly installed NORTEM microscopes, as only 15 credits was spent on this thesis over this year. This last year a total of 45 credits has been divided to the work of this thesis.

I would like to thank Prof. Randi Holmestad for her guidance, patience and charismatic support. I am deeply grateful the opportunity to learn experimental material physics under her supervision. Furthermore I would like to thank Magnus Nord for his time spent assisting me in both sample prep. and TEM experiments. Without his help I would not have been able to achieve the results presented in this thesis. Thanks are due also to Adj. Assoc. Prof. Per Erik Vullum for his help in understanding the perovskite structure and his valuable advises regarding experimental work. Prof. Thomas Tybell is thanked for pushing me further by asking good and difficult questions. Ingrid Hallsteinsen is thanked for providing the films being studied and valuable insight into the growth mechanisms.

Additionally, I thank the people in the TEM group for their helpful discussions and their interest in my work. Their help has proven invaluable. My fellow students at the MSPHYS study programme are also thanked, for the companionship and discussions before and during the thesis work.

Emil Christiansen
NTNU, Trondheim
May 15th, 2015

Table of Contents

Abbreviations

ABF - **A**nnular **B**right **F**ield

ADF - **A**nnular **D**ark **F**ield

AFM - **A**nti **F**erro**m**agnetic

APB - **A**nti**p**hase **B**oundary

BF - **B**right **F**ield

CBED - **C**onvergent **B**eam **E**lectron **D**iffraction

CS - **C**ross **S**ection

CTF - **C**ontrast **T**ransfer **F**uction

CTR - **C**rystal **T**runcation **R**od (also referred to as ”relrod”)

DF - **D**ark **F**ield

DFT - **D**ensity **F**unctional **T**heory

DP - **D**iffraction **P**attern

DLF - **D**iamond **L**apping **F**ilm

EDP - **E**lectron **D**iffraction **P**attern

EDS - **E**nergy **D**ispersive **S**pectroscopy

EELS - **E**lectron **E**nergy **L**oss **S**pectroscopy

FEG - **F**ield **E**mission **G**un

FFT - **F**ast **F**ourier **T**ransform

FIB - **F**ocused **I**on **B**eam

FT - **F**ourier **T**ransform

FM - **F**erro**m**agnetic

GMR - **G**iant **M**agneto **R**esistance

HAADF - **H**igh **A**ngle **A**nnular **D**ark **F**ield

HRTEM - **H**igh **R**esolution **T**ransmission **E**lectron **M**icroscopy

IDB - **I**nternal **D**omain **B**oundary

LAO - **L**a**A**l$\mathbf{O}_3$

LFO - **L**a**F**e$\mathbf{O}_3$

LPMO - **L**a$_{0.55}$**P**b$_{0.45}$**M**n$\mathbf{O}_3$

LSMO - **L**a$_{0.7}$**S**r$_{0.3}$**M**n$\mathbf{O}_3$

MBE - **M**olecular **B**eam **E**pitaxy

NTNU - Norwegian University of Science and Technology (**N**orges **T**eknisk **N**aturvitenskapelige **U**niversitet)

PEEM - **P**hoto**e**lectron **E**mission **M**icroscopy

PV - **P**lan **V**iew

RHEED - **R**eflection **H**igh-**e**nergy **E**lectron **D**iffraction

SA - **S**elected **A**rea

SEM - **S**canning **E**lectron **M**icroscope

STEM - **S**canning **T**ransmission **E**lectron **M**icroscopy

STO - **S**r**T**i$\mathbf{O}_3$

TEM - **T**ransmission **E**lectron **M**icroscope/**M**icroscopy

VLM - **V**isible **L**ight **M**icroscope

WPOA - **W**eak **P**hase-**O**bject **A**pproximation

XMLD - **X**-ray **M**agnetic **L**inear **D**ichroism

XRD - **X**-ray **D**iffraction

Chapter 1

Introduction

Perovskite thin film heterostructures exhibit a wide variety of functional properties due to their great sensitivity to chemical composition and structural variation [1–6]. These materials consist of interfaces between two different materials that have chemical composition ABX_3 where A and B are cations and X is an anion, typically oxygen. $LaFeO_3$ (LFO) is an antiferromagnetic (AFM) perovskite which has shown to exhibit orientational domains when deposited as a thin film on (001) oriented $SrTiO_3$ (STO) substrates [7, 8]. The surface of (001) STO has a fourfold symmetry. Because the structure and symmetry of oxide thin films are closely related to the structure and symmetry of the substrate, it is believed that the sixfold symmetry of (111) oriented STO will affect the properties of the film. This orientation is also suspected to cause a closer coupling between film and substrate. In this thesis thin films of epitaxial LFO on (111) oriented STO substrates grown by pulsed laser deposition (PLD) have been studied by transmission electron microscopy (TEM). High resolution TEM (HRTEM), dark field (DF) imaging, electron diffraction studies, and scanning TEM (STEM) were used to investigate the structure. To prepare samples for TEM studies several techniques have been applied, tripod polishing and focused ion beam (FIB) milling being the most important. Both cross sectional (CS) and plan view (PV) TEM samples have been studied and compared.

1.1 Motivation

Today's society is heavily based on computer and information technology. Modern movies, images, music, and books all rely on the benefits and tools computers offer. Almost instant communication across the globe with all its upsides and downsides would not be possible without computers. The number of ways modern computer and information technology affects today's society is therefore vast. However, the part computers have played in the advancement of science can not be overestimated. Every great scientific feat in the last decades have applied computer technology in some way or another. One example is the discovery of the Higgs Boson in 2012, where vast amounts of data needed to be acquired,

analysed, stored, interpreted and so on. This would have been impossible without the powerful computing power offered by modern computers and technology. Indeed the design of the experiment would have been impossible without computers. Further development of digital devices and computers is therefore expected to be of importance in nearly all fields of society.

Central to the development of computers and electronic devices is the field of materials science. Especially semiconductors have been important since they are the basis for conventional transistors. The invention of the transistor by Bardeen, Brattain, and Shockley in 1947 is what made today's computers possible. In a way this discovery can be considered as the most important technological breakthrough in the 20th century. Along with this discovery the extensive study and production of single crystalline silicon has driven materials science and nano technology to new levels. The statement by Gordon E. Moore that the number of components per integrated circuit doubles every two years has been named Moore's law, and proven to be mostly correct so far. This statement can be applied to the evolution of memory devices as well, which plays a vital role in the development of computers. However semiconductor electronics is believed to soon reach fundamental limits, and new materials systems must be explored.

Electroceramic materials, as discussed by Setter and Wasser [9], show great promise as successors to conventional semiconductor devices. These materials exhibit a range of dielectric, magnetic, semiconducting, superconducting, and ionically conducting properties, and have applications as e.g. non-volatile, fast and power efficient memory devices. A new generation of devices has been born with the field of spintronics, in which electroceramic materials play a vital role. Spintronic devices are devices which are sensitive to the spin of the electrons flowing as current [10, 11]. The giant magneto resistance (GMR) [12] effect plays a vital role for such devices. This is an effect that causes the electrical resistance between two ferromagnets separated by a thin insulating layer to be dependent on the relative orientation of their magnetic moments. In essence the effect can be explained by the density of states available for the electrons passing as current, as illustrated in Fig. 1.1. If the magnetic moments of the ferromagnets are anti-parallel there will not be enough states for all the electrons of one side to tunnel over to the other, thus reducing the current.

A spin valve is one example of an application of the GMR. It can be engineered by having a non-magnetic material sandwiched between two ferromagnetic materials, one of which must be made relatively insensitive to external magnetic fields (pinning). To achieve this pinning an AFM material can be introduced as a fourth layer on top of one of the ferromagnetic layers as illustrated in Fig. 1.2. This has the effect of shifting the magnetic curve of the ferromagnet, called exchange bias [13]. The magnetic moment in the unpinned ferromagnet can be switched, and when this moment is parallel to that of the pinned layer, the resistance through the device is low. If the moment is anti-parallel however, the resistance is typically $\sim 5-10\%$ higher. Such spin-valves are today used as read heads in hard disks and as magnetoresistive random access memory (MRAM) [10].

The synthesis of devices such as a spin valve involves advanced materials science. For the

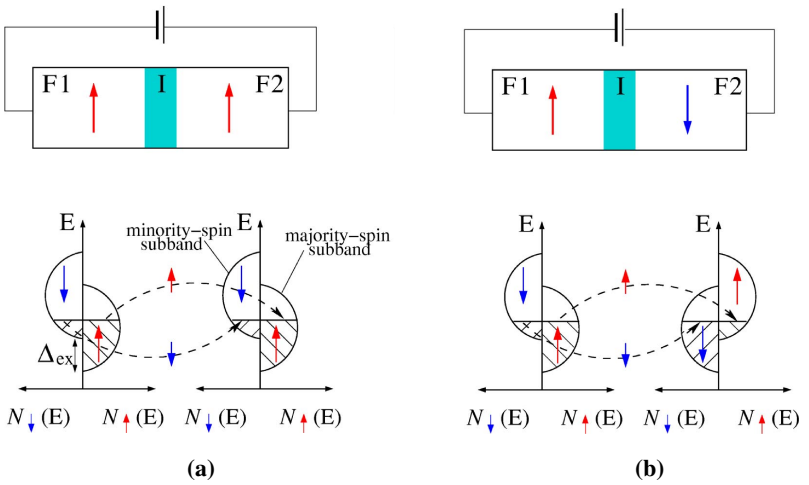

(a) **(b)**

Figure 1.1: Illustration of the GMR effect. In both drawings a circuit with a ferromagnet-insulator-ferromagnet (marked F1, I, and F2) device is presented. The insulating layer is thin, so tunnelling may occur from one side to the other. The ferromagnets in the device presented in a) the left have parallel moments, while the device in b) have anti-parallel ones. E is the energy of the electrons, and $N\,(E)$ is the number of electrons allowed with energy E and spin indicated by the arrow. If the magnetic moments of the two ferromagnets are parallel (a), the density of states for electrons are equal on both sides. If however the magnetic moments are anti-parallel (b) there will not be enough states for the all the electrons with spin e.g. up at one side to accept all the electrons from the other, and a reduced current will flow. From [11].

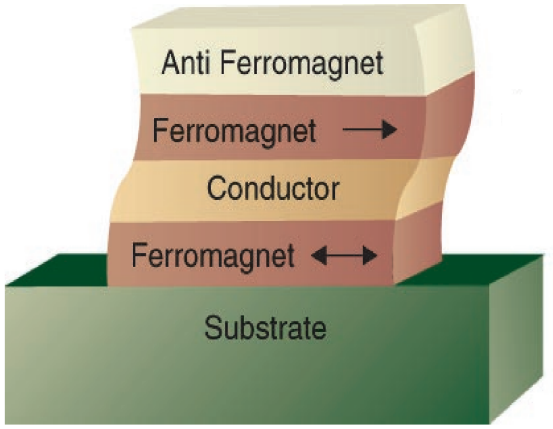

Figure 1.2: Schematic of a spin valve. From [10].

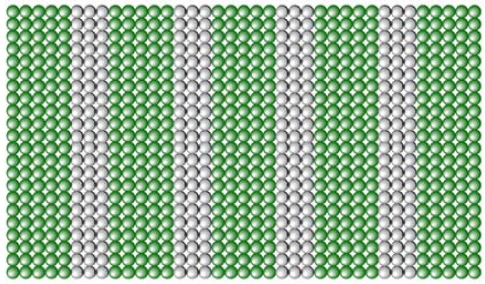

Figure 1.3: Illustration of a multilayer with atomically sharp interfaces. Green and white spheres mark lattice sites of each material. Taken from [12].

GMR to be achieved, the contact interfaces between the layers must be nearly perfect on an atomic scale. This means that the layers exhibiting different properties must be grown epitaxially on a substrate. Epitaxial growth is the process of depositing layers on top of a substrate in such a way that the atoms of the layers have the same atomic structure as the substrate, as illustrated in Fig. 1.3. One generally wishes to keep the resulting film to be as thin as possible as the interface of such thin structures is easier to control, and the relevant application of such a layer requires it to be thin [13]. To achieve epitaxial thin films the bulk atomic structure of the various layers must be somewhat similar and advanced synthesis techniques must be applied. Some of the most used growth techniques are PLD, molecular beam epitaxy (MBE), and off-axis radio frequency magnetron sputtering. The task then is to find materials of similar structure but with greatly different functional properties. One group of materials that are promising in this regard are the perovskites. Several functional properties are found in this group of materials, with relatively little difference in atomic structure. LFO is an anti ferromagnetic perovskite which forms structural domains (grains) when grown on different substrates [7, 8]. Such LFO thin films also form AFM domains. The exchange bias achieved by an AFM layer is greatly dependent on the domain structure of the film, in some cases large grains increase the shift, while in other cases this reduce the shift. In the study by Seo et. al. LFO thin films with small grain size were found to provide a larger exchange bias [8].

The magnetic properties of a material is intimately connected with its electronic structure which in turn is decided by crystal structure and chemistry. Structural domains and grain boundaries have been seen to affect the magnetotransport in ferromagnetic oxides to a large degree [14]. For $La0.7Sr_{0.3}MnO_3$ (LSMO) thin films there have been found several ways to control the thin film structure, and thus to tailor its ferromagnetic property [15–18]. Some of these ways include growing the films on substrates of different crystal orientation. It is therefore expected that the six-fold symmetry of the (111) plane of STO will influence LFO thin films if deposited epitaxially on such substrates, and that new insight into the orbital structure of LFO can be gained.

Prof. Thomas Tybell at NTNU and his team of researchers are leading in the field of oxide thin film synthesis. They are able to grow thin LFO and LSMO films on (111) oriented

STO, which are materials where, at least in the case of LFO, little published work exist [16, 19, 20]. It has been observed that the metal-insulator transition temperature of bilayers of $La_{0.55}Pb_{0.45}MnO_3$ (LPMO)/LFO on $LaAlO_3$-Sr_2AlTaO_6 increases when grown on (111) oriented substrates rather than (001). This increase was attributed to the enhanced pinning of the ferromagnetic moments in the LPMO layer due to the uncompensated AFM moments of the LFO buffer layer. Tybells group is interested in examining the orbital configuration of LFO films grown on (111) STO and to apply this in e.g. LSMO/LFO multilayers. The creation of embedded nanostructures in such multilayers are also of interest [17, 18]. In order to elucidate the orbital configuration of such structures an increased understanding of the structural aspects of LFO/STO (111) thin films is required. A close partnership with the TEM Gemini Centre at NTNU lead by Prof. Randi Holmestad has been initiated to aid in this endeavour, as the TEM is an excellent tool for probing the atomic structure of these films. To gain an increased understanding of the atomic structure of LFO/STO (111) thin films of ≈ 20 nm thickness (which in turn may lead to an increased understanding of the orbital configuration in such systems), this thesis seeks to reveal the structure of these films by TEM.

1.2 Outline

In order to appreciate both the methods and the results of this thesis, an introduction to relevant theory is presented in Chapter 2. Here the concept of crystals is explained and how they may be observed/characterized by diffraction. Next follows a detailed presentation of the structure of LFO and its functional properties. The reciprocal lattice of LFO, and how it relates to that of STO by assuming bulk LFO parameters, is described in detail. Next a presentation of the microscope structure and design is presented. Finally, the imaging techniques used in this thesis are introduced and explained.

Chapter 3 concerns the experimental procedure applied in this thesis. It begins by introducing the naming system and the samples studied before it explains the synthesis of the thin films. A detailed explanation of the TEM sample preparation follows, where images acquired during the processes are presented. Due to the extensive and somewhat complicated preparation techniques this section contain a lot of information and images. This is in order to give a clear picture of how TEM samples were prepared and how the different sample geometries are achieved, as well as providing a recipe for those who want to repeat the procedures. After this section, the methods and instruments used in the actual TEM experiments are presented and explained.

Chapter 4 presents and discusses the results acquired by TEM experiments. To promote the important aspects of the results, it was deemed best to present non-crucial, but supporting, results in a separate appendix (Appendix C). The presentation and discussion of the results starts with some comments on sample preparation, with the intention of passing on useful tricks and experiences for future work. Next results regarding the various attributes of ”step lines” (note that this is not necessarily actual step lines induced by substrate miscuts), film structure and quality, and domain structure are presented and discussed simultaneously.

A conclusion based on the results and discussion is made in Chapter 5, where the main points regarding sample preparation is concluded on first. Concluding remarks on film quality and domain structure are given afterwards.

Finally, in Chapter 6 further work is suggested in light of the discussion and conclusions made by this thesis.

Chapter 2

Theory

The physics of electroceramic thin films is advanced and extensive. This chapter begins by giving an introduction to crystals and diffraction, before presenting the structure and functional properties of LFO. Lastly, it presents the basic theory and applications of TEM necessary to appreciate the results presented in later chapters.

2.1 Crystals and diffraction

This section is heavily based on [21–26], therefore citations to these works are omitted through this section.

Crystal are a form of solid state where the atoms constitute a highly periodic array. The periodicity of an ideal crystal is represented mathematically by an infinite lattice, called a Bravais lattice. The Bravais lattice is not a crystal by itself, but by associating a basis with each lattice site the ideal crystal is achieved, called the crystal structure. This can be done through the convolution of a basis and the crystal lattice. The basis can be as simple as a single atom, molecule or particle, or a vast collection of objects (such as a protein).

A Bravais lattice is defined by the lattice vector $\vec{R}$

$$\vec{R} = u\vec{a} + v\vec{b} + w\vec{c}, \tag{2.1}$$

with $u, v, w \in \mathbb{Z}$. The vectors $\vec{a}$, $\vec{b}$, and $\vec{c}$, with lengths of a, b, and c respectively[1], are called primitive basis vectors, and are not allowed to be parallel or in the same plane. Together these primitive basis vectors span the primitive unit cell of the lattice which encloses exactly one lattice point, but is not unique as Fig. 2.1 illustrates. Other unit cells may be defined as well, and by convention the one which best reflects the symmetry of the lattice is used. The conventional unit cells used for the different Bravais lattices are

[1]The following convention is accepted for the angles between lattice vectors $\vec{a}\angle\vec{b} = \gamma$, $\vec{b}\angle\vec{c} = \alpha$, and $\vec{a}\angle\vec{c} = \beta$.

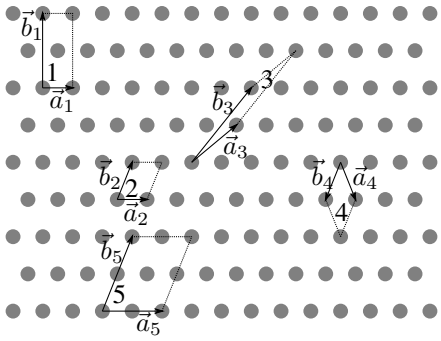

Figure 2.1: Illustration of some different choices of basis vectors for a centred rhombic 2D Bravais lattice, the subscripts of the vectors denotes unit cell no. 1, 2 and so on. The complete outline of each unit cell is shown as dotted lines. The first unit cell is the conventional unit cell for this lattice, showing how this lattice actually is a rectangular one (planar group number 5, cm). Unit cells 2, 3, and 4 illustrate some different possibilities of primitive unit cells, as only one lattice point is included in the interior. Unit cell 5 shows how one may extend unit cell 2 to a larger unit cell. While equivalent, unit cell 2 is preferred over unit cell 5 as the representation becomes simpler.

presented in Table 2.1. The Bravais lattice's definition makes it invariant under translation of an integer linear combination of the basis vectors. Because of this, only certain other symmetry operations are possible for any Bravais lattice[2]. In $2\mathbb{D}$ these operations are the point symmetry operations of 1-, 2-, 3-, 4- or 6-fold rotation, mirroring ("m") or inversion (denoted as a bar¯). In $3\mathbb{D}$ there are the additional operations of screw axes and glide planes, which are constructed through combinations of translation with mirroring and rotation. When a lattice is invariant under a group of symmetry operations, we say that it belongs to a planar or space group ($2\mathbb{D}$ and $3\mathbb{D}$ respectively)[3]. As indicated in Table 2.1, there are only 32 planar groups and 230 space groups. With increasing temperature a crystal structure will go through first order phase transitions to space groups of increasing symmetry, unless it melts.

Directions and lattice planes in a crystal are expressed through a set of indices called the Miller indices[5] h, k, and l. A lattice plane is a plane that will, when parallel translated through the entire crystal, contain all the lattice points in the crystal. When given in a normal parenthesis, (hkl), these indices represent the reciprocal intersection made by a plane with the unit cell axes. The plane (112) for instance is a plane that intersects the crystal axes a, b, and c at the fractional coordinates $1/1$, $1/1$ and $1/2$ respectively. For

[2]Physical objects not exhibiting the translational symmetry of Bravais lattices, but are periodic and ordered in some other way are called Quasicrystals, and can exhibit different symmetries, such as 5-fold symmetry (e.g. Penrose tilings)

[3]The word group is here used in its proper mathematical meaning as such a group would exhibit closure and associativity, and contain an inverse element and an identity element.

[4]7 from the rhombohedral **lattice** system and 18 from the hexagonal **lattice** system.

[5]Sometimes a fourth index $i = -(h + k)$ is introduced for hexagonal lattices, and the term Miller-Bravais indices is used

Table 2.1: Overview of the different crystal systems, their Bravais lattices and their number of different point/space groups [27].

System	Axes	Unit cell	#PGs	#SGs
Cubic	$a = b = c$ $\alpha = \beta = \gamma = 90°$	P, I, F	5	36
Tetragonal	$a = b \neq c$ $\alpha = \beta = \gamma = 90°$	P, I	7	68
Orthorhombic	$a \neq b \neq c$ $\alpha = \beta = \gamma = 90°$	P, I, F, C	3	59
Trigonal/Rombohedral	$a = b = c$ $\alpha = \beta = \gamma \neq 90°$	P	5	25[4]
Hexagonal	$a = b \neq c$ $\alpha = \beta = 90°, \gamma = 120°$	P	7	27
Monoclinic	$a \neq b \neq c$ $\alpha = \gamma = 90° \neq \beta$	P, C	3	13
Triclinic	$a \neq b \neq c$ $\alpha \neq \beta \neq \gamma \neq 90°$	P	2	2

directions the notation of $[UVW] \equiv U\vec{a} + V\vec{b} + W\vec{c}$ is used. It is only in cubic crystal systems that the direction $[hkl]$ always will be orthogonal to the plane (hkl), and for other crystal systems care must be taken when considering directions and planes. Negative values are usually represented as a bar ($\bar{x}$). A zone axis is a crystallographic direction that is perpendicular to the normals of at least two different planes. The distance d_{hkl} defined as the distance from the unit cell origin and the (hkl) plane in a crystal system with right angles, is given by

$$\frac{1}{d_{hkl}} = \pm\sqrt{\frac{h^2}{a^2} + \frac{k^2}{b^2} + \frac{l^2}{c^2}}. \tag{2.2}$$

For other crystal systems the expression for d becomes more complicated. It is obvious that the distance d of a plane having Miller indices $(2h2k2l)$ is twice that of the plane with miller indices (hkl). The distance between such two planes is therefore d.

The reciprocal lattice of a crystal is a very powerful tool. It can be defined as the points spanned by the set of vectors

$$\vec{G} = u^*\vec{a}^* + v^*\vec{b}^* + w^*\vec{c}^*, \tag{2.3}$$

with coefficients u^*, v^*, and w^* that span $\mathbb{Z}$. The vectors $\vec{a}^*$, $\vec{b}^*$, and $\vec{c}^*$ are defined[6] by

$$\vec{a}^* = 2\pi \frac{\vec{b} \times \vec{c}}{V_E}$$
$$\vec{b}^* = 2\pi \frac{\vec{c} \times \vec{a}}{V_E}$$
$$\vec{c}^* = 2\pi \frac{\vec{a} \times \vec{b}}{V_E}$$

where V_E is the volume of the unit cell in real space. The vectors defined by Equation 2.3 are called the reciprocal lattice vectors, and create points in what is known as the reciprocal space. It is important to be aware that it is only in systems where $\alpha = \beta = \gamma = 90°$ that the reciprocal unit vectors will be parallel to their real-space counterparts. Through simple geometric arguments it can be shown that a reciprocal lattice vector with $[u^*, v^*, c^*] = [h, k, l]$ is perpendicular to the plane (hkl) and its length will be

$$\left\| \vec{G}_{hkl} \right\| = \frac{2\pi}{d_{hkl}}. \tag{2.4}$$

Each point in the reciprocal lattice thus represents a unique plane and can be considered as a spatial frequency in the structure. The reciprocal lattice defined in this way is actually the Fourier Transform (FT) of the crystal lattice, making it an incredibly efficient tool when combined with the convolution theorem of Fourier analysis.

A real physical crystal cannot be infinite, as the Bravais lattice is. Hence the real structure of a physical crystal will be described by the convolution between the Bravais lattice with the basis, multiplied with a step function to truncate the infinite structure. In accordance with general Fourier analysis, an object that is localized (i.e. ”small”) in real space, is smeared out in reciprocal space. Therefore the points in the reciprocal space of a real crystal are smeared out, especially if the crystal is ”thin” in some direction. In materials science these ”smeared-out” points are called crystal truncation rods (CTRs) or rel-rods. How far a CTR extends from a reciprocal lattice point is dependent on how the crystal is truncated. The CTRs of an infinite $3\mathbb{D}$ crystal in the shape of a single atomic sheet, will be very long and thin rods perpendicular to the sheet. As will be explained in the TEM section, a TEM sample must be very thin in order to be electron transparent. This causes CTRs to be formed, which is decisive to TEM operation.

2.1.1 Crystal defects

A real crystal will contain some defects. Local defects caused by missing (vacancy) or extra (interstitial) atoms are called point defects. These effects cause a local disturbance

[6] Two different conventions live side by side. In this thesis the factor 2π is included, but in other work this might be omitted

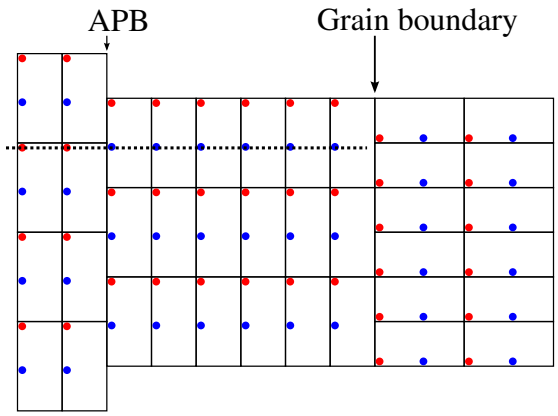

Figure 2.2: Illustration an APB and a grain boundary as planar defects. The rectangles signify unit cells, with the red and blue dots corresponding to atoms or basis sites. The APB occurs when the unit cell of one part of the grain are shifted $1/2$ unit cell with respect to the other. When following the dotted line from left to right one will encounter red-red-blue-blue-blue... dots, illustrating that the sides of the boundary are out of phase. The grain boundary is due to the different orientation of adjacent unit cells.

in the crystal lattice and are of crucial importance for e.g. solar cells [28]. When such vacancies are ordered, superstructures within a crystal may be achieved, such as the Brownmillerite phase which is applicable in e.g. fuel cells [29]. Line defects are extended dislocations such as the termination of a lattice plane within the crystal.

Planar defects are another kind of irregularity that can be present in a real crystal. Such defects include grain boundaries, antiphase boundaries (APBs) and stacking faults. In Fig. 2.2 a simple illustration of both grain boundaries and APBs is presented. A crystalline material may consist of several grains, each of which have a crystallographic orientation that is different from its neighbouring grains. This causes grain boundaries to appear between them, where a discontinuity in crystal orientation takes place. APBs occur within a single grain, and are usually due to a shift of $1/2$ unit cell of one side with respect to the other side of the boundary.

2.2 Perovskites and $LaFeO_3$ - crystallography and functional properties

Functional materials (also called smart materials) are materials where an external stimuli causes a change in the material's physical properties. A prime example are piezoelectric materials where an applied stress to the material produces an electric field within the material. According to the Neumann principle [30] a macroscopic property of a crystal cannot have a higher symmetry than the unit cell itself, and to understand the properties of a material it is necessary to understand its structure. As mentioned in the introduction

LFO has AFM properties and therefore a brief presentation of magnetism is given before the structure of LFO is explained in detail.

2.2.1 Magnetism

Some of the properties of functional materials are connected with the spatial order of atoms, while other properties are due to an even more subtle order within the material [30]. Magnetism is an example of such a property. Magnetic materials are materials where there exist some kind of order between the spins of the atoms, yielding a magnetic flux density of

$$\vec{B} = \mu\vec{H} = \mu_0\vec{H} + \vec{M},$$

where $\vec{H}$ is an external magnetic field, μ_0 the free space permeability and $\vec{M}$ is the magnetization of the material. The magnetic susceptibility χ couples $\vec{M}$ to $\vec{H}$ by $\vec{M} = \chi\vec{H}$ so that the magnetic permeability of a material is given as $\mu = \mu_0(1+\chi)$. Diamagnetic materials are materials with $\mu < 1$. Electrons of the atoms in such a material seek to counter an externally applied magnetic field. Paramagnetism is present in materials with a permeability larger than 1, meaning that the spins of electrons align with the applied field. The susceptibility of a paramagnetic material follows Curie's law $\chi \propto 1/T$, where T is temperature. Both dia- and paramagnetism require an externally applied field to be observed, and are relatively weak effects.

Ferromagnetic (FM) materials are materials that will contain a spontaneous magnetic field even when no external magnetic field is applied. This means that the relationship between $\vec{B}$ and $\vec{H}$ is not linear, and FM is a much stronger effect than dia and para magnetism. The response of such a material follows a hysteresis loop, such as the one in Fig. 2.3. A remnant field $\vec{B}_r$ is present at $H = 0$, and $\vec{B} = 0$ at the coercive field $\vec{H}_c$. FM is an order-disorder effect present below a certain material specific temperature T_C called the Curie temperature. Below this temperature the unpaired electrons of nearby atoms align, adding up to a macroscopic magnetic moment. When the temperature is increased above T_C the material undergoes a second order phase transition and the alignment of electrons is lost. The magnetic field of a macroscopic FM slab will be zero, as the slab will orient the magnetic field of different regions (magnetic domains) to cancel each other. By applying an external field the volume distribution of the different magnetic domains will be shifted in favour of the applied field. After the external field is turned off the material will require time to reorient its domains.

Another magnetic phase, which has for many years been of little interest, is the anti ferromagnetic (AFM) phase. With the discovery of the GMR effect, renewed interest in this phase has taken place. The spins of neighbouring atoms in an AFM are opposite, creating a spin sub-lattice as in Fig. 2.4. The ordered spin sub-lattice is usually due to orbital overlap between some atoms via an intermediate atom (super exchange). The theory behind AFM materials is quite complex, but the magnetic susceptibility of such materials is of the form [30]

$$\chi = \frac{2CT - 2\alpha C^2}{T^2 - T_N^2}\mu_0,$$

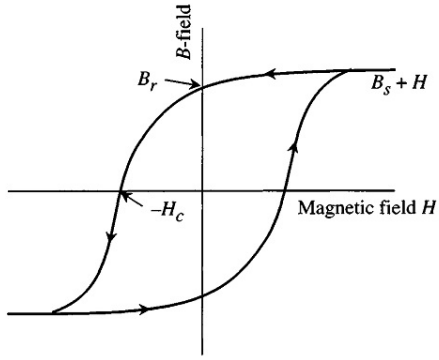

Figure 2.3: Typical hysteresis loop of a FM material. Applying an external magnetic field H produces a magnetic flux density B. The magnetization of the material saturates at a certain H, and a remnant field B_r persists even after the applied field is turned off. The coercive field H_c is the field required to produce $B = 0$. The slope of the loop gives the magnetic susceptibility of the material. From [30].

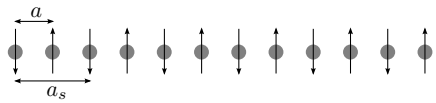

Figure 2.4: Illustration of a $1\mathbb{D}$ AFM chain. Dots represent atom sites, while the arrows represent the spin of each atom, a is the repetition distance of the "main" lattice, and a_s is the sub-lattice repetition distance.

in which C is the Curie constant of the atoms producing the AFM property, and T_N is the critical temperature below which the material is no longer AFM (called the Neél temperature, sometimes the symbol T_C is used instead). Since the magnetic moments of neighbouring atoms are equal but opposite, the total magnetic moment will be zero, except if there are uncompensated spins at surfaces or defects are present.

2.2.2 Perovskite and $LaFeO_3$ crystallography

Perovskites, or perovskite-like materials, are characterized as solids with the chemical composition ABX_3, where A and B are cations (A is the larger of the two) and X is a much smaller anion. Their structure can be visualized as a cube with A cations in the corners and a B cation in its centre with the X anions on the cube faces, see Fig. 2.5. The anions thus form an octahedron around the B-cation. Most perovskites or perovskite-like materials deviates from this cubic arrangement[7], but a pseudo-cubic unit cell may be defined instead for such structures (pseudo cubic parameters and Miller indices will be denoted with subscript pc through this thesis). The Goldschmidt tolerance factor t is a

[7] Even natural perovskite $CaTiO_3$ which was discovered by Lev Perovski in 1839 has orthorhombic structure [31, 32]

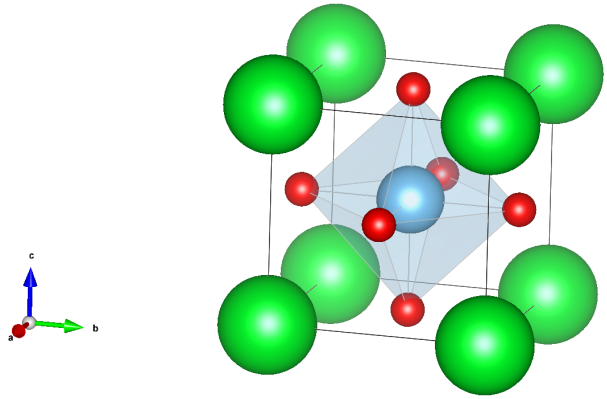

Figure 2.5: Illustration of the STO unit cell. The "green" Sr ions are situated in the corners of a cube, with the "grey" Ti ion sitting in its middle. On the cube faces "red" oxygen ions are found, forming an octahedron around the Ti ion. Simulated in VESTA [36].

measure of the perovskite-likeness of a structure, defined as

$$t = \frac{r_A + r_X}{\sqrt{2}\,(r_B + r_X)}, \tag{2.5}$$

where r is the ionic radii for the ion indicated by the subscript. For an ideal perovskite $t = 1$, and the larger $1 - t$ of a structure the less perovskite-like the structure is [1]. Perovskites may deviate from the ideal structure by tilting the oxygen octahedra or displacing the cations, thus increasing the pseudo cubic unit cell's deviation from a cube. Glazer developed a notation for describing the tilt of perovskite oxygen octahedra [33]. In the Glazer notation, a general tilt of octahedra along the pseudo cubic unit cell axes are denoted $a^{\pm}b^{\pm}c^{\pm}$. A plus sign in the superscript means that octahedra are tilted in phase along this axis, while a minus sign indicates out of phase tilts. When heated the unit cell will expand, allowing the octahedra more space and reducing tilting. Therefore a perovskite-like structure is expected to approach an ideal perovskite as its temperature is increased [34, 35].

LFO is a perovskite-like solid that crystallizes in the orthorhombic space group $Pbnm$[8] with bulk lattice parameters $a = 5.556$ Å, $b = 5.565$ Å, and $c = 7.862$ Å at room temperature [37]. The atomic fractional positions presented in Table 2.2 forms the LFO basis [38]. Figure 2.6a shows the resulting unit cell of LFO, which may be divided into a pseudo-cubic cell with parameters $a_{pc} = c_{pc} = 3.932$ Å and $b_{pc} = 3.931$ Å [37].

[8]Different conventions are used, $Pnma$ is the setting used by the International Tables for Crystallography [27], where it is listed as space group no. 62 (setting 1). $Pmnb$ is the second setting (labelled 2), where $\vec{a}^{(1)} \to \vec{b}^{(2)}$, $\vec{b}^{(1)} \to \vec{a}^{(2)}$. $Pbnm$ is the third setting (labelled 3), and is achieved by permuting the axes of $Pnma$ once to the right.

Table 2.2: Fractional coordinates of atoms in $LaFeO_3$ from [38] in the Pbnm setting

Atom	**Site**	**x**	**y**	**z**
La	4c	~ 0.995	~ 0.03	$1/4$
Fe	4b	0	$1/2$	0
O(1)	4c	~ 0.07	~ 0.49	$1/4$
O(2)	8d	~ 0.73	~ 0.28	~ 0.05

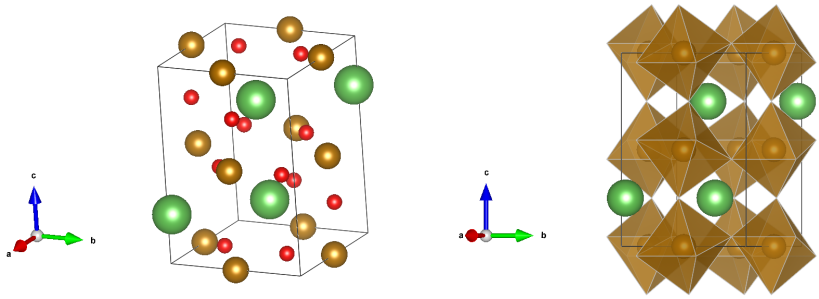

(a) **(b)**

Figure 2.6: The LFO unit cell in the Pbnm setting simulated in VESTA [36]. Green, brown, and red balls mark positions of La, Fe, and O ions respectively. In a) the full unit cell is shown. The unit cell in b) show the oxygen octahedra, rather than the oxygen ions themselves, to promote the principle of octahedra tilts.

In LFO $t = 0.0001$, calculated by numbers from [37], which indicates a nearly cubic structure. However, the phase diagram of LFO indicates that LFO is quite far from the cubic structure. LFO is reported to have no first order phase transition until $T = 1228$ K where its space group becomes $R\bar{3}c$, the first order transition to the ideal perovskite structure is expected at $T = 2140$ K [38], which is very close to its melting temperature of 2163 K [39]. The high temperature required for bulk LFO to become cubic leads one to expect that LFO is not as close to the ideal perovskite structure as the pseudo-cubic lattice parameters or the Goldschmidt tolerance factor indicates [37]. This is most likely due to the fact that the unit cell deviates from the ideal perovskite by tilting or distorting the oxygen octahedra [40] as illustrated in Fig. 2.6b. In bulk LFO the tilt system is $a^+_{pc}b^-_{pc}b^-_{pc}$ for space group $Pmnb$ [40], which transforms to $a^-_{pc}a^-_{pc}c^+_{pc}$ for Pbnm. This means that the octahedra are rotated in phase along $\vec{c}_{pc}$, and out of phase about the other two pseudo cubic axes. This causes a buckling of the Fe-O-Fe bonds so that the bond angle becomes $\sim 158^\circ$ [41].

2.2.3 $LaFeO_3$ functional properties

In LFO the $2p$ orbitals of O^{2-} are all fully occupied, as are the $5p$ orbitals of La^{3+}. The trivalent iron ions however, have its 5 $3d$ orbitals occupied by one electron each. This means that Fe^{3+} ions in LFO have a net spin. Furthermore, the originally five-fold degeneracy of the $3d$ orbitals will be lifted because of the nearly cubic symmetry experienced by Fe cations due to the oxygen anions [42], as indicated in Fig. 2.7 taken from [43]. This figure illustrates the splitting of the $3d$ orbital into the energy levels t_{2g} and e_g. The resulting t_{2g} threefold degenerate levels have a lower energy than the twofold degenerate e_g orbitals [43]. Of these two e_g orbitals one will not overlap at all with the p_z orbitals of the anions and one e_g may [44]. The ultimate effect of this orbital ordering is that bulk LFO is (G-type) AFM, with its AFM axis along the a-axis [8, 45]. Its Neél temperature is $T_N = 740$ K, highest among the group of perovskites known as the orthoferrites [46]. Above this temperature bulk LFO looses its AFM property, and a reduction of the Fe-O-Fe bond angle is thought to reduce this temperature [41]. This means that the Neél temperature of strained LFO might be reduced. The symmetry of the spin sub-lattice is low, so that LFO exhibits weak ferromagnetism as well [47]. Nanoparticles of LFO synthesized by sol-gel are reported to exhibit weak ferromagnetism [48], which is credited to uncompensated moments at the surfaces. Thin films of LFO have shown a change in the AFM axis[49], and weak ferromagnetic hysteresis loops [50] as well. This illustrates that the functional properties of LFO vary greatly with respect to the materials morphology.

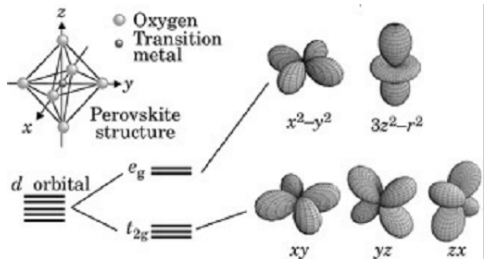

Figure 2.7: Illustration of the degeneracy of the $3d$ orbitals into t_{2g} and e_g. The transition metal ion experiences a cubic potential due to the oxygen ions, and thus the e_g orbitals will require more energy than the t_{2g} orbitals in order to be occupied. From [43].

2.2.4 Thin film synthesis and structure

Epitaxial thin film synthesis is based on depositing atoms onto the surface of a substrate, a process usually referred to as ”growth”. The word ”epitaxy” originates from Greek, *epi* meaning ”above” and *taxis* meaning ”an ordered manner”. When using the word in thin film synthesis it is understood that the atomic order of the film follows that of the substrate. Epitaxial structures may be achieved through techniques such as PLD, which will be explained in short in chapter 3. In order for epitaxial growth to happen, the bulk lattice parameters and symmetry of the material one wish to deposit should not deviate too far from that of the substrate. If the in-plane bulk lattice parameter(s) of the film differs from that of the substrate, there are two ”main” options for the film. It can either adapt to the in-plane lattice parameter(s) of the substrate or it may relax and create misfit dislocations at the interface in order to retain its original lattice parameter(s), both cases are illustrated in Fig. 2.8. Films will typically relax above a certain thickness, as the strain energy then becomes comparable to that of introducing misfit dislocations. In some cases the strain in the interface between substrate and film can be used to tailor interesting properties [51, 52].

Many of the properties one want to tailor are highly anisotropic, such as ferromagnetism

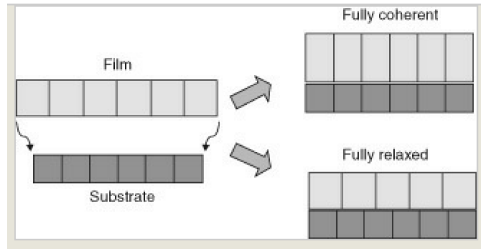

Figure 2.8: Illustration of the two main options for a film when being deposited on a substrate. The film may match its in-plane lattice parameter(s) with that of the substrate, but change its out-of-plane lattice parameter(s), or it may relax. If the film relaxes, it does so by keeping its bulk lattice parameters and introduce misfit dislocations at the interface. From [43].

and AFM. Because the orientation of the substrate dictates that of the epitaxial film, the orientation of the substrate is of great importance. Furthermore the termination of the substrate with respect to both morphology and chemistry should be as perfect as possible. How much the average surface normal deviates from the crystal normal is expressed as the substrate miscut. Every real substrate surface will have some degree of miscut, resulting in terrace steps. These steps may be used to stimulate nucleation during growth, and the orientation of the steps is yet another parameter that can be used to tailor the properties of the film. For a film exhibiting structural domains the miscut orientation can be used to increase the volume fractions of one domain at the cost of the other, even offering the possibility of engineering mono domain films [43]. The chemical termination, i.e. what kind of atoms are present at the surface of the substrate is also important as shown in the $LaAlO_3$ (LAO)/STO material system. In this system the termination of the STO substrate changes the interface between substrate and film from being insulating to conductive [5].

STO is an insulating and nonmagnetic cubic[9] perovskite of space group $Pm\bar{3}m$ (no. 221) above 105 K. It remains cubic up to temperatures of $973 - 1173$ K [43], and its lattice parameter is $a = 3.905$ Å [1] at room temperature. STO is often used as a substrate for thin films of other perovskites as its lattice matches that of a wide range of other perovskites and it remains cubic at typical deposition temperatures. By doping STO with e.g. $0.1-0.5$ wt% Nb or La, it becomes conductive, which opens up for a wide range of applications for films grown on STO. Different epitaxial thin films of perovskites grown on STO exhibit a wide range of functional properties from high temperature superconductivity, metallic, AFM, ferromagnetic and multiferroic properties [43].

As the pseudo cubic unit cell parameters of bulk LFO are slightly larger than that of STO, epitaxial LFO films on STO will be strained. The mismatch is only 0.1% for the pseudo cubic unit cell, but if one instead compares the orthorhombic unit cell of LFO to STOs, one sees that $a_{LFO} \approx b_{LFO} \approx \sqrt{2}\, a_{STO}$, and $c_{LFO} \approx 2c_{STO}$, with mismatches of 0.6%, 0.8% and 0.6%, respectively. This means that LFOs orthorhombic unit cell will fit itself by orienting its two shorter axes 45° to two of the STO axes, and its longer axis parallel to the remaining STO axis, such as the case presented in Fig. 2.9. Thus, there are at least 24 ways[10] that the larger LFO unit cell can fit on the smaller STO lattice, of which only three are distinguishable in the TEM:

A: $[100]_{LFO} \parallel [011]_{STO}$, $[010]_{LFO} \parallel [0\bar{1}1]_{STO}$, and $[001]_{LFO} \parallel [100]_{STO}$

B: $[100]_{LFO} \parallel [101]_{STO}$, $[010]_{LFO} \parallel [10\bar{1}]_{STO}$, and $[001]_{LFO} \parallel [010]_{STO}$

C: $[100]_{LFO} \parallel [110]_{STO}$, $[010]_{LFO} \parallel [\bar{1}10]_{STO}$, and $[001]_{LFO} \parallel [001]_{STO}$

These three distinguishable orientations are labelled A, B, and C after which STO axis the orthorhombic $\vec{c}$ axis aligns with. Note that all of these orientations will have the $\vec{b}$

[9] STO has been shown to exhibit piezoelectricity to some small degree, indicating that it has no centre of symmetry and is thus not perfectly cubic [53]

[10] For instance, if $\vec{c}_{LFO}$ points in the same direction as $\vec{c}_{STO}$, $\vec{a}_{LFO}$ may point along $\vec{a}_{STO} + \vec{b}_{STO}$, $\vec{b}_{STO} - \vec{a}_{STO}$ or opposite to these directions giving a total of four possibilities in this case. Similarly if $\vec{c}_{LFO}$ points along $-\vec{c}_{STO}$, thus for the case where the c vectors are parallel or anti-parallel, there are eight possibilities.

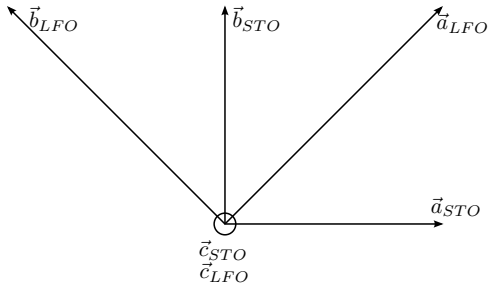

Figure 2.9: Illustration of one way the larger $Pbnm$ unit cell of LFO can fit onto the smaller $Pm\bar{3}m$ unit cell of STO. In this particular case, the a and b axes of LFO and STO share the same plane, with their c axes being parallel and pointing out of the paper plane, forming a right-hand system. The connection between the c axes are $\|\vec{c}_{LFO}\| \approx 2\|\vec{c}_{STO}\|$.

axis in the $(111)_{STO}$ plane. Monsen observed structural domains in LFO grown on (001) STO in his master thesis [7], which were attributed to the three orientations mentioned above[11]. Similar results are reported by Scholl *et al.* [54]. The shape and sizes of the structural domains imaged by TEM matches fairly well the shape and sizes of the AFM domains imaged by X-ray Magnetic Linear Dichroism Photoelectron Emission Microscopy (XMLD-PEEM) [54]. According to Wang *et al.* [35, 55] the twin laws of the natural perovskite $CaTiO_3$, which has $Pbnm$ structure, are reflection about the $\{110\}$ and $\{112\}$ planes ($Pbnm$ indices), as well as $90°$ rotation about $[001]$. $1/2[001]$ APBs are also possible. Indeed, Monsen observe both $(001)_{pc}$ and $(101)_{pc}$ twins in his thin films.

In thin (001) LFO/STO films the octahedra in the first layer of LFO share only one apex with the substrate, thus giving the film a certain possibility to adapts by distorting its octahedra, and such films have shown a drop in Neél temperature [56]. When growing films on (111) oriented STO however the first LFO unit cells will each share three oxygen atoms (one octahedra face) with the substrate, thus possibly locking the LFO structure tighter to the substrate's. This has the effect of increasing the strain in the film, and possibly altering out-of-plane Fe-O-Fe bonds, thus possibly decreasing the Neél temperature of such films even further.

To examine the connection between LFO domains and STO, one can define the unit cell axes of STO to be along the Cartesian unit vectors $\hat{\imath}$, $\hat{\jmath}$, and $\hat{k}$. The unit cell of STO can then be expressed as $\vec{a}_{STO} = a\hat{\imath}$, $\vec{b}_{STO} = a\hat{\jmath}$, and $\vec{c}_{STO} = a\hat{k}$. STOs reciprocal space is thus spanned by the vectors $\vec{a}^*_{STO} = 2\xi\hat{\imath}$, $\vec{b}^*_{STO} = 2\xi\hat{\jmath}$, and $\vec{c}^*_{STO} = 2\xi\hat{k}$, with $\xi = \pi/a_{STO}$. Assuming that two LFO axes lie in the same plane as two of the STO axes and are inclined

[11] Monsen used a slightly different convention for the notation of some of these domains.

by 45° to these, the three LFO domains can be expressed as (approximately):

$$\begin{aligned}
\vec{a}_A &= \vec{b}_{STO} + \vec{c}_{STO} & \vec{b}_A &= -\vec{b}_{STO} + \vec{c}_{STO} & \vec{c}_A &= 2\vec{a}_{STO} \\
\vec{a}_B &= \vec{a}_{STO} + \vec{c}_{STO} & \vec{b}_B &= \vec{a}_{STO} - \vec{c}_{STO} & \vec{c}_B &= 2\vec{b}_{STO} \\
\vec{a}_C &= \vec{a}_{STO} + \vec{b}_{STO} & \vec{b}_C &= -\vec{a}_{STO} + \vec{b}_{STO} & \vec{c}_C &= 2\vec{c}_{STO}.
\end{aligned}$$

Here it is assumed that the orthorhombic cell distorts by changing the lengths of its axes to fit the STO lattice as in Fig. 2.9. The advantage of doing this assumption is that the reciprocal lattices of the three domains are easily obtainable:

$$\begin{aligned}
\vec{a}^*_A &= \xi\left(\hat{i}+\hat{k}\right) & \vec{b}^*_A &= \xi\left(\hat{i}+\hat{k}\right) & \vec{c}^*_A &= \xi\hat{i} \\
\vec{a}^*_B &= \xi\left(\hat{j}+\hat{k}\right) & \vec{b}^*_B &= \xi\left(\hat{i}-\hat{k}\right) & \vec{c}^*_B &= \xi\hat{j} \\
\vec{a}^*_C &= \xi\left(\hat{i}+\hat{j}\right) & \vec{b}^*_C &= \xi\left(-\hat{i}+\hat{j}\right) & \vec{c}^*_C &= \xi\hat{k},
\end{aligned}$$

With these definitions, a connection between the reciprocal space of STO and LFOs three domains can be made, yielding the following reciprocal lattice vectors

$$\vec{G}^{STO}_{111} \approx \vec{G}^{A}_{202} \approx \vec{G}^{B}_{202} \approx \vec{G}^{C}_{202} \tag{2.6}$$
$$\vec{G}^{STO}_{11\bar{2}} \approx \vec{G}^{A}_{\bar{1}32} \approx \vec{G}^{B}_{\bar{1}32} \approx \vec{G}^{C}_{20\bar{4}} \tag{2.7}$$
$$\vec{G}^{STO}_{\bar{1}01} \approx \vec{G}^{A}_{11\bar{2}} \approx \vec{G}^{B}_{0\bar{2}0} \approx \vec{G}^{C}_{\bar{1}12} \tag{2.8}$$
$$\vec{G}^{STO}_{0\bar{1}1} \approx \vec{G}^{A}_{020} \approx \vec{G}^{B}_{1\bar{1}\bar{2}} \approx \vec{G}^{C}_{1\bar{1}2} \tag{2.9}$$
$$\vec{G}^{STO}_{1\bar{1}0} \approx \vec{G}^{A}_{\bar{1}12} \approx \vec{G}^{B}_{11\bar{2}} \approx \vec{G}^{C}_{0\bar{2}0} \tag{2.10}$$
$$\vec{G}^{STO}_{001} \approx \vec{G}^{A}_{110} \approx \vec{G}^{B}_{1\bar{1}0} \approx \vec{G}^{C}_{002} \tag{2.11}$$
$$\vec{G}^{STO}_{110} \approx \vec{G}^{A}_{1\bar{1}2} \approx \vec{G}^{B}_{112} \approx \vec{G}^{C}_{200}. \tag{2.12}$$

The $\approx$ symbol in this situation refers to similarity with respect to both lengths and directions. Equations 2.6-2.12 can be used to index different diffraction patterns, and are as such useful tools[12]. Throughout this thesis the relations presented above is assumed when indexing diffraction patterns. It should be noted that as a_{LFO} and b_{LFO} are very similar these two axes may in principle be interchanged. This means that e.g. the $(010) \rightarrow (100)$. For simplicity the $\vec{b}_{LFO}$ axis is assumed to lie in the STO (111) plane, as illustrated in Fig 2.10. However, since a_{LFO} is more similar to the $< 1\bar{1}0 >_{STO}$ direction than b_{LFO}, the $\vec{a}$ axis is probably the one that will be in-plane. An important fact about these reciprocal lattices is that they overlap (or do so very closely) with STO reflections, except for some possible reflections specific to LFO domains (called super reflections). For instance, when viewing along the $[111]$ zone axis of STO the three domains will each be able to produce three separate super reflections in addition to produce the common STO $\{1\bar{1}0\}_{STO}$ reflections, while for the other two zone axes discussed here, some super reflections are unique only to the C domain.

[12] Equations 2.11 and 2.12 are redundant as they can be made from the other relations quite easily, but they are explicitly given as this simplifies the indexing of the $[1\bar{1}0]_{STO}$ zone axis.

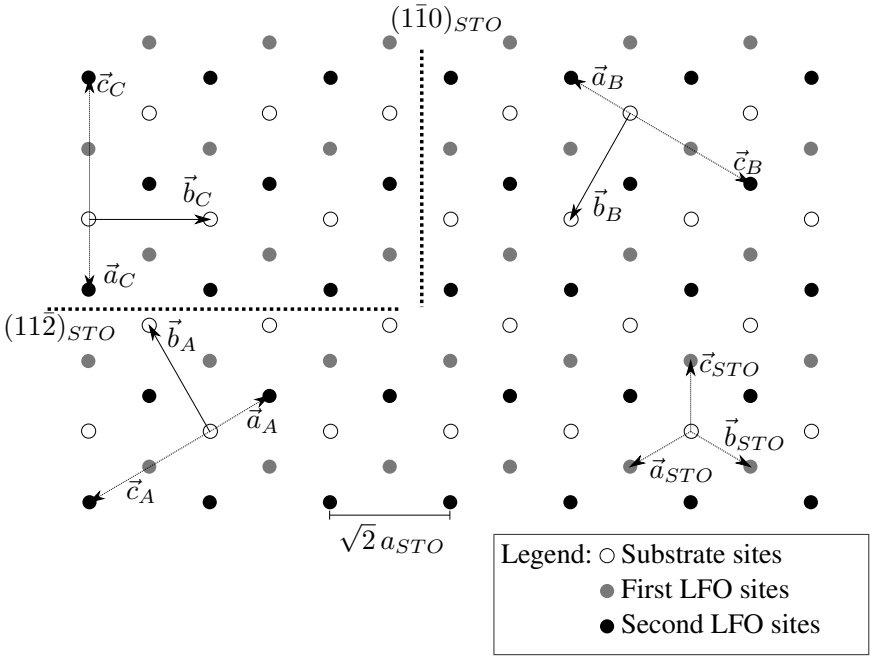

Figure 2.10: Illustration of the different LFO domain orientations on (111) oriented STO by assuming $a_{LFO} = b_{LFO} = \sqrt{2}\,a_{STO}$ and $c_{LFO} = 2a_{STO}$. Circles mark atom sites of the STO surface, the lighter dots mark the first layer of atom in LFO, while the dense dark dots mark the second layer of LFO atoms. Dotted vectors refer to vectors with an angle to the paper plane, while full vectors are in-plane. The dotted lines mark possible grain boundaries. In the lower right the unit cell of STO is presented. Note that the twin boundaries of the $Pbnm$ structure will not be observable in PV geometries, as these will be angled to the $(111)_{STO} \equiv (101)_{LFO}$ plane.

The reason why this discussion has been limited to these three zone axes only, is that these zone axes are either normal to, or perpendicular to the film surface. Figure 2.11 show simulations from CrystalKit [57] of the three zone axes of STO discussed above. For each zone the expected reflections due to LFO domains are drawn in and indexed manually (i.e. they are not simulated) according to Equations 2.6-2.12. Blue, green, and red colours are used for A, B, and C domains respectively, and this convention is used throughout this thesis. The open circles show where LFO reflections are expected to appear, and reflections common for all LFO domains have been marked with yellow open circles. In Figs. 2.11b and 2.11a only one domain can be separated from the others, while in Fig. 2.11c all three domains are distinguishable at the same time.

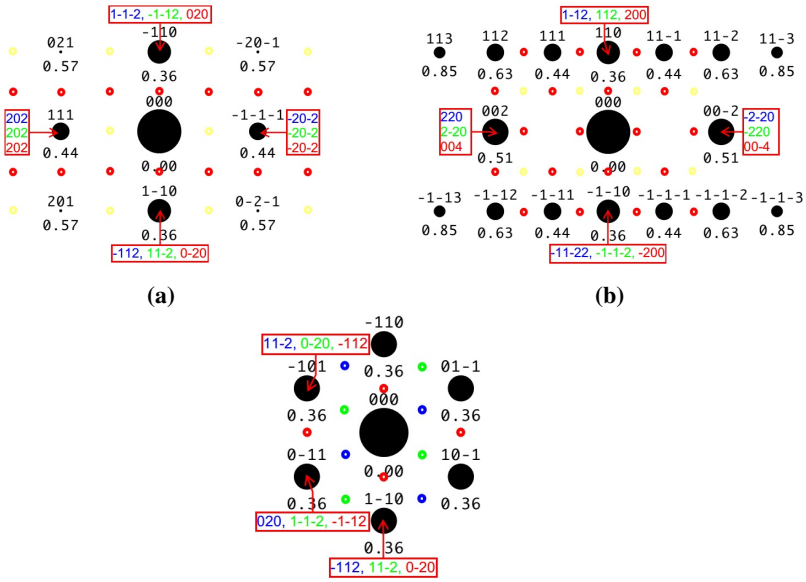

Figure 2.11: Simulated DPs of the STO zones $[11\bar{2}]$ (a), $[1\bar{1}0]$ (b), and $[111]$ (c) through the use of CrystalKit [57]. Black disks and numbers refer to STO indices, with the miller indices above the dots, and the value of $\left\| \frac{\vec{G}_{hkl}}{2\pi} \right\|$ below. Indices in blue, green, and red refer to A, B, and C domains respectively, and has been manually translated from STO indices by the use of Equations 2.6-2.12. The open circles mark where reflections due to the three LFO domains are expected to occur, blue, green, and red referring to A, B, and C respectively, while yellow is used for common LFO indices.

2.3 Transmission Electron Microscopy

This section is heavily based on the detailed book by Williams and Carter [26], and as such citations to this book is omitted through this section.

A Transmission Electron Microscope is a powerful tool in understanding both structure and composition of materials, therefore it plays a vital role within the fields of materials science, nanotechnology, and biotechnology. In essence a TEM exploits the particle-wave duality of electrons. A comparison to visible light microscopes (VLMs) is useful for explaining the principle behind TEM. VLMs manipulate photons, and the TEM uses electrons in much the same ways, although there are fundamental as well as practical differences between the two instruments. One of the main motivations for using a TEM rather than a VLM is that a TEM offer much higher resolution. The general idea of resolution, or resolving power, is that two features or objects in an image cannot be distinguished if the distance between the two is so that the diffraction maxima of one object lies between the first diffraction minima and the maxima of the other object. This is in essence limited by two factors, the wavelength of the waves (or particles) used, and the numerical aperture of the instrument. The smallest distance between two objects δ that an optical system with numerical aperture of $\mu \sin \beta$ is able to resolve is given by

$$\delta = \frac{0.61\lambda}{\mu \sin \beta}. \tag{2.13}$$

Equation 2.13 is called the Rayleigh criterion for the resolving power of an imaging system, in which λ is the wavelength of the waves used, μ is the refractive index of the viewing medium and β is the semi-angle in which the magnifying lens collects photons. Often $\mu \sin \beta \approx 1$, so that the resolving power of an optical microscope is limited to the wavelength of the waves.

Louis de Broglie showed that the wavelength of electrons λ (in nm) is dependent on their energy E (in eV) as in Equation 2.14

$$\lambda = \frac{1.22}{\sqrt{E}}. \tag{2.14}$$

The electrons in a TEM operating at 200 keV will move with relativistic velocity and have a wavelength of 0.00251 nm. This means that a TEM should be able to resolve objects well below the Ångstrom scale, if one applies the Rayleigh criterion. However there are several limitations to TEM that lowers the resolution, imperfections in the optics being the main culprit. In this section the design, techniques and limitations to TEM are presented.

2.3.1 Scattering and electron interactions

Electrons and photons interact very differently with matter, as one is a charged fermion with a finite mass and another is a neutral and massless boson. From a classical point of view, light (electromagnetic waves) scatters on a single electron by causing it to vibrate and thus emit electromagnetic radiation itself. Because an electromagnetic wave of high

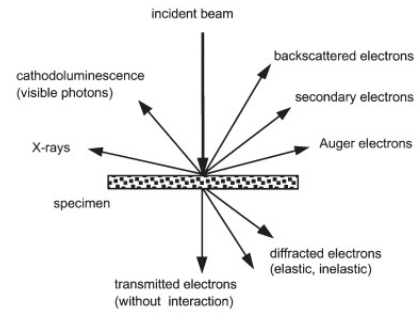

Figure 2.12: The most important interactions between the electron beam and a specimen in a TEM. From [58].

energy doesn't interact strongly with the core of an atom this, is fairly simple to extend to atoms and thus molecules and crystals [23]. For a beam of electrons however, things are more complicated because the electrons in the beam interact quite strongly with both the electrons and the core of an atom. Interaction between the electron beam and the electron cloud of an atom will cause the incoming beam to scatter slightly. The positive attraction by the nucleus however can change the path of the incoming electrons by up to $180°$. Several other interactions also occur in a TEM such as core shell excitations and de-excitations of atoms, producing characteristic X-rays. Figure. 2.12 summarizes most of the important interactions between the electron beam and a specimen. Due to the strong interaction between electrons and matter, the samples studied in a TEM need to be very thin, typically less than a hundred nanometres.

The Rutherford differential cross section describing the probability of an electron scattering elastically through an angle θ into a solid angle $d\Omega$ by a nucleus of an atom with atomic number Z as illustrated in Fig. 2.13, is given by

$$\sigma_R(\theta) = \frac{Z^2\lambda_R^4}{64\pi^4 a_0^4} \frac{d\Omega}{\left(\sin^2\left(\frac{\theta}{2}\right) + \frac{\theta_0^2}{4}\right)^2}. \tag{2.15}$$

In Equation 2.15 λ_R is the relativistic wavelength of the electron, Z is the atomic number of the scatterer, $a_0 \approx 0.0529$ nm is the Bohr radius, and $\theta_0 = 0.117Z^{1/3}/E_0^{1/2}$ (E_0 is the electron energy in keV). The equation is only valid for large scattering angles, moderate electron energies (less than 300-400 kV accelerating voltages in a TEM) and for light elements ($Z < 30$). Rutherford scattering is incoherent while electrons scattered to lower angles ($< 3°$) by diffraction phenomena are coherent. These two scattering mechanisms are the main ways contrast is achieved in the TEM.

For elastic scattering cases when Equation 2.15 is not valid, i.e. for diffracted electrons, one need to consider the intensity of a scattered electron wave as the absolute square of the atomic form factor. The atomic form factor is defined as the FT of the scattering object.

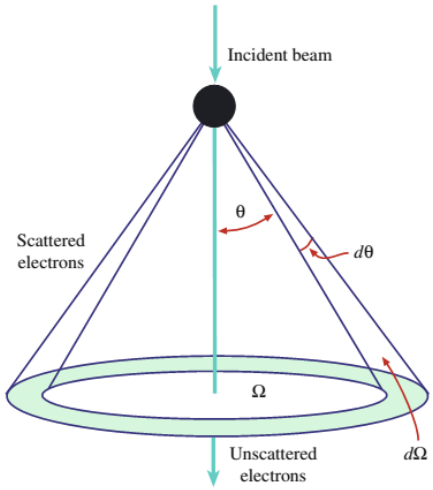

Figure 2.13: Schematic of elastic Rutherford scattering of an incident beam on a scattering centre. The scattered beam scatters through an angle θ into the solid angle $d\Omega$. From [26].

For x-rays scattering on an atom the general expression is

$$f_x\left(\vec{Q}\right) = \int_{-\infty}^{\infty} \rho\left(\vec{r}\right) e^{i\vec{Q}\cdot\vec{r}} d\vec{r}, \tag{2.16}$$

where $\vec{Q} = \vec{q}' - \vec{q}$ is the wave vector transfer of the incoming wave with wave vector $\vec{q}$ and the scattered wave with wave vector $\vec{q}'$. $\rho\left(\vec{r}\right)$ is the electron density of the atom as a function of position $\vec{r}$ from the nucleus. The atomic form factor of electrons can be related to that of x-rays f_x by

$$f^B\left(\vec{Q}\right) = \frac{me^2}{2\pi\hbar\epsilon_0}\left(\frac{Z - f_x(\vec{Q})}{\left\|\vec{Q}\right\|^2}\right), \tag{2.17}$$

called the Mott-Bethe formula. In this equation m is the electron mass, e the electron charge, ϵ_0 the permittivity of vacuum, and $\hbar$ is the reduced Planck constant. Equation 2.17 is useful for understanding and predicting how electrons scatter on isolated atoms. When studying samples in a TEM the electrons will not scatter on a single atom however, but a collection of atoms. Because the wavelength of the electrons is much smaller than the inter atomic distances in most crystals, diffraction will occur. This type of collective scattering is coherent and the intensity in such a scattered beam is given by the structure factor. In the same way the atomic form factor is the FT of the scattering potential the structure factor is the FT of the structure of the collection of scatterers. To evaluate the FT of a crystal it is first advantageous to look at the principle of diffraction and how it occurs in a crystal.

Diffraction - Bragg's law and the Laue condition

The phenomena when waves scatter on gratings is called diffraction, and analysis of so-called diffraction patterns (DPs) is an important part when determining the structure of a material. Because of the short wavelength of the electrons in the TEM the crystal will serve as a diffraction grating. The Braggs visualized the lattice planes in a crystal as "mirrors" able to reflect incoming waves according to Snell's law, as illustrated in Fig. 2.14a. Throughout this thesis, the wave vector of an incoming plane wave of electrons will be denoted as $\vec{k}$, while scattered waves will have wave vector $\vec{k}'$, their magnitudes denoted as k and k' respectively. Constructive interference will only occur if the difference in path length between the incoming plane wave and the scattered wave equals an even number of wavelengths λ, yielding Bragg's law

$$2d \sin \theta_1 = n\lambda. \tag{2.18}$$

In Bragg's law θ is the angle the incoming wave vector $\vec{k}$ makes to the lattice planes, and n is an integer. For the case of $\lambda = 0.00251$ nm and $d = 1.73$ Å (the d_{111} of Pt [59, 60]) $\theta = 0.04°$, illustrating the fact that this kind of scattering is mainly in the forward direction. When Bragg's law is satisfied, the plane is said to be "in Bragg". The relation given by the Braggs is very useful, but because the diffracted electrons in a TEM is not reflected, it is physically wrong. The Laue equations give a better understanding of the actual physics behind diffraction. An incoming plane wave scattering on two objects separated by some $\vec{R}$ generates a scattered wave as shown in Fig. 2.14b. This scattered wave will interfere constructively if the difference in path length equals an integer times the wavelength, according to

$$\vec{R} \cdot \left(\vec{k}' - \vec{k}\right) = 2\pi n. \tag{2.19}$$

As this must hold for all $\vec{R}$ in the crystal, the wave vector transfer $\vec{K} \equiv \Delta\vec{k} = \vec{k}' - \vec{k}$ must equal a reciprocal lattice vector, i.e. $\vec{K} = \vec{G}$. This is called the Laue condition for interference. Both Bragg's law and the Laue conditions state the allowed directions of diffracted waves.

Because of the Laue conditions it is simple to find the structure factor for a crystal. A crystal with N unit cells will have a structure factor of $NF_{uc}\left(\vec{k}\right)$, where $F_{uc}\left(\vec{k}\right)$ is the structure factor of the unit cell. As this is defined to be the FT of the unit cell, the intensity of diffracted beams are governed by the periodicity of the unit cell only. A wide range of wave vector transfers are allowed for non-crystalline materials, but due to the Laue conditions only those equal to a reciprocal lattice vector are allowed for a crystal. For a crystal with a unit cell with n potentially different atoms with fractional positions $\vec{r}_j = x_j\vec{a} + y_j\vec{b} + z_j\vec{c}$ the intensity of the scattered beam due to the plane (hkl) becomes

$$F_{hkl} = \sum_{j=0}^{n} f_j\left(\vec{G}_{hkl}\right) e^{i\vec{G}_{hkl}\cdot\vec{r}_j} = \sum_{j=0}^{n} f_j\left(\vec{G}_{hkl}\right) e^{2\pi i(hx_j + ky_j + lz_j)}. \tag{2.20}$$

Depending on the unit cell, the structure factor may be zero for certain $\vec{G}$ and the scattered beam suffers destructive interference (the diffracted beam is extinct). It is clear from

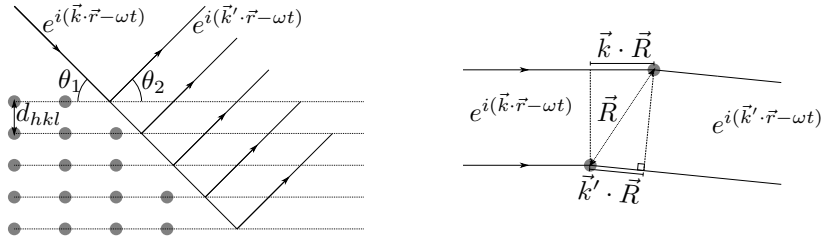

(a) Bragg approach **(b)** Laue approach

Figure 2.14: Sketch of the two different approaches to interference of scattered waves on planes (Bragg) or scattering centres (Laue). In both figures the incoming plane wave has wave vector $\vec{k}$, and the elastically scattered wave has wave vector $\vec{k}'$. $\vec{r}$ is the position of the wave at time t, having frequency ω, as usual. a) Schematic of the Bragg's law. The incoming plane wave makes an angle θ_1 to the lattice planes (hkl) and reflects according to Snell's law with an angle $\theta_2 = \theta_1$. The reflected wave has wave vector $\vec{k}'$. The lattice planes are separated by a distance d_{hkl} and are drawn as dotted lines. For clarity only some of the lattice points are drawn. b) The Laue approach, where the incoming wave scatters on two objects spatially separated by $\vec{R}$. By simple geometry the path difference is $\vec{k}' \cdot \vec{R} - \vec{k} \cdot \vec{R}$.

Braggs law that if $\theta = 0$ no diffraction will occur. However most of TEM DP images are acquired under such conditions. In order to explain how diffraction occurs in the TEM the Ewald sphere is helpful.

The Ewald sphere

As mentioned previously the spacing between lattice planes d_{hkl} is related to reciprocal lattice vector $\vec{G}_{hkl}$. However, as $\vec{G}_{hkl}$ of a real crystal does not point to points, but CTRs, $\vec{G}_{hkl}$ is not well defined. This causes the Laue conditions to relax slightly, meaning that lattice planes will diffract even when not exactly in Bragg. When $\vec{k}$ is along a zone axis the planes forming the zone will make an angle $\theta = 0$ to $\vec{k}$. As mentioned earlier such planes cannot be in bragg. A sketch of the Ewald sphere is presented in Fig. 2.15. This is a sphere existing in reciprocal space, and having radius $\vec{k}$. It's surface passes through the (000) reciprocal lattice point, and its origin relative to (000) is given by $\vec{k}$ relative to the physical crystal. It can be seen that $\vec{K}$ originates at (000) and terminates on the Ewald sphere surface for any $\vec{k}'$ as long as $\left\|\vec{k}\right\| = \left\|\vec{k}'\right\|$ (elastic scattering).

The Laue conditions state that $\vec{K}$ must equal $\vec{G}_{hkl}$ in order for the plane (hkl) to diffract. This is equivalent to saying that the Ewald sphere must pass through the centre of the (hkl) CTR in order for the plane to diffract. If the Ewald sphere instead intersects the CTR a little off its centre the lattice plane will still diffract, although with reduced intensity. The excitation error $\vec{s}$ is a measure of how far a CTR is from satisfying the Laue condition exactly. It is defined by $\vec{K} = \vec{G} + \vec{s}$ as shown in Fig. 2.15. If the excitation error terminates

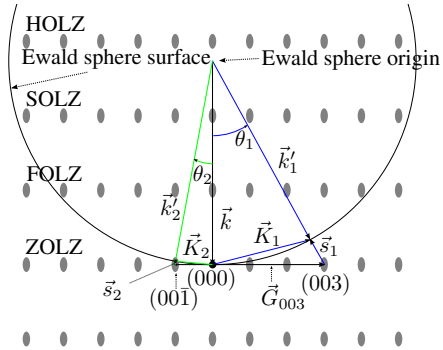

Figure 2.15: $2\mathbb{D}$ Illustration of the Ewald sphere in the reciprocal space of a hypothetical crystal. The principle of Laue zones is also illustrated. Reciprocal lattice points that lie in a plane with $\vec{k}$ as its normal will form a Laue zone. The incoming wave vector $\vec{k}$ terminates in the (000) lattice point, and thus decides the origin of the sphere. In this illustration the reciprocal lattice of the hypothetical crystal is smeared out in the viewing direction to illustrate CTRs due to the "thinness" of the sample. The (000) point is still point-like, and is shown as more dense than the other points to signify that the "intensity" of the other reciprocal lattice points is distributed across their corresponding CTR. The elliptical shape of the CTRs can be considered to show the boundary within which e.g. 90% of the CTR intensity is contained. Two scattering cases are shown, $\vec{k}'_1$ and $\vec{k}'_2$, where only the latter will satisfy the Laue conditions sufficiently to produce a reflection in a DP. The wave vector transfers $\vec{K}_1$ and $\vec{K}_2$ are shown for each case, as well as their excitation errors $\vec{s}_1$ and $\vec{s}_2$, and the Bragg angles θ_1 and θ_3. $\vec{s}_1$ will be too large in magnitude for the (003) reflection of this particular crystal to be excited. In fact the (015) reflection will have a better chance to appear in the FOLZ than the (003) in the ZOLZ. $\vec{s}_2$ on the other hand lie within the CTR, and thus the $(00\bar{1})$ and (001) planes will satisfy the Laue condition sufficiently and can appear in a DP.

within the CTR the corresponding plane will diffract. As $\vec{K}$ can in theory terminate on any point on the surface of the Ewald sphere $\vec{s}$ of a single reciprocal lattice point can take infinitely many values. In the figure the minimal excitation error of the (003) plane, $\vec{s}_1$, is too large for this plane to diffract. The $(00\bar{1})$ plane however have several excitation errors terminating within its CTR. A non-minimal excitation error $\vec{s}_2$ has been drawn explicitly. This plane will therefore be able to diffract electrons into slightly different angles.

Fig. 2.15 also serves to explain the principle behind Laue zones. With an incoming wave vector $\vec{k}$ defining both the origin of the Ewald sphere and the (000) reflection, one can define a set of planes with normals parallel to $\vec{k}$, so that all the reciprocal lattice points are contained within such planes. The lattice points lying in the plane which also contains the (000) spot are called the Zero-Order Laue Zone (ZOLZ), the ones in the second plane (towards the Ewald sphere centre) is called the First-Order Laue Zone (FOLZ), the ones in the third plane are called the Second-Order Laue Zone (SOLZ) and the ones in the other planes are called Higher-Order Laue Zones (HOLZs). Reflections in a DP are usually due to the intersection of the Ewald sphere with the ZOLZ, but one can sometimes observe other Laue zones as well, for instance in high angle annular dark field (HAADF) images.

If the radius of the Ewald sphere increases, i.e. a smaller wavelength of radiation is used, the Ewald sphere surface will grow and become more flat. This will then cause more reflections from e.g. the ZOLZ to appear in the DP as can be appreciated by Fig. 2.15. This is typically the case in a TEM, and when on a zone axis many reflections from the ZOLZ are generally present. In addition, the Ewald sphere discussed so far has been an infinitely thin spherical shell. In reality this shell will have a finite thickness, depending on the radiation source used.

2.3.2 Microscope design

In order to understand TEM results an understanding of the instrument itself is required. As the name suggests the instrument transmits electrons through a specimen and detects the various attributes of these electrons. The basic design of most TEMs is such as the one shown in Fig. 2.16. The instrument is constructed as a column in which a vacuum of a certain quality is maintained. An electron gun is situated at the top of the column, and is used to produce the beam of high energy electrons. The gun can be a thermionic gun consisting of a W or LaB_6 filament which is heated in order to make it easier to pull out electrons with an electric field. An alternative to the thermionic gun is a field emission gun (FEG). This type of electron source pulls electrons from a very fine needle by applying an electric field. The needle can be heated to make it easier to extract electrons, but this will reduce their coherency. A FEG can also be kept at room temperature to increase the coherency of the electrons, but such a gun must be operated under ultra high vacuum of $< 10^{-9}$ Pa, in order to reduce contamination degrading the tip. The brightness (intensity per solid angle) of a FEG is generally superior to a thermionic gun. Because the coherency of the electrons in a FEG is much better than for thermionic guns, a FEG is preferable when acquiring phase-contrast images. However, as the needle tip of a FEG is extremely small, FEGs won't be able to image as large areas as a TEM with a thermionic gun, when doing amplitude contrast imaging a thermionic gun may therefore be preferable. The concepts of phase- and amplitude contrast will be discussed in more detail later.

After electrons are extracted from the filament they are formed into a beam by a system of magnetic lenses, deflection coils, and apertures, called the illumination system. This part of the instrument determines the parallelism of the beam, measured by the convergence angle α. A parallel beam is required for applications such as diffraction, Bright Field (BF) and DF imaging. In STEM and convergent beam electron diffraction (CBED) techniques a larger convergence angle is often used, as this determines the probe quality and properties. Apertures in the TEM are used to select which electrons one wish to "pass on" to the later parts. The condenser aperture is used to select which electrons from the gun that are allowed to hit the specimen. Electrons that travel far from the optic axis are less coherent, and this aperture can be used to reduce the amount of incoherent electrons. This aperture also decides the convergence angle to a large extent. The rest of the illumination system consists of electromagnetic lenses and deflectors. The deflectors are coils that can tilt the electron beam off the optic axis. When applied as a pair these coils can shift the beam off the optic axis while still keeping the beam parallel to it. The lenses in the illumination system essentially "images" the filament.

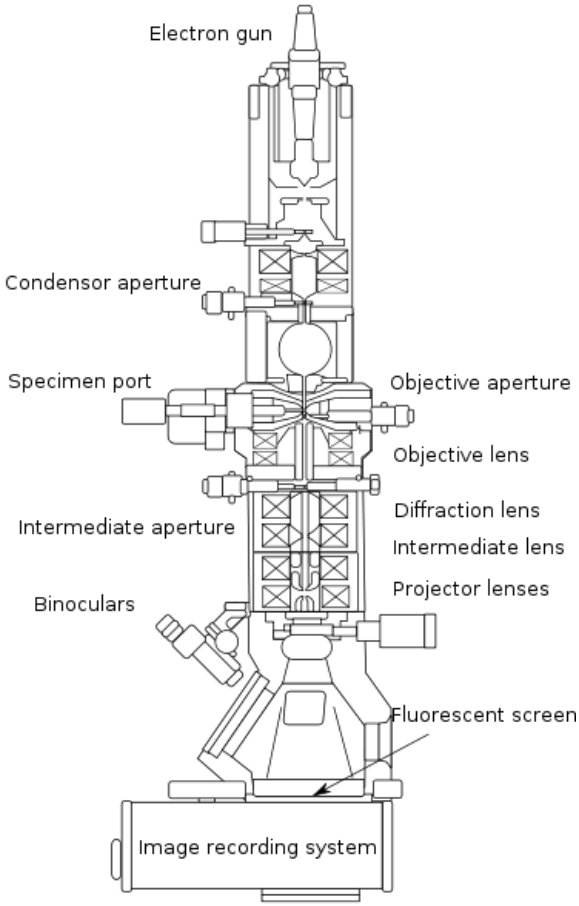

Figure 2.16: Schematic drawing of a typical TEM column. The different components of the instrument are shown, all except the condensor lens (which sists above the condensor aperture) are labelled. From [61].

Lens systems in the TEM are decisive to the instrument. They are electromagnetic pole-pieces that generate a nearly symmetric magnetic field around the optical axis. Magnetic lenses in the TEM are somewhat equivalent to refractive lenses in regular optical microscopes, and most of the terminology and the theory behind TEM are therefore based on regular light optics. A general "problem" with all lens systems is that they are finite in size, and thus they cannot collect all the information (rays) emitting from a specimen. This means that no perfect image can be acquired because a point will form a Gaussian distribution in the image. All lenses in a TEM suffer from aberrations and astigmatism, and electrons travelling through a lens far from the optic axis will be more affected by lens defects than electrons travelling closer to the optic axis. The simplest way of limiting aberrations is therefore to use small apertures, but this will reduce the intensity. Other means to correct for lens defects are available, but these solutions are quite expensive and delicate. The greatest difference between the magnetic lenses of a TEM and the refractive lenses of a VLM, is that the strength of the magnetic lenses can be changed as needed. This means that the focal length of each lens can be changed at will during operation.

The objective system is where the specimen inserted into the TEM sits and the basis for the final image is formed. The objective lens (which in practise usually consists of several lenses) is the strongest and most important lens in the TEM when operated in normal TEM mode. Because it collects and manipulates the electrons being transmitted through the specimen the final image is especially sensitive to defects in this system. The electron DP is formed in the focal plane of this lens, and inserting an aperture in the front focal plane allows the operator to form images with specific diffracted beams (dark- and bright field). An aperture can also be inserted into one of the image planes of this system to limit the image to a selected area of the specimen. This aperture is called a selected area (SA) aperture, and is frequently used when acquiring DPs.

The intermediate image of the specimen formed by the objective system is passed on to the imaging system. This consists of an intermediate lens and a projector lens, and can be used to shift/centre the DP of the specimen, to shift the real space image itself, or to magnify the intermediate image. When the TEM operates in diffraction mode the imaging system images the back focal plane of the objective system, while in normal TEM mode it images the imaging plane. The final image is then brought to a fluorescent viewing screen or to some other kind of detector.

The depth of field $D_{ob} = d_{ob}/\beta_{ob}$ and depth of view $D_{im} = d_{ob}M_T^2/\beta_{ob}$ are measures of how much an object can be moved along the optic axis without loss of focus in the image and how much the detector in the image plane can move and still record an image being in focus. β_{ob} is the maximum angle of the beams emerging from the object, d_{ob} is the resolution in the object, and M_T is the transversal magnification of the system. D_{im} is in the order of meters, meaning that detectors and cameras in the TEM can be placed basically anywhere after the imaging system. D_{ob} is usually in the order of tens or hundreds of nanometres allowing for a whole TEM specimen can be in focus at the same time. By inserting objective apertures, β_{ob} can be reduced, and these depths can be increased.

STEM

The basic principle behind Scanning Transmission Electron Microscopy (STEM) is pretty much self-explanatory. The lenses are adjusted so that the incoming beam becomes narrow, and slightly coned. This form what is then referred to as a probe whose diameter can be down to the Å regime. By scanning this probe across the surface of the specimen convergent beam electron diffraction (CBED) patterns are formed for every probe position. These patterns are extremely sensitive to symmetries in the crystal. A STEM image is the acquired by counting the number of scattered electrons into specific solid angles for every probe position, giving a measure of how much that probe position scatters. As the image in STEM is not formed by any lenses, STEM images are independent of defects in the imaging and objective system. However, the probe itself is formed by the condensor lens system, and as such the quality of this system determines the quality of the probe, which in turn determines the resolution in the final image. Therefore the resolution in STEM images is determined by the size of the probe. Having a FEG based illumination system therefore benefits the STEM quality, as does having a small condenser aperture. Furthermore, the depth of focus when in STEM is quite low, meaning that it is mostly just the surface of the specimen that will be in focus, in strong contrast to what happens in normal TEM mode. Another effect that is important to be aware of when doing STEM, is that the electron beam will get ”channeled” by the atomic columns, so that even though only the surface is in focus, the beam doesn't spread too much as it passes through the specimen. Magnification in STEM is very different from magnification in TEM, as in STEM it is the assigned area of the sample to scan, and the size of the digital image formed by the computer, that decides the magnification.

2.4 Imaging techniques

Imaging is essentially the principle of acquiring some sort of data from different regions in a sample. Contrast is then the intensity difference of the data from two adjacent areas. When doing any kind of imaging the contrast is usually the quantity one wants to maximize. The most intuitive kind of data one can image in the TEM is the intensity of electrons coming from different areas of the sample. Contrast then arises if the transmitted data of one area differs from that of another area. The TEM is an incredibly versatile imaging system as it can determine the chemical composition of a sample by energy dispersive spectroscopy (EDS), probe the electron configuration of elements by electron energy loss spectroscopy (EELS), image structural domains by dark field imaging, and acquire phase-contrast images by high resolution TEM, in principle all from the same point in space. Each of these techniques have their strong and weak points, and this section seek to present the basic theory, limitations and/or challenges connected with the techniques applied in this thesis.

When considering the contrast in a TEM image one must consider two types of contrast.

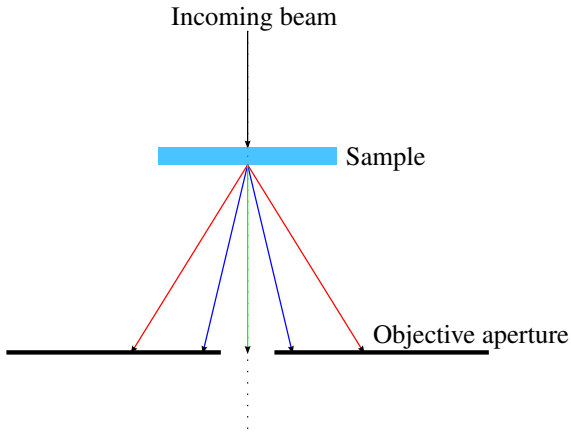

Figure 2.17: Sketch of how different scattering mechanisms can be filtered out in a TEM. The red arrows signify electrons which have experienced Rutherford scattering, blue arrows illustrate diffracted beams, and the green arrow show the unscattered beam. Insertion of an objective aperture keeps the electrons which have undergone scattering or diffraction from contributing to the final image.

When electrons travels through a specimen, both their amplitudes and phases may change. The resulting image may thus contain contrast due to both amplitude and phase changes. Diffraction and mass-thickness contrast are examples of amplitude contrast mechanisms, while HRTEM is a result of phase contrast.

2.4.1 Amplitude contrast

The promotion of amplitude contrast in the TEM usually involves inserting an objective aperture in the focal plane of the objective system. By doing this, images may be formed using only scattered or unscattered electrons. When selecting only the unscattered electrons a bright field image is achieved, and Fig.2.17 illustrates the concept. In a BF image, areas of a sample that scatter strongly will appear dark, while areas that scatters less will be brighter. Regions with high Z in a perfectly flat sample will scatter more than regions with lower Z according to the Rutherford cross section presented in Equation 2.15. Similarly if the thickness of a sample varies while Z is constant, more Rutherford scattering will occur in the thicker regions. Both Z and thickness therefore contribute to contrast in the same way, which is why this is called mass-thickness contrast. In BF image,s areas of increased mass and/or thickness will therefore appear dark. Regions that diffract more than others will of course also appear darker, which is why the crystal orientation of a sample will affect BF images.

Bent samples can be considered as a collection of crystal grains that vary very smoothly in orientation. Figure 2.18 illustrates how a bent sample may be considered as segments of constant orientation, and how the reciprocal lattice of each segment will intersect with

the Ewald sphere. In this example a sample has a surface normal that varies smoothly, and when this normal is anti-parallel to the incoming beam, the sample is on zone and scatters strongly (case I). As this area scatters a lot it will appear dark in BF images. In case II) the same planes still scatter, but they scatter far less as the Ewald sphere intersects only the very end of the CTR. Finally in case III) the planes that previously scattered are completely out of Bragg, and does not scatter, causing this area to appear bright in BF. However, other CTRs in this area are close to be in Bragg, and further bending may cause the intensity in the BF image to drop

DF imaging

An alternative to filter out all scattered electrons from the image, is to include only scattered electrons. One way of doing this is to insert an objective aperture as if one were to do BF imaging, but centre this aperture on a diffracted beam instead. In this way, only electrons scattered to a specific angle will contribute to the final image. Because only electrons having passed through an area containing a specific spatial frequency contribute to the image, the final image can be considered as a frequency filtered image. Imagining that the sample in Fig. 2.18 is not bent, but contain discrete grains instead, the concept and power of DF imaging becomes clear. If one does DF imaging of the red and/or blue CTR in this illustration, the areas I) and II) will light up, with I) being the brightest. At the same time areas containing orientation III) will appear dark. The contrast of DF images is therefore usually opposite of BF images. In the case of structural/orientational domains, DF imaging is extremely powerful because different domains in such a sample may produce separate reflections in a DP. These reflections may then be used to image the shape and size of each domain.

HAADF STEM

An annular detector can be used to acquire the CBED patterns generated during STEM. A high angle annular dark field (HAADF) detector will measure the total intensity scattered into a certain range of angles. For each STEM probe position the total number of electrons scattered to a certain range of angles is recorded. Which angles are detected is governed by the HAADF detector size and more importantly by the camera length L. This parameter is defined as the effective distance between the specimen and the detector, and determines the distance between reflections in a DP. Therefore the distances in the STEM CBED pattern can be changed while keeping the HAADF detector and sample in fixed positions. Choosing a short camera length will make mostly electrons scattered to high angles hit the HAADF detector. A long camera length makes the detector record electrons scattered to lower angles. If using a short camera length, mostly electrons having suffered Rutherford scattering will be detected, yielding images with high Z contrast. STEM HAADF images are capable of yielding Z contrast with resolution below the nm scale, as the results of e.g. Nord *et al.* [62] illustrate.

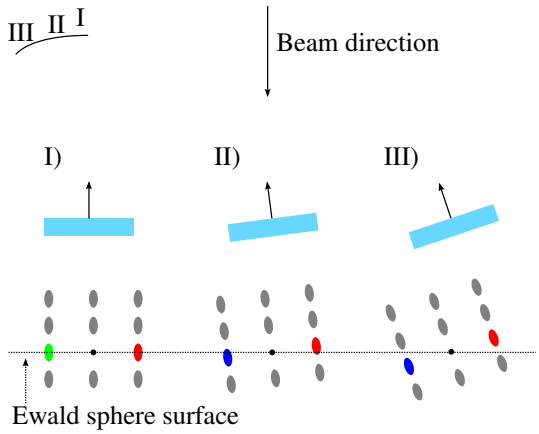

Figure 2.18: Illustration of bending contrast in TEM. In the upper left corner a drawing of the sample geometry is shown, with three regions labelled. The surface of the Ewald sphere has been drawn as a horizontal dashed line. Segments from these regions are shown as blue rectangles, with their surface normals pointing in slightly different directions. Below each segment a part of the samples reciprocal lattice is drawn, the dense dot marking the (000) point in each. In I) the plane corresponding to the red and blue CTRs scatter strongly and this segment will appear dark in BF and bright in DF. The same plane will still scatter in segment II) but the intensity will be much lower, causing a decrease in DF contrast and an increase in BF contrast. Finally in III) the plane no longer diffracts at all, and the area with this orientation will be bright in BF and dark in DF.

Energy dispersive spectroscopy

When an atom is illuminated by photons or electrons with a high enough energy, internal excitations within the atom may occur. These excitations are discrete and unique for every element. This non-elastic scattering mechanism causes the atoms to radiate x-rays that serve as a fingerprint, and can be used to determine the chemical composition of a sample [23]. The TEM is an excellent tool for this task, as long as the sample can survive vacuum and the high energy electrons. By inserting an energy dispersive detector close to the sample, x-rays of different energies can be separated and counted individually. One can either operate the TEM in regular imaging mode and acquire energy dispersive spectra (EDS) from large areas, or one can operate the TEM in STEM mode and acquire a spatial map of the chemical composition of the sample. Tables such as the one by Center for X-ray optics (CXRO) [63] contain experimental data on the allowed transitions for elements $3 - 95$ and can be used to index EDS.

2.4.2 Phase contrast

Phase contrast arises due to interference between scattered and unscattered beams. By using an annular bright field (ABF) detector in STEM mode it is possible to image lighter atoms, and is a result of a complicated interference process between the diffracted beams. However this technique require great skill and advanced equipment. A simpler, but still powerful and commonly used phase contrast technique, is HRTEM.

High resolution

HRTEM creates an image that is the result of complex diffraction and interference in the electron beam, i.e. it images the phase difference of the transmitted electrons. This phase difference is strongly connected with the specimen's crystal lattice and structure. Because the lenses in the TEM are somewhat crude and imperfect as well as finite in size, HRTEM will image a point in the sample as Gaussian distribution, and the resulting image is sensitive to the overlap of these distributions. In other words, the image will be described as the convolution between the specimen and the instruments point spread function. Letting the functions $g(\vec{r})$, $f(\vec{r})$, and $h(\vec{r})$ represent the image, sample and the point spread function of the image respectively, the image can be expressed as

$$g(\vec{r}) = f(\vec{r}) \otimes h(\vec{r} \tag{2.21}$$

If $G(\vec{u})$, $F(\vec{u})$, and $H(\vec{u})$ are the Fourier transforms of g, f and h respectively, the following relation is obtained through the convolution theorem:

$$G(\vec{u}) = F(\vec{u}) \cdot H(\vec{u}). \tag{2.22}$$

$H(\vec{u})$ is called the contrast transfer function (CTF), and limits the frequency range of $G(\vec{u})$. How the apertures, wave attenuation, and lenses affect the beam is incorporated in $H(\vec{u})$. Equation 2.22 means that the frequencies in the sample will be preserved in the image, below a certain "cut-off" decided by the point spread function.

The CTF may be simplified if the sample is sufficiently thin. In what is called the Weak Phase Object Approximation (WPOA) where the sample is approximated as

$$f(x,y) = 1 - \mathrm{i}\sigma V_t(x,y), \tag{2.23}$$

where σ is the interaction constant and $V_t(x,y)$ is the projection of the sample potential along the beam direction of a very thin sample. In this approximation absorption is neglected, which is reasonable when the sample is very thin. It should be noted that "very thin" is a rather relative term. For instance, the thinnest possible sample of Uranium one can imagine is a single monolayer, but even this is a too thick "sample" for the WPOA to be valid. In the WPOA the CTF may be represented as

$$T(\vec{u}) = 2E(\vec{u})\, A(\vec{u}) \sin\left(\chi(\vec{u})\right), \tag{2.24}$$

and it is now called the objective transfer function. E represents the envelope aspect of the function, and the effects of apertures are contained in A. The phase-distortion function $\chi(\vec{u})$ contain information of spherical aberration C_s and defocus Δf, and can be expressed as

$$\chi = \pi \Delta f \lambda u^2 + \frac{1}{2}\pi C_s \lambda^3 u^4. \tag{2.25}$$

Figure 2.19 show a plot of $2\sin\left(\chi(u)\right)$ for certain defocus and spherical aberrations. When this quantity is larger than zero, atoms will appear as bright spots, and dark if it is less than zero. The figure helps to illustrate the fact that the microscope settings, i.e. the defocus and spherical aberration, affect the contrast in a HRTEM image. Interpretation of

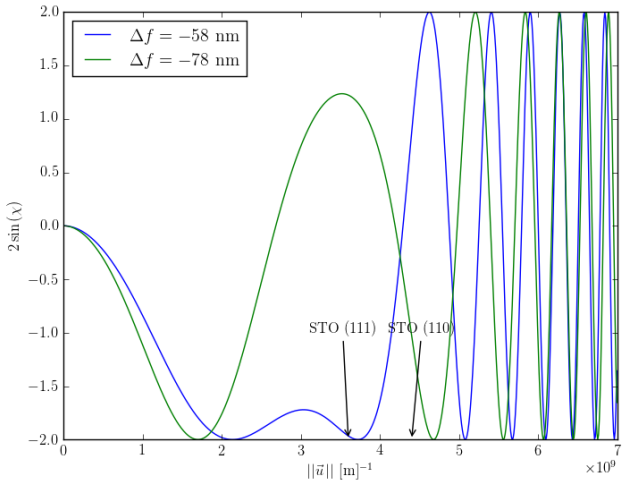

Figure 2.19: Example of the oscillatory property of an objective transfer function with $\lambda = 0.00251$ nm and $C_s = 1$ mm for two different defocus values $\Delta f = -58$ nm (blue) and $\Delta f = -78$ nm (green). The reciprocal values of STO (111) and (110) are shown to provide some reference.

HRTEM images is therefore not straightforward, and simulations are needed to interpret this kind of images. If one is only interested in the spatial frequencies of a sample, FFTs of a HRTEM image can be a powerful tool as the lowest spatial frequencies of a sample are preserved in a HRTEM image.

Chapter 3

Experiment

3.1 Material synthesis

Thin films of LFO on (111) oriented STO was synthesized by PLD at the Department of Electronics and Telecommunication (IET), NTNU, by Ingrid Hallsteinsen. As the synthesis of thin films is not the focus of this thesis, details concerning the growth is omitted. In short, PLD works by generating a plasma of a target by exposing it to an intense laser in short pulses. The target contains the elements one wish the film to consist of. The substrate onto which the film is to be grown is positioned relatively close to the target. In order to give the adatoms from the plasma a possibility to move around before nucleating, the substrate is heated to a certain temperature. Both the target and the substrate are held in a vacuum chamber, in which a small amount of gas (e.g. oxygen) may be present. The atoms in the gas will participate in the growth of the film. By examining the substrate continually by Reflection high-energy electron diffraction (RHEED), one are able to estimate both the quality and thickness of the film during growth [64].

Table 3.1 presents an overview of the different samples studied in this thesis. The film name is the one given by the growers at IET. Samples made from the various films have received names to separate them. A sample "F$x.y$" is referred to as sample number y of film number x. Their geometry and the sample preparation technique used for each are explained in the table, for FIB CS sample the surface normal of the sample is also given.

The growth temperature of the films studied in this thesis was 540 °C. An oxygen pressure of 0.35 mbar was used and the substrate-target distance was 45 mm. A substrate miscut of 0.1° was used to control step edges. These step edges are along the $< 11\bar{2} >_{STO}$ directions. Atomic force microscopy data of the films (except for F1) are presented in Appendix A, along with x-ray diffraction (XRD) data from F4. According to the growers the surface of LFO thin films have a tendency to crack when reaching a certain thickness [19, 20]. Small square wafers of roughly 25 mm^2 and ~ 0.5 mm were provided for TEM studies of the films. When received from IET, the crystallographic orientation of the film

Table 3.1: The samples studied and the methods used for sample preparation. * marks samples which were heated at 150°C after having been thinned. $[hkl]$ are STO indices.

Film name	Sample name	Geometry and method	Comments
p41204	F4.6	CS, FIB $[1\bar{1}0]$	Ruined during sample preparation
p41204	F4.5	PV, Tripod+FIB	Not investigated by TEM
p41204	F4.4	PV, Tripod+FIB	
p41204	F4.3	PV, Tripod+FIB *	
p41204	F4.2	CS, FIB $[1\bar{1}0]$	Ruined during sample preparation
p41204	F4.1	CS, FIB $[11\bar{2}]$	
p40903	F3.1	CS, FIB	Thickness is > 30 nm
p40207	F2.2	Cs, Tripod, PIPS, CAIBE	Sample not electron transparent
p40207	F2.1	PV, Tripod	
p30804	F1.2	CS, Tripod	
p30804	F1.1	PV, Tripod	

was sometimes given, enabling preparation of samples for specific zone axes.

Not all samples have been studied in the same detail. F1.1 was made primarily with the purpose of learning the sample preparation method, and was not thought to be of much interest until a much later stage. Hence, no results from this sample is presented. Sample F2.1 did not receive much attention either, due to its relatively poor quality. F2.2 was also of very poor quality, and it was attempted to improve this by ion milling, but not much effort was put into this sample. In Appendix D the ion milling procedure and some TEM images of this sample are presented. Sample F4.5 was finished at the very end of the thesis, and there were no time to study this sample. Samples such as F4.2 and F4.6 was destroyed by sample preparation, and TEM images of these are also presented in Appendix D. Sample F4.1 and F4.3 are the samples that have been most studied in this thesis.

3.2 TEM Sample preparation

In order to prepare TEM samples of the wafers received from IET, two main techniques were applied. Some samples were prepared by mechanical polishing using a tripod polishing system, while others were prepared by ion milling in a focused ion beam (FIB) instrument. A combination of the two procedures was applied to some samples.

The first step in order to prepare samples was to cut the sample wafers into suitable pieces (long slabs of 1×5 mm^2 for preparation purely by FIB and small pieces $\sim 1 \times 0.8$ mm^2 for tripod) using a *Testbourne Model 60 Low Speed Diamond Wheel Saw* equipped with a 0.5 µm thick *Allied Wafering Blade*.

3.2.1 Tripod polishing

Tripod polishing is a mechanical sample preparation route that has shown promising results for perovskite materials [7, 65]. The preparation scheme used in this thesis follows that of Monsen in general, and the reader is referred to his master thesis for details concerning the procedure.

Figure 3.1a illustrates the principle of the *Allied MultiPrep System*, a polishing system that provides a precise and reproducible way of preparing TEM samples. A rotating platen and an arm form the main components. Different polishing media can be attached to the platen, and a removable paddle can be attached to the tripod arm. On this paddle a pyrex stub is fastened, which may be polished to provide a reference plane. A sample is then polished by attaching it to the pyrex stub of a tripod paddle as illustrated in Fig. 3.1b, and by lowering the arm with the mounted paddle, onto the rotating platen. A load between $0 - 500$ g can be applied to the arm, allowing polishing of both hard and sturdy, and delicate and brittle materials to be polished. A micrometer dial is used to control the amount of material removed *in situ*. The arm can be laterally moved by the system automatically, in order to utilize more of the DLF, while at the same time reducing the chance for dislodged material to ruin the sample. Continuous rinsing of the polishing media with water is possible through a flexible water tap, further reducing the chance of debris to ruin the sample. A pair of micrometre screws can be adjusted to introduce a wedge in the sample with respect to the polished reference plane of the pyrex stub. Such a wedge will be electron transparent at its tip if prepared correctly, the wedge angle determining the amount of electron transparent area and the strength of the sample.

Two different sample geometries were prepared by tripod, PV and CS. PV samples were prepared by gluing a piece cut from the sample wafer to the pyrex stub using acetone soluble glue, with the substrate facing up. The sample was then polished from the substrate-side with a wedge angle of $2 - 4°$. Starting with relatively rough diamond lapping films (DLFs) of $15 - 3$ µm, the substrate material was polished off to form a wedge as in Fig. 3.1c. To thin the wedge further to electron transparency DLFs of 1, 0.5, and 0.1 µm were used in decreasing roughness. In these steps *Allied GreenLube Polishing lubricant* was used to reduce cracking and scratches in the surface. The 1 µm DLF was used until the sample edge was at the region of interest (ROI), meaning that the sample should not be too ”big” to fit on the TEM grid, or the sample started to show thickness fringes. Using 0.5 µm DLF the sample was polished to further enhance the thickness fringes. It was discovered when polishing the later samples that the 0.5 µm DLF should be avoided as the tip of the sample often cracked when using this DLF. The 0.1 µm DLF was used until the thickness fringes were extensive, as in Fig. 3.2a. A filt cloth stained with *Allied* 0.02 µm *colloidal silica suspension* was used to give the samples a finish, with the result that the edge became much smoother and the fringes being even more pronounced, as seen in Fig. 3.2b. The colloidal silica was removed by applying cotton sticks soaked in *Allied Micro Organic Soap* diluted 2% in deionized (DI) water, and thorough rinsing with DI water.

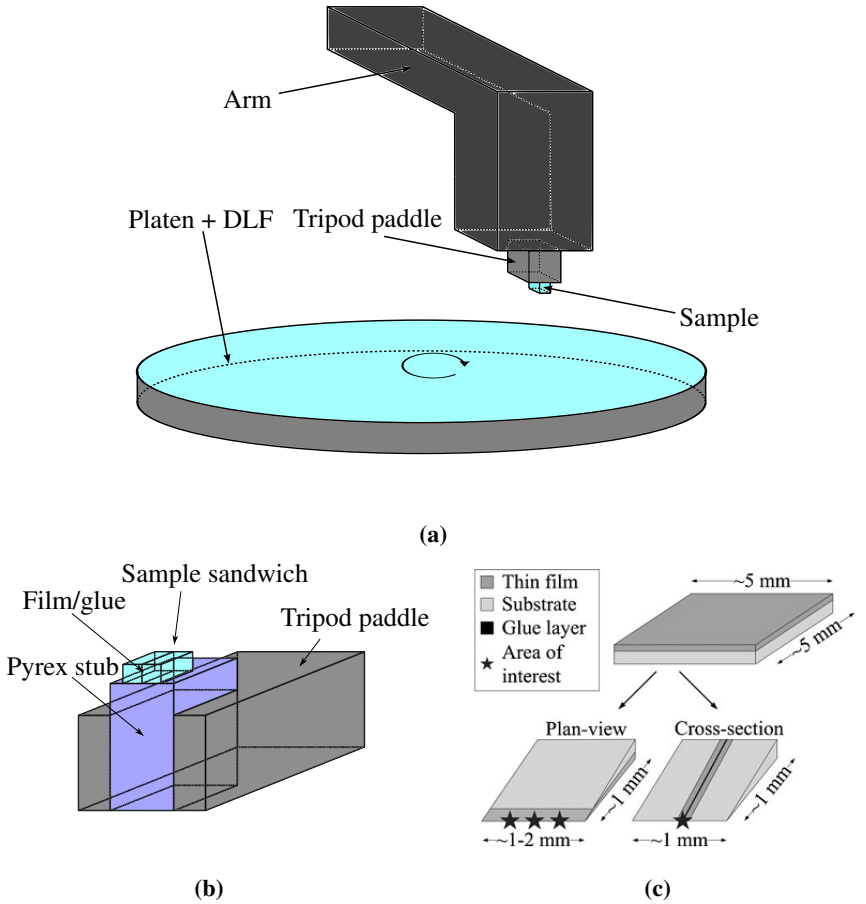

Figure 3.1: Illustration of sample preparation geometry by tripod. In a) the tripod system itself is illustrated. A polishing media, e.g. a DLF is attached to a rotating platen, while the tripod paddle such as the one sketched in b) is attached to a movable arm. The arm can be lowered so that the sample (or pyrex if no sample is attached) comes into contact with the platen. The angle the paddle makes to the platen can be adjusted using a set of micrometer screws (not shown), thus enabling the preparation of wedged samples. The arm can be made to sweep the platen radially in a periodic way, causing the radial position of the sample with respect to the platen centre to oscillate. A sketch of a sample sitting on the pyrex stub of a tripod paddle is shown in b). In this case the sample has a cross sectional geometry. In c) an illustration taken from [65] of the two different geometries of PV and CS specimens prepared by tripod polishing is presented. The ROIs of each sample are marked with star(s). These sketches are meant for illustrative purposes only, and are as such not made to scale.

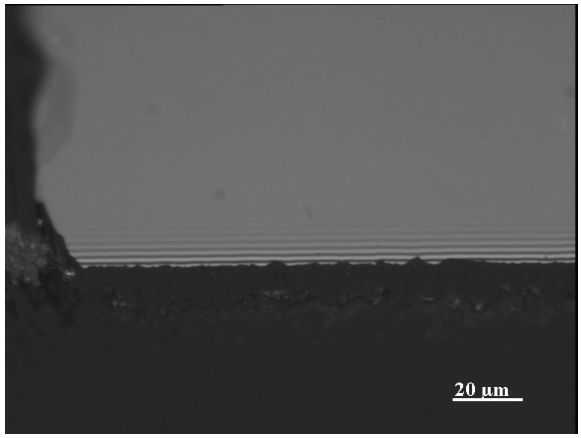

(a)

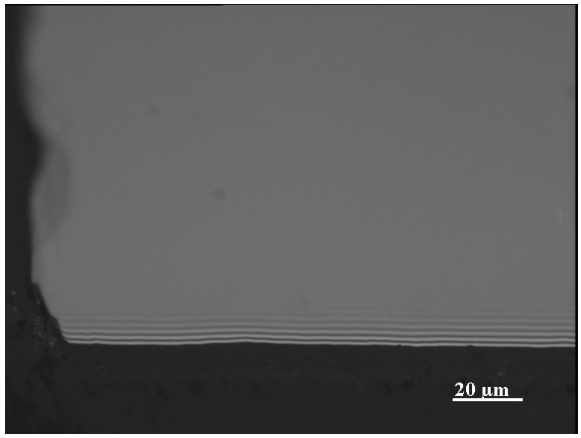

(b)

Figure 3.2: VLM images of F4.5 before (a) and after (b) the finishing step of polishing with a colloidal silica stained filt cloth.

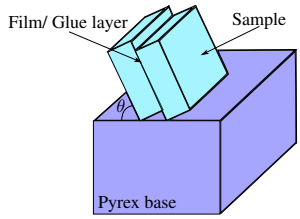

Figure 3.3: Illustrative sketch on CS sample on pyrex base of tripod paddle. Due to the two misaligned sandwich halves, the sandwich sits skew on the pyrex when polishing the reference side, thereby introducing an angle θ which needs to be compensated in the TEM to reach the desired edge-on view.

Preparing CS samples involved making a sandwich of two wafer pieces by gluing them film-to-film with *Allied 2-bond Epoxy* glue. The sandwiches were put in a clamp to apply pressure in order for the resulting glue layer to be as thin as possible, and cured on a 150 °C hot plate for $\sim$ 2 hrs. After the glue had cured sufficiently the sandwiches were glued on pyrex stubs with the sandwich interface normal to the pyrex surface, with acetone soluble glue, yielding a geometry as in Fig. 3.3. A reference side of the sandwiches was polished by following a similar procedure as for PV samples, but with no wedge angle introduced, and not with the intention of thinning the samples. After a scratch-free reference side had been polished using DLFs of decreasing roughness, and finishing by a colloidal silica stained filt cloth, the sandwiches was detached from the pyrex stubs using acetone and re-glued with their reference sides facing the pyrex. The samples were then polished in the same way as the PV samples. Figure 3.4 show VLM images of different magnification of sample F1.2. For CS samples only the interface region is required to be thin and smooth. However only one side of the interface at the tip is intact in this sample, reducing the possible area to study in the TEM by half.

Before gluing any two surfaces together, both were cleaned with acetone and ethanol. Inspection of the surfaces in a VLM was done in order to ensure that no debris or dirt was present.

TEM half-grids were glued to the polished side of the samples using epoxy glue while they still were attached to the pyrex stub. The glue used for some samples required thermal hardening and the pyrex stub was put on a hotplate of 150 °C. These samples have been marked with an asterix in Table 3.1. For the unmarked samples, *Araldite* epoxy glue was used, which did not require thermal hardening.

PV samples were much easier to make because the CS samples had a tendency to crack at the interface. The electron transparent area of the ROI PV samples are also much larger than the very small ROI of CS samples, therefore more PV than CS samples were successfully prepared.

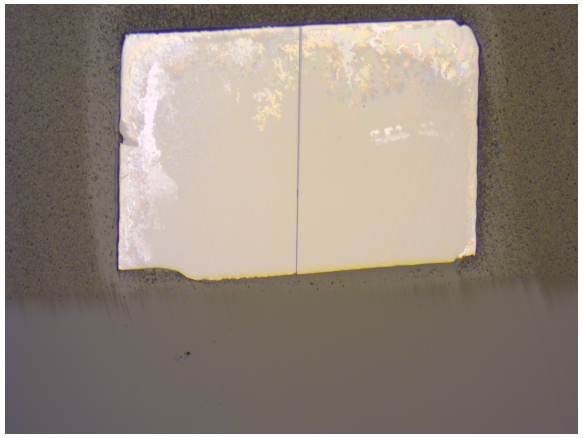

(a)

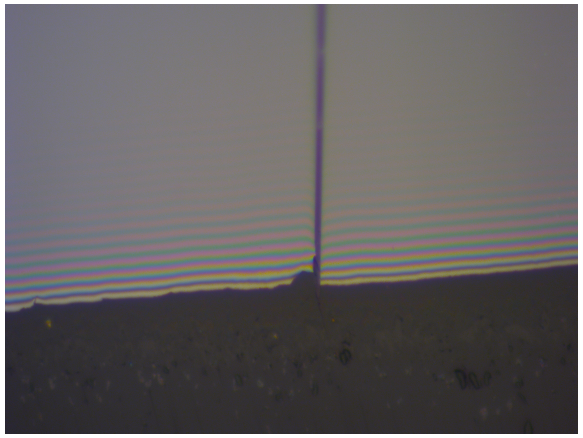

(b)

Figure 3.4: VLM images of different magnifications of finished F1.2. At the ROI one small piece of the sandwich has fallen off, thus reducing the possible area to study in the TEM by half.

3.2.2 Focused Ion Beam (FIB)

The NTNU NanoLab is in possession of an advanced *FEI Helios NanoLab DualBeam FIB* that is excellent for preparing TEM specimens. This instrument is a combined scanning electron microscope (SEM) and a FIB. The SEM creates an image of a sample by recording backscattered electrons, X-rays, and so on. The FIB uses Ga ions at relatively high energies to mill and/or perform destructive imaging. The workings of these instruments are beyond the scope of this work, and will not be discussed or presented in detail. Instead some of the most important aspects of the sample preparation are outlined.

In perovskite STO the Ga ions from the FIB will tend to leave an amorphous layer of ~ 1 nm$/1$ kV. Therefore protective layers were deposited on the samples in order to protect their crystalline properties, before turning on the FIB source. When preparing samples of F4 the wafer piece was first coated with a ~ 3.0 nm layer of Pt/Pd (80/20) using a *Cressington Sputter Coater Model 208 HR B* in an attempt to further protect the film against stray Ga ions. By introducing gases in close proximity to the surface of a sample within the vacuum chamber, elements in this gas can be made to condense on the surface in a pattern determined by the user. The energies of either the electrons in the SEM or the ions in the FIB can separate the various elements in the gases, and high precision deposition of amorphous/polycrystalline materials can be achieved. The FIB can also be made to mill away material. Using high ion beam currents usually leads to inhomogeneous milling. The imaging, milling and deposition qualities makes the FIB a very versatile tool in nanotechnology.

In the FIB instrument used during this work the SEM and ion gun is angled 52° to each other, making it possible to observe the object one is milling in or depositing on from two different directions at the same time. A high precision movable needle-like *Omniprobe AutoProbe* probe of W provides the possibility to lift and move tiny objects within the FIB, by welding them to this probe. The FIB require much training and experience, as well as having a heavy user load. The preparation was therefore done by Magnus Nord. This section seeks to illustrate the principles of the procedures used.

Cross section samples

Figure 3.5a illustrate the half grid used to attach samples and how a notch must be made in this to make room for the sample itself. The illustration in Figure 3.5b show the geometry of a finished FIB CS sample from two different angles. In order to explain the procedure a short explanation of the various steps is presented, before a more detailed presentation is given.

For CS samples the film surface of small slabs cut from the wafers were put into the FIB, together with an array of TEM half grids. The lift-out procedure was as follows:

1. A thin protective layer of carbon and subsequently platinum was deposited on the desired area of the film side of the wafer slab, using the non-destructive electron beam (see Figs. 3.6b and 3.6c).

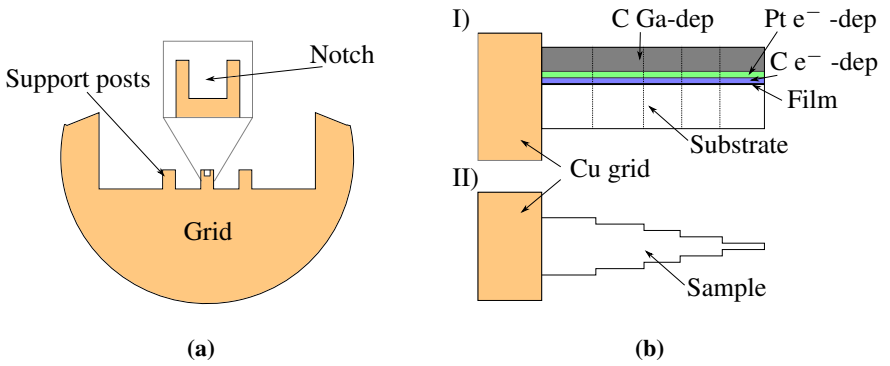

Figure 3.5: Schematic of a) the grid for FIB CS samples showing the notch made in one of the posts, and b) the FIB CS sample geometry seen from two different angles I) from the side, i.e. the geometry seen by the electrons in the TEM, and II) from above. Green and blue layers refer to Pt and C layers deposited by the electron beam in the FIB respectively. Dark gray area are the protective C layer deposited by the ion beam. Dotted lines in I refer to the thickness steps, in accordance with II.

2. A thicker layer of carbon was deposited on top of the thin layer by the Ga beam (see Fig. 3.6d).

3. Several ”ditches” were dug straight down through the film and into the substrate around the protected area (see Figs. 3.7b and 3.7a).

4. A ”J-cut” was performed to separate the piece covered by the protective layer from the rest of the sample wafer, except from a small ”bridge” (see Figs. 3.7c and 3.7d).

5. The AutoProbe was attached to the protective layer by depositing some Pt with the electron beam, and the bridge was cut so that the sample could be lifted out of the wafer (see Fig. 3.8a).

6. The TEM grids (actually FIB half-grids) was then located, and a small notch was dug in one of the support posts (see Figs. 3.5a and 3.8b).

7. The probe with the sample still attached was lowered into the notch, and the sample was fastened to the grid using Pt before the probe was cut off (see Figs 3.8c and 3.8d).

8. A series of milling steps were then performed, shaping the sample into a double staircase being very thin at the tip (see Figs. 3.9a and 3.9b). To reduce the inevitable amorphous layer introduced by the Ga beam, the last thinning was done using reduced voltages.

Figures 3.6-3.9 show SEM images of the preparation of F3.1 by lift-out in the FIB. The overview SEM image in Fig. 3.6a show the $\sim$ 498 µm wide slab of the sample wafer with the film facing upwards on a piece of sticky tape inside the FIB. On this slab a thin, rectangular ($\sim 2 \times 12$ µm) layer of carbon was deposited by the electron beam as shown in Fig. 3.6b. Figure 3.6c show the similar layer of platinum (2×12 µm) which was

subsequently deposited on top of the thin carbon layer. A third layer consisting of carbon was deposited on top of the first two layers by the ion beam and is shown in Fig. 3.6d. This layer provided the thick protective layer necessary when doing the thinning steps in this procedure.

Ditches measuring $\sim 22 \times 15$ µm shown in Figs. 3.7b and 3.7a were dug on the two long sides of the protective layers shown in Fig. 3.6. These ditches allowed for a "J-cut" to be made, as indicated and shown in Fig. 3.7c and Fig. 3.7d. A small "bridge" was left on one side so that the specimen was suspended and free from the rest of the sample wafer.

The specimen was welded with Pt to the AutoProbe and the bridge was removed as shown in Fig. 3.8a. By carefully retracting the omniprobe, the specimen was lifted out of the sample wafer. Figure 3.8b show a notch of ~ 24 µm wide was made in one of the Cu TEM/FIB grid support posts, and the omniprobe with the specimen was carefully lowered into this notch as shown in Fig. 3.8c. By welding the specimen to the inside of this notch with Pt, the geometry in Fig. 3.8d was achieved.

Thinning the specimen to electron transparency was done by making a double staircase geometry, shown in Fig. 3.9. In Fig. 3.9a a side-view of the finished specimen is shown. The angle of view in this image is along the same direction as the one that the incident electrons in the TEM will travel. An area of $\sim 6 \times 2$ µm is the ROI. This region appear bright because the volume of the sample in this area is smaller than that of the required reaction volume for the SEM, indicating that the sample is thin enough or nearly so for TEM. Figure 3.9b offer a top-view of the specimen, showing clearly the double staircase geometry, the steps being of $\sim 2 - 3$ µm in lengths.

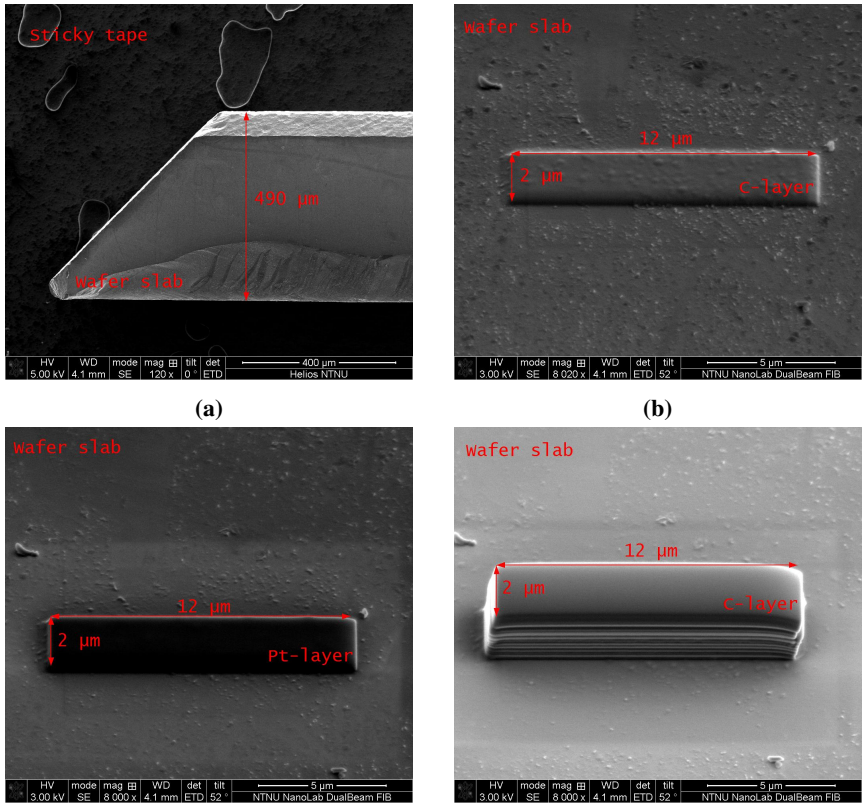

Figure 3.6: First steps of FIB sample prep of F3.1, a cross section sample, by lift-out. The image in a) show an overview SEM image of the sample wafer slab, and a piece of the sticky tape used to hold it still. In b) a thin layer of carbon has been deposited by the electron beam, while in c) a thin layer of platinum has been deposited on top of the carbon layer, also by the electron beam. On top of the electron deposited layers, a much thicker carbon layer has been deposited on top of the other two by the FIB as shown in d). The purpose of the first two layers is to protect the film from the ions used to deposit the last C layer. The last C-layer serves to protect the film from the ions when thinning the specimen.

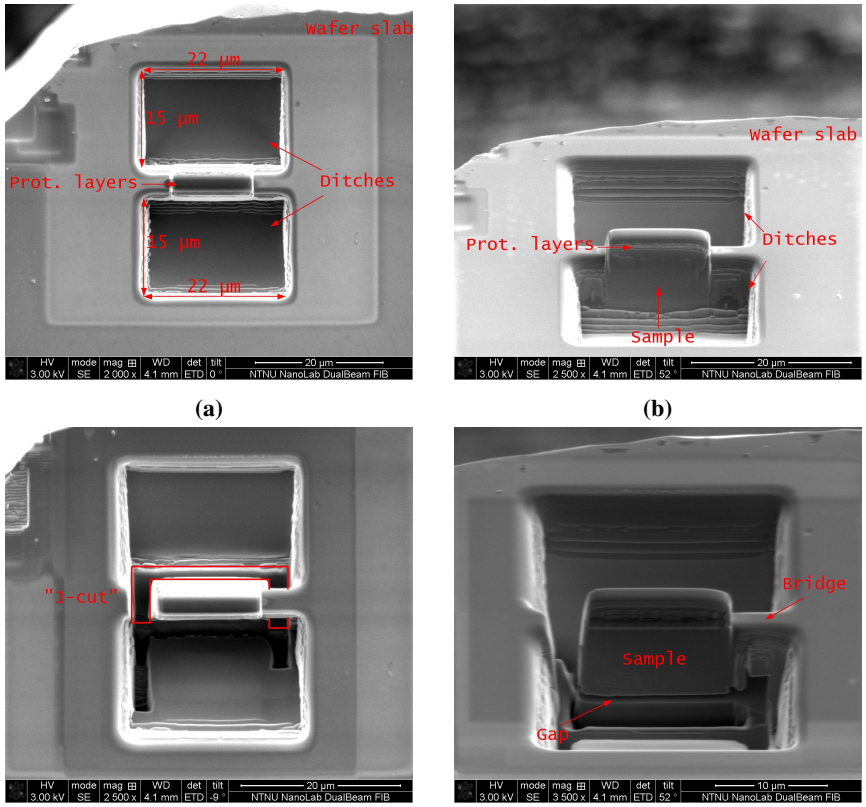

Figure 3.7: The digging steps of the preparation of F3.1 by lift out in the FIB. In a) a top-down view of the ditches is shown, while in b) a side-view is offered. The ”J-cut” has been performed in c) as outlined. The cut leaves the sample hanging by a bridge. in d) angled view of the sample wafer showing the specimen with its protective layer being supported by the bridge alone. The specimen has been cut from ”above and behind” by a ”J-cut”, separating it from the rest of the sample wafer.

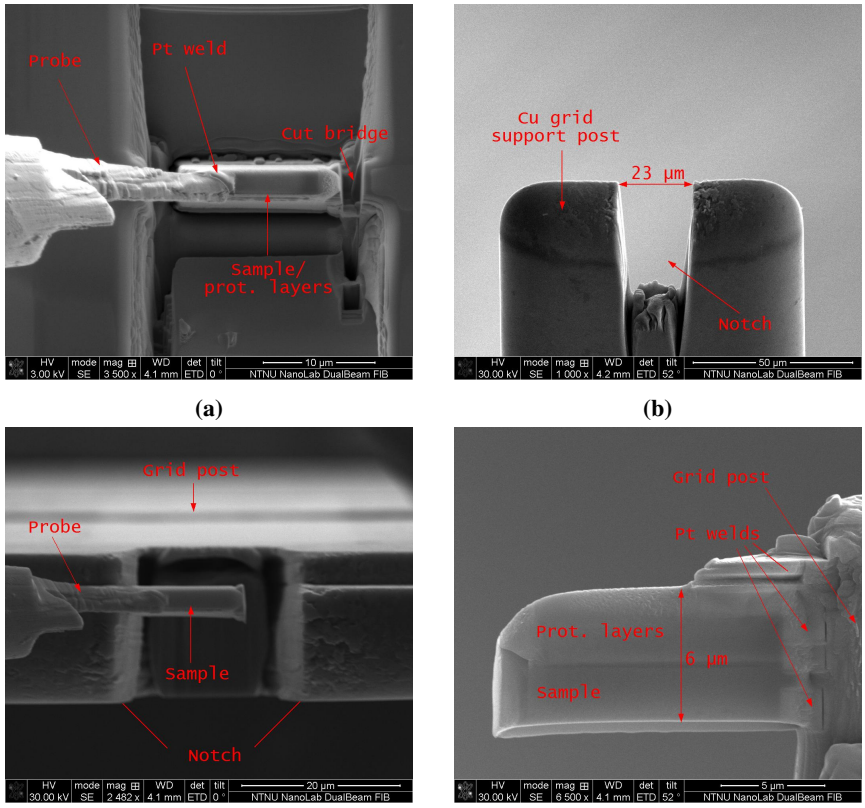

(a) **(b)**

(c) Top-view image of the specimen being **(d)**

Figure 3.8: SEM images showing the lift out process, notch prep. and the sample being welded to the grid. In a) the specimen has been attached to the omniprobe with a Pt weld before being lifted out. The bridge that was supporting the specimen has been cut, leaving the specimen to be solely held by the omniprobe. The slightly angled image in b) show the notch made with the FIB in one of the support posts of the TEM/FIB Cu grid. The specimen are to be attached to the inside of the notch. the notched support post of the Cu TEM/FIB grid. The sample are about to be attached to the Cu TEM grid post inside the notch by Pt welds in c). After it has been welded in place the probe was cut. d) show the attached sample from the side, ready to be milled from the top.

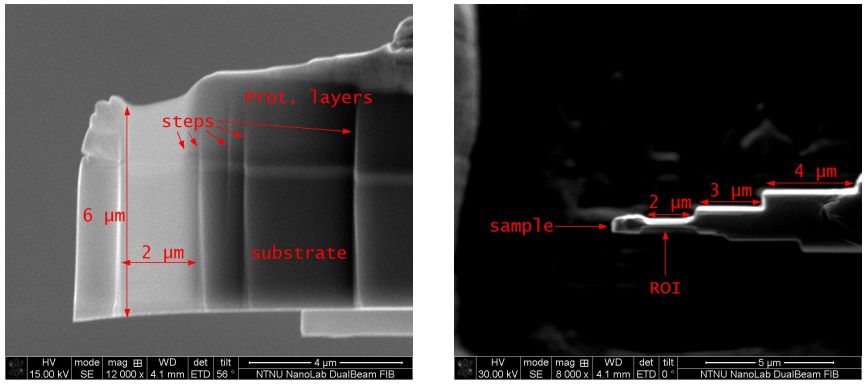

(a) **(b)**

Figure 3.9: The finished F3.1 specimen prepared by lift-out in the FIB, a) from a top-view and b) from a side-view.

Plan-view samples

The major problem with tripod samples in general is that the thinnest and best parts of the sample are quite bent, and the contrast in TEM images can be difficult to interpret. To improve tripod PV samples by FIB, a similar FIB thinning approach as was used for CS samples was followed. However, in this case no lift out was required. An important part of this procedure was to ensure that the Ga beam never faced the film side, as this would destroy the film. Observation of specimen thickness is achieved by the SEM which faces the film side at $\sim 52°$, while the Ga beam faces the wedge edge straight on.

Figure 3.11a show a SEM image taken from the substrate side of F4.3 with the notch pointed out. Images of this sample taken through the sample prep. process will be presented through this section to illustrate the different steps. In the image some ditches on the left side are visible. These were made in preliminary attempts to produce electron transparent areas far into the tripod wedge where the surrounding material was thick enough to keep the thin area from bending. These tests revealed the need for depositing a protective layer so that milling could be done nearly edge on. In order to deposit the protective layers the edge had to be wide enough.

A wider edge was accessed by milling out a notch in the sample using 30 kV and 6.5 nA ion beam parameters at an angle of $-9°$ ($0°$ being parallel to the film). Figure 3.11b show a close up SEM image of the $\sim$ 53 µm wide notch in the tripod wedge of the sample, which is $\sim$ 15 µm deep. A positive consequence of this is that the tripod wedge is much more stable and smooth this far inside, providing a better chance for a smooth PV ditch. Afterwards the sample was rotated and tilted to $52°$, and a protective layer of $\approx$ 1.2 µm C was deposited using the electron beam onto the new edge (using 3 kV, 2.7 nA SEM parameters). Next, the sample was rotated again to bring the film surface to face the SEM, and tilted to $44°$. A $\sim$ 3 µm thick layer of C was then deposited with the ion beam using

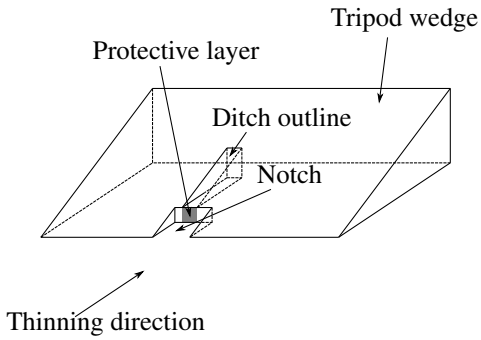

Figure 3.10: Illustration of the geometry of PV improvement by FIB. The notch is made in order to access a sturdier and "flatter" area of the sample. A protective layer is deposited before digging begins. Ditches, such as the one outlined, are dug sequentially so that the thickness decreases. The film is facing "down" in this figure.

30 kV and 0.49 nA. The deposited $\sim$ 17 µm wide protective layer is seen in the middle of the notch in Fig. 3.11b. Ditches were dug "edge-on" in order to thin down the sample by tilting the sample to 46°. Figure 3.10 illustrates the principle while Fig. 3.12 presents SEM images of the ditch during the process. The ditches were made successively so that the thickness of the sample decreases step by step. Ion beam voltages and currents of 30 kV and 0.26 nA were used initially, but were reduced to 5 kV and 0.13 nA when the sample measured $\sim$ 100 nm. Eventually, a large area of electron transparent film+substrate was produced, with little to no bending or thickness variation.

3.3 TEM experiments

The TEM Gemini centre at NTNU is in possession of four TEMs, one W thermionic TEM *Philips CM30*, a LaB_6 thermionic *JEOL JEM-2100*, a Schottky FEG *JEOL JEM-2100F*, and double corrected cold FEG *JEOL ARM-200F*. In this study the author has been conducting experiments on the JEM-2100 and JEM-2100F, and Magnus Nord has acquired data with the ARM-200F. All instruments were operated on 200 kV, and double tilt holders with tilting ranges of $\pm 30°$ were used.

The JEM-2100 (referred to as the 2100 microscope) was equipped with a *Gatan 2k Orius* CCD camera, along with a *Gatan Imaging Filter* (GIF) system with a 2k CCD camera. TEM images on the JEM-2100F (referred to as the 2100F microscope) was acquired with a *Gatan 2k UltraScan* bottom mounted CCD camera. HAADF STEM experiments were also conducted on this microscope. HRTEM images and EDS data were acquired on the ARM-200F (referred to as the ARM) by Magnus Nord using a *2k Orius CCD* camera and a *Centurio SDD EDX*, respectively.

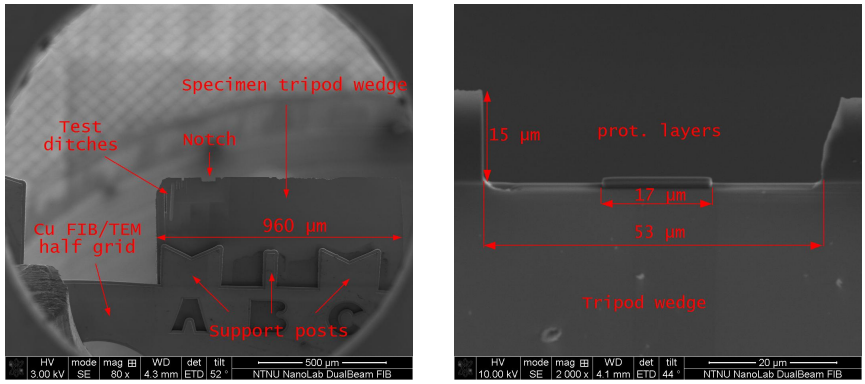

(a) **(b)**

Figure 3.11: SEM images of the preparation of protective layers of the tripod wedge sample F4.3. In a) an overview image facing the substrate side of the tripod wedge is shown. Some trial ditches were dug in the left part wedge to explore different kinds of ditches. A notch was made into the wedge to provide a stable surface for protective layers to be deposited onto in order for a "low-angle" digging sequence to be performed without damaging the film. b) SEM image of the C/C protective layers on the notch edge. The notch depth and width are ≈ 15 µm and ≈ 53 µm respectively. The protective layers are ≈ 17 µm wide, and ≈ 1.6 µm thick. Note that the image is taken with an angle to the layers, and the measured thickness is not the true thickness. The layers have been deposited at a slight angle due to restrictions in the FIB. The film is facing the SEM in this image.

Selected Area Electron Diffraction Patterns (SAEDPs) were acquired by operating the TEM in diffraction mode as explained in the theory chapter. The camera lengths used were 15.24 cm and 50 cm (uncalibrated) on the 2100 and 2100F, respectively. Camera length calibrations on the 2100 were conducted by the author, yielding the plot in Appendix B. In the DP presented in this thesis, reflections due to A, B, and C domains are marked with blue, green, and red circles/arrowheads, respectively, with indices and directions common to all LFO domains e.g. $[202]_{LFO}$ in yellow. STO indices and directions are in teal. This convention is used throughout this thesis.

When doing DF imaging, the diffraction focus was adjusted in order to focus the objective aperture. This caused the diffraction spots to be out of focus, which was solved by collecting the beam. Therefore the DF images in this thesis are acquired with a slightly larger convergence angle than what is ideal. To acquire proper DF images, the beam is tilted before it hits the sample, so that the diffracted beam travels along the optic axis. For PV samples, mosaics have been made from the different DF series. The mosaics are meant to illustrate the complete jigsaw puzzle of the different DF images. A, B, and C sensitive DF images have been coloured blue, green and red, respectively, when making the mosaics. *Gatan Digital Micrograph Suite* [66] (DMS) was used to threshold and colour the mosaics. The DMS software was also used to enhance contrast and to apply fast Fourier transform (FFT) routines to other images. FFT analysis and filtering have been used to investigate the frequency aspects of HRTEM and STEM images. HRTEM imges of CS samples have been rotated so that the substrate is on top, and the film is below. Inset DPs are rotated

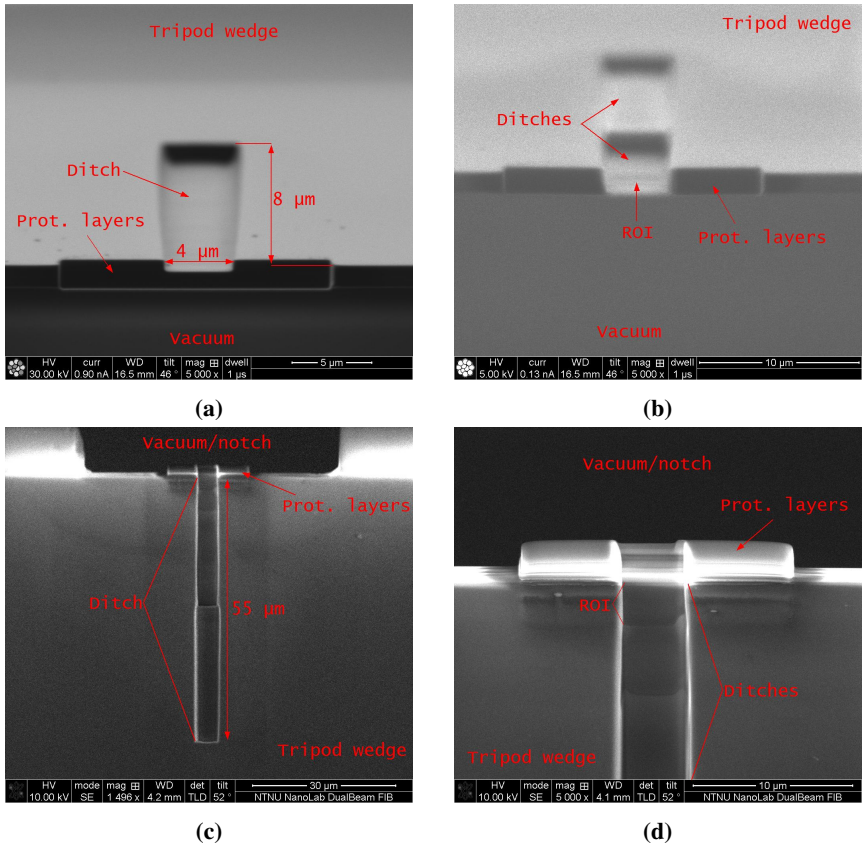

Figure 3.12: SEM images showing the thinning steps of FIB improvement of F4.3. a) FIB image of the first ditch as seen from the notch (digging direction) with the film facing down. The ditch measures ≈ 4 µm wide and the apparent length is ≈ 8 µm. Due to the angle of view this length is a vast underestimate. b) FIB image from the same angle as a) showing the ditches after preparation is complete. The acceleration voltage of the ions used to both dig and image at this point has been set quite low (5 kV) in order to reduce the amount of material becoming amorphous, but also yielding reduced image quality. In c) an overview SEM image of finished ditches is presented. The real length of the ditch is measured to be ≈ 55 µm, which is ≈ 6.9 times longer than the length measured in Fig. 3.12a. The film is facing away from the SEM in this image. d) SEM close-up image of the ROI of the ditch with the film facing away from the SEM. The contrast in the ROI indicate that the reaction volume in this region is reduced with respect to its surroundings. The ROI should be as dark as possible, with the protective layer still intact. More sessions was used to improve this sample further.

correspondingly.

Chapter 4

Results and discussion

In this chapter a presentation and discussion of the findings of the experimental work is presented. As can be appreciated from the few samples studied, there were several samples which were *not* studied. Therefore a discussion on sample preparation is first presented, concerning the various issues with TEM sample preparation. The intention of this specific section is to pass on some sample preparation tricks and warnings that might be useful for future work, and is not based on explicit results. Next follows a presentation and discussion on the step lines observed in PV samples. The third section is devoted to discussing the domain structure of the film. Finally, the film structure and quality is presented and discussed, where the substrate-film coupling is given special attention. The reason why the domain structure studies are considered before the crystalline quality of the films, is that the crystal structure and the coupling to the substrate is discussed in light of domains and domain boundaries. In the different images, the scale bar and eventual insets has/have been positioned so as to not cover interesting features, therefore their position is not consequent.

Several terms are used in the presentation of results and discussion, they are defined in the following way:

1. $\{hkl\}$ refer to a set of planes equivalent by symmetry.
2. (hkl) refer to a specific crystallographic plane.
3. $[hkl]$ are used for crystallographic directions.
4. $< hkl >$ refer to crystallographic directions equivalent by symmetry.
5. Dark lines observed within a domain are referred to as internal domain boundaries (IDBs).
6. Dark lines seen criss-crossing the sample surface at 60° are referred to as step lines.
7. A, B, and C refer to different orientational domains. These are defined to be domains with the long orthorhombic axis along the STO axis of corresponding lower-

case letter. The STO axes are however arbitrarily defined, and as such A, B, and C domains can not uniquely be established.

8. Blue, green, and red are used to annotate A, B, and C domain reflections respectively. Yellow is used for common LFO indices, while teal is used for STO indices.

9. In DF mosaics the A, B, and C domains are coloured blue, green, and red, respectively.

10. If no zone axis is specified for PV samples or FIB samples, the zone axis is $[111]_{STO}$ or the one indicated by Table 3.1 (i.e. at 0° tilt).

11. When the terms "outer" and "inner" reflections are used in connection with PV samples, it is referred to reflections with reciprocal lattice lengths $\left\|\vec{G}^{STO}_{1\bar{1}0}\right\|$ and $\left\|\vec{G}^{STO}_{11\bar{2}}\right\|$.

4.1 TEM sample preparation

4.1.1 Tripod issues

The yield rate of tripod CS samples of LFO/STO (111) was very low. Many samples were attempted, but only a single one became electron transparent. Most of the samples cracked and crumbled during sample preparation. Monsen and Eberg *et al.* suggests that this is due to too thick glue layers between the tripod pyrex and the sample wedge, and between the sandwich pieces [7, 65]. However, the LFO/STO material studied in the present work seemed to be extremely brittle and fragile. In the recipe from Monsen and Eberg *et al.* a wedge angle of 2° was used. Samples prepared using this angle cracked very easily. For the later PV samples increasing this angle to 4° increased the yield dramatically. It would be interesting to investigate how this increase in wedge angle affects the CS yield. It may be that LFO/STO (111) is much more brittle than LFO/STO (001), and that is the reason why an increase in wedge angle is beneficial.

Regarding the tripod polishing of TEM samples, one should pay special attention to the platen and DLF, as damages in these components can cause severe damage to the samples. When polishing with $0.5\ \mu\mathrm{m}$ DLFs, periodic tremors were detected in the polishing system when the outer half of the DLF was used, and the samples were destroyed when polished in this region. Therefore, when using lateral movement of the arm and fine DLFs, the arm was manually lifted up when approaching the bad regions, and put down again when within the good region, as illustrated in Fig 4.1. This increased the quality of the samples drastically, and much less cracking was observed.

Some of the main issues with tripod CS samples are present in the BF image in Fig. 4.2, where a very small area of the film is electron transparent. It is part luck, part experience that determines if one ends up with only one or two sides of the sandwich intact at the film-substrate interfaces. In the case of F1.2, only one side remains as seen in Fig. 4.2a. According to Eberg *et al.* the glue layer should be thinner than 50 nm, and the reason why only one side of the sandwich remains in F1.2 can be attributed to the glue layer being twice as thick as what is recommended. It is uncertain whether the fact that the glue layer

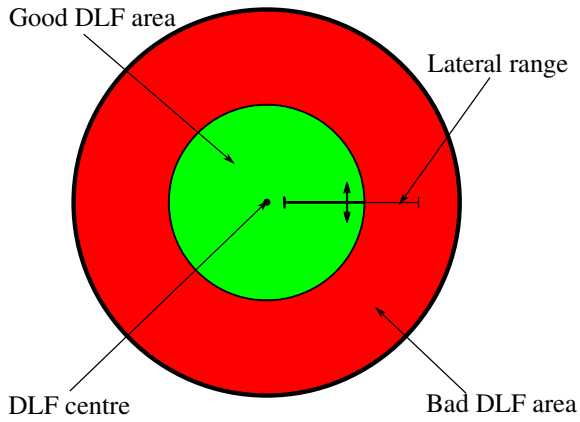

Figure 4.1: Illustration of tripod polishing using a platen and/or DLF of reduced quality at the outer $\sim$ half. The green area is an area that is deemed "safe" for the sample. This must be based on experience and is best detected by keeping a hand on the instrument during polishing to feel for tremors. The red area indicate a risk area where the sample most likely will get damaged when using finer DLFs. A double arrow mark the position where the arm should be raised/lowered.

does not extend all the way to the tip has a positive impact on the sample or not. An eventual glue layer in this region would have provided extra support, especially if the other part of the sandwich was intact. However it could be that some tension could have built up, causing the sample to bend even more. The contrast in the substrate is quite unordered, which can be attributed to bending and surface dislocation effects. In the BF image in Fig. 4.2b a crack or a sudden bend is pointed out. Due to this crack it is troublesome to tilt the sample so that the film is seen edge-on. A tilt of $\approx 10^{\circ}$ was required in the y-direction and about half that in the x-direction was required to get to the $[11\bar{2}]_{STO}$ zone, where all images of this sample are acquired. It required much training and experience with reciprocal space and tilting to be able to orient the sample correctly. These points are what makes FIB CS samples so attractive as such samples does not exhibit these weaknesses.

An important aspect of this sample (F1.2) is that the film has somehow turned amorphous or polycrystalline at the tip (thinner region), as evident by the HRTEM image in Fig. 4.3. As this is not observed in the FIB CS samples it may be assumed that the mechanical strain due to tripod polishing has altered the film structure in the thinnest regions. A suggestion to what causes this change is that the mechanical strain from the tripod DLF provide enough energy for the film in the thinner regions to relax in some way. The fringes observed in this layer can be thickness fringes, indicating that the amorphous layer is increasing in thickness towards the film/substrate. This is not surprising as this part is exposed to the polishing media used because of the lack of glue-layer in this region. Hence it can also be suggested that the glue layer serves to protect the film, and it is possible that if the glue layer had extended all the way to the tip, the film would have been intact.

Further into the tripod sample, i.e. at thicker regions, HRTEM images such as the one pre-

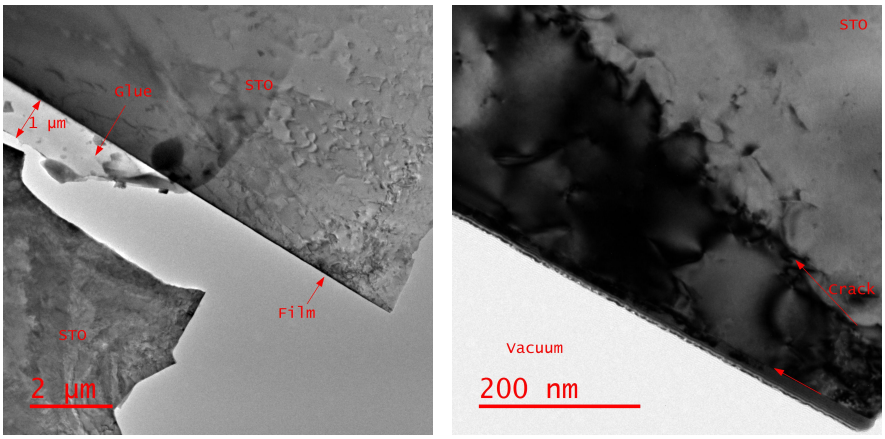

(a) **(b)**

Figure 4.2: Effects of sample preparation on F1.2 shown by TEM images acquired on the 2100F ca one and a half year after the sample was finished. In a) a low-mag TEM image is shown. Only one side of the sandwich remains with its film seemingly intact and electron transparent. The remaining glue layer measures $\approx$ 1 µm. Bending and surface dislocations are most likely the source of the disordered contrast visible in the substrate. The BF TEM image in b) show that at the very edge of the sample the film is amorphous. The unlabelled arrow mark the interface between film and substrate. The other arrow mark a crack, traversing this crack from the substrate towards the film results in a sudden change in crystal orientation.

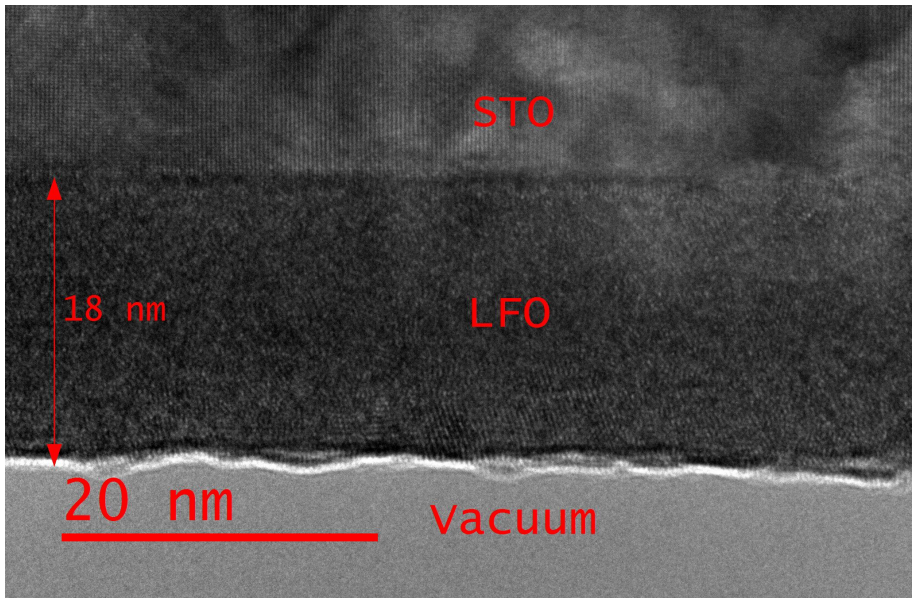

Figure 4.3: HRTEM image of F1.2 acquired from the 2100F, showing the substrate and an amorphous/polycrystalline layer. This image is acquired at the very tip of the edge of the sample, where the BF image in Fig. 4.2b indicated that the film is amorphous. The amorphous/ polycrystalline layer observed here measures $\approx$ 18 nm, corresponding well with the estimated film thickness expected from the film synthesis.

sented in Fig. 4.15a show an amorphous surface layer, which might be explained by the same mechanism suggested above. In this case however, it could be that the sample is thick enough for the inner part of the film to stay crystalline, but the surface layer of ≈ 8 nm becomes amorphous. This may be because the total strain energy of the film increases with the thickness (the presence of a critical thickness for these films show this [19]), and when exposed to a certain amount of stress the film can reduce its total strain energy by relaxing its surface. The film structure closer to the film however, would require more energy and hence it would keep its crystalline structure adopted from the substrate. Of course this is subject to some debate because it does not seem very reasonable that the energy supplied by the tripod polishing is coincidentally just enough to alter just some parts but not the whole film. Also it seems more reasonable that the film should turn polycrystalline with its bulk lattice parameters rather than amorphous. Due to the lack of other explanations however, the amorphous/polycrystalline surface of F1.2 is attributed to sample preparation.

Even if the preparation of PV samples by tripod had a high yield, several problems with these samples were present. Firstly, the bending and surface dislocations introduced additional contrast, making the interpretation of BF/DF images challenging (see Figs. 4.5a, 4.5b and 4.9c). The samples are most bent close to the edge which is the thinnest. However this is not so bad, as the thinnest areas of a tripod PV sample should be considered with some scepticism following the discussion of the amorphous film of sample F1.2, and are therefore rather uninteresting. Scratches due to the tripod preparation is visible as rough lines across the samples. These scratches can be difficult to separate from the step lines however (step lines will be discussed later), and as such the complicated contrast in purely tripod wedged PV samples make them less attractive than FIB improved ones.

4.1.2 FIB

FIB improvement of tripod PV wedges was a great success. The DF series of the tripod edge of F4.3 presented in Fig. 4.9c show extensive bending contrast and scratches which disrupts much of the image. The DF series of a FIB ditch in this same sample (see Figs. 4.9b and 4.11c) show none of these effects, and the contrast mechanisms of interest are much more easily interpreted. The most benefit of this procedure is perhaps best appreciated by STEM and EELS, as such techniques are very sensitive to height differences and surface morphology. FIB preparation of PV samples should therefore have the goal to prepare samples for such advanced techniques, because tripod wedge samples may very well be suitable for low magnification DF imaging.

CS samples prepared by lift-out in the FIB were much easier to work with in the TEM than tripod CS samples. However, the FIB preparation was very time consuming and required much skill and expertise to perform. The recipe developed and used by Magnus Nord was very efficient, and if time had allowed it, samples of much higher quality could have been produced. One of the most challenging aspect of this kind of preparation is to estimate the sample thickness *in situ*. A ”better safe than sorry” policy is advised, as a sample that is a little too thick can be brought back to the FIB for improvement, which is a further advantage over tripod samples. Besides the large flat electron transparent areas provided by

the FIB preparation, the high degree of control of the zone axis provided by this technique was very advantageous because very little tilting in the TEM was required to get samples on desired zones. The bending of tripod CS samples may in principle induce strain, which in turn may alter the properties of the material being studied. This makes FIB CS samples even more attractive.

The danger of exposing the film to the ion beam at high acceleration voltages and turn the crystalline film amorphous is always present when preparing FIB samples. It is only when the finished sample are studied in the TEM that it can be discovered if the film is destroyed or not (see Figs. 6.12b and 6.13 in Appendix D for examples of destroyed samples). The first couple of samples prepared from F4 did not exhibit ion beam damage, but sample F4.6 did. When attempting to improve a FIB CS sample that was ruined due to the tip breaking off (F4.2), the film of this sample became damaged as well. It is thought that the beam damage is mostly due to the changing of the apertures governing the ion current in the FIB, as when the ion beam apertures were changed a strong signal was sometimes detected by the secondary electron detector, indicating stray ions hitting the sample or chamber walls. Hence the sample wafer might have been exposed to stray ions, thus turning the film amorphous, even before the protective layers could be deposited. This might be the reason for several nanometres of film becoming amorphous before depositing local protective layers with the electron beam, the 3 nm of Pt/Pd deposited by the sputter coater before loading the sample in the FIB offering too little protection. Ideally the whole wafer slab should be coated with the C+Pt layers deposited by the electron beam before the ion source was turned on. However depositing these layers is very time consuming and draining on the materials in the FIB. Alternatively one could coat the whole wafer in a $30+$ nm layer of Pt/Pd using the sputter coater, but this is thought to produce grains that will disturb the milling and introduce a "curtaining" effect on the sample (a "wave"-like variation in thickness orthogonal to the film interface). Another option would be to use the sputter coater to deposit C instead of Pt/Pd, but at the time this feature was not working, and could not be tested. To ensure a successful sample new pieces of the sample wafer should be used each time, or one could deposit several protective layers with the electron beam initially.

The risk of destroying the film is the very reason why the protective layers are deposited. As can be appreciated from the STEM and EDS data in Fig. 4.4 the protective layer of C and Pt are sufficient to stop Ga ions from reaching the film when depositing the thicker C layer. There are some lines in the EDS data between 2 and 4 keV that has not been indexed. These lines belong to the e-dep protective layers, and can therefore be a variety of elements that are present in the gases used to deposit these layers. A very weak line at energies about 1.7 keV are present in both the substrate and the e-dep protective layers, and has not been indexed. This line might be due to Si as this element have three K-shell transitions around 1.74 and 1.84 keV. As the saw that cut the sample wafer was of Si composition, the presence of Si is not surprising. Additionally, the FIB is used quite a lot for Si purposes, and the sample wafer is almost sure to have had some contact with other sources of Si as this is a very common element. What is strange is that the line seems to disappear in the film and the Ga C layer. In any regard, the presence of this line is thought not to

influence the results of this thesis.

Another thing that can go wrong when preparing TEM samples by FIB, is the handling of the lift-out piece. As the sample hangs only by the AutoProbe (see Fig. 3.8b) any disturbance in this probe can cause it to vibrate. This vibration may break the Pt welds that hold the sample to the prob,e and send the small piece flying and sucked in by the vacuum system. The same problem arises if the sample is not properly detached from the sample wafer before the probe is moved, as this effectively makes the sample and probe a spring system that can launch the sample through the chamber. These are problems that present themselves about halfway into the preparation session, leaving the operator with the option to start over again. The issues connected to the movement of the probe can not be avoided, and only experience and skill along with a bit of luck can prevent them.

4.2 Step lines

The BF images of the tripod edge in F2.1, presented in Figs. 4.5a, and 4.5b, show some scratches which may be attributed to sample preparation (pointed out by green arrows), but other lines, pointed out by red, blue, and pink arrows, that are too thin and regular (and in unlikely directions $\sim 60^\circ$ to each other) for them to be scratches, are also observed. For clarity, these lines will be referred to as "step lines". The step lines are seen in TEM images of FIB PV samples, presented in Figs. 4.5c, 4.5d, and 4.5e, and can not be due to tripod polishing. First of all the STO surface exposed to the DLFs have been milled away by the FIB in some of these images, and step lines are still present (even unchanged in the case of F4.3 which has undergone two FIB sessions). A rule of thumb with mechanically polished samples is that one should remove ~ 3 times as much material as the grin size used for the polishing in order to fully remove the effects of the polishing. As the FIB ditches in the PV samples are > 0.6 µm deep, the mechanical polishing of these samples cannot be the origin for the step lines, hence they must be due to the substrate or the film. Furthermore, it is highly unlikely that scratches on the film surface would be straight like the step lines observed, and so they must be an effect of the substrate, substrate surface or in the film.

As the substrates have a miscut, and hence induced terraces, the resulting step edges might be the origin of the step lines. In Fig. 4.5a the step lines can be seen to be along $< 1\bar{1}0 >_{STO}$, which is the same as in the DF mosaic of F4.4 in Fig. 4.9a. However, for F4.3 they go in $< 11\bar{2} >_{STO}$, as seen in Fig. 4.9b. According to the growers, the step edges should go along $< 11\bar{2} >_{STO}$, it is therefore surprising that in the same film lines along$< 1\bar{1}0 >_{STO}$ are observed. Whatever the reason for the step lines, they are not observed to affect the domain structure of the film. Comparing the DF image of F4.4 in Fig. 4.9a with the DF image of F4.3 in Fig. 4.9b reveals that the domain structure, and the relative amounts of A, B, and C domains, are not influenced by the step lines. It might seem like the domains are confined by the step lines, but this is not always the case. No domain appears more often around a step edge as another, and the step edges seem to pass right through the different domains. Therefore it is concluded that the step lines are

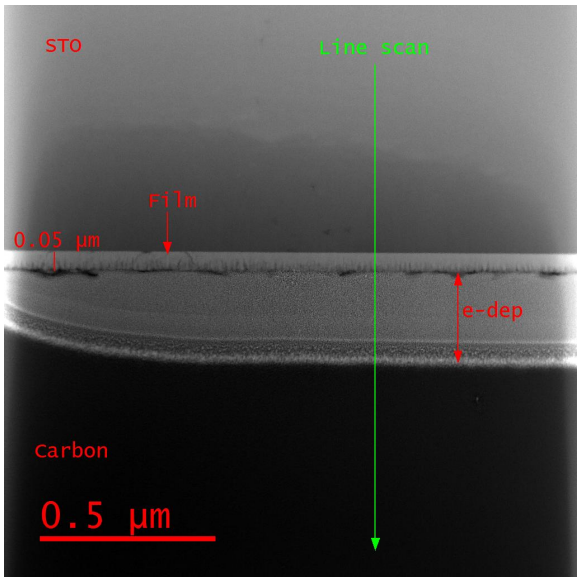

(a)

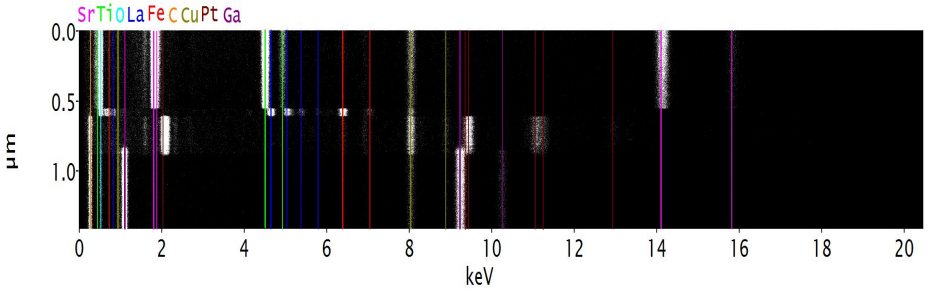

(b)

Figure 4.4: HAADF STEM and EDS analysis across the interface of sample F3.1 acquired on the ARM200F. In a) the HAADF STEM image is presented, showing the line and direction of the EDS scan. Some structure of the film can be seen, and its thickness is ≈ 0.05 µm. The protective layer deposited by the electron beam in the FIB is marked explicitly. EDS data acquired from the scan is presented in b), with the abscissa in keV and the ordinate being the position along the scan. It is indexed using the tables of the X-ray data booklet [63].

artefacts related to the substrate and are not directly relevant to the results and discussions in this thesis.

4.3 Domain structure

In Figs. 4.6 and 4.7 CS DF series of F4.1 and F3.1 are presented. It is clear that there are some major differences in the two series. For F4.1, the DF image using the $\bar{1}0\bar{1}_{LFO}$ reflection reveals domains of relatively homogeneous contrast, while the $(101)_{LFO}$ DF image of F3.1 show very disordered contrast. This is a reflection that, according to the theory chapter, should be present in the film at all times. It is likely that the sample is a little bent, but the contrast changes too abruptly in both images for this to seem plausible and other explanations must be sought. One such explanation is that the structure factor of the film unit cell varies. This might be due to e.g. octahedra rotations and slight cation displacements, and could in theory reduce the intensity of the diffracted beam or make it extinct. It seems reasonable that the thicker and cracked film of F3 will contain more strain and thus more variations in structure factor, both in-plane and out-of-plane, compared to the thinner film of F4. For F4.1 it seems more likely that the difference in contrast are due to bending and thickness variations however, as this film should be rather homogeneous with respect to the structure factor both in-plane and out-of-plane.

The other reflections imaged of F4.1, namely the $(\bar{1}1\bar{1})_{LFO}$ and $(010)_{LFO}$, are specific to C domains. Therefore it is expected that these reflections would reveal domains in the film. Domains imaged by these reflections appear much more sharper than the ones imaged using the $(\bar{1}0\bar{1})_{LFO}$ reflection, which may seem strange when considering the fact that the reflection in the DP (Fig. 4.6a) is much weaker than the $(\bar{1}0\bar{1})_{LFO}$. However the contrast of each image has been enhanced individually, and the relative intensities between these images are therefore irrelevant. The reason why the domains vary in contrast along the substrate is simply due to the fact that this is a CS sample and the volume fraction along the viewing direction may not be constant as illustrated in Fig. 4.8. What is interesting however is that the C domains imaged seem sharp, and their contrast appear to be relatively homogeneous in the out-of-plane direction. There are some domains that does not exhibit a boundary perpendicular to the $(111)_{STO}$ plane, indicating that eventual domain boundaries are not necessarily perpendicular to the film surface.

When it comes to the DF series of F3.1 the most interesting features are observed in the substrate. The contrast in the film is very disordered, and following the discussion of structure factor variations due to strain, the contrast in the film will not be discussed more extensively. Considering the DF images of the $(111)_{STO}$ and $(1\bar{1}0)_{STO}$ reflections shown in Figs 4.7b and 4.7d it seems that the substrate is somehow affected by the thin film in irregularly spaced regions, these regions are marked with teal arrow heads. The sample seem to be a little bent, but the contrast in these regions is too abrupt to be completely attributed to bending and thickness effects. Some of these regions are quite extended along the interface, being $\sim$ 20 nm in length, while others are very small and are $<$ 5 nm in length. Comparing the LFO sensitive DF images and the STO sensitive ones, no connec-

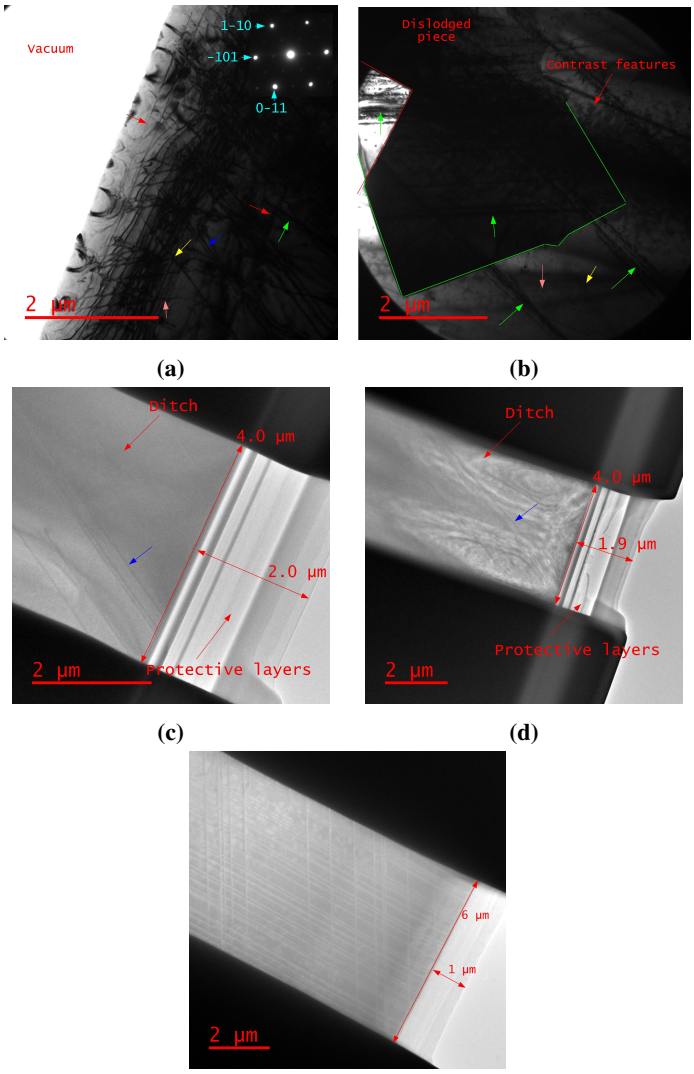

Figure 4.5: TEM images showing the various effects of PV sample preparation. In a) and b) BF images of two different areas along the tripod edge of F2.1 is presented. Rough lines are observed and pointed out by green arrows. Sample preparation seems a probable explanation for these lines. Another set of lines, pointed out by red, blue and pink arrows are much finer and angled an integer multiple of $\sim 60^\circ$ to each other. In b) a dislodged piece is seen and outlined by green lines. A notch in the base sample is outlined by red lines. In c) and d) TEM images of the FIB ditch in sample F4.3 is shown before and after second session respectively. A set of fine lines are pointed out by a blue arrow. These lines has not changed during FIB sessions. Finally in e) a TEM image of the FIB ditch of sample F4.4 is presented, clearly showing two sets of lines angled 60° to each other. The fine lines in all these images are referred to as step lines in the text. All images were acquired on the 2100 microscope, except e) which were acquired in the 2100F.

tion is found, i.e. dark spots at the interface in the STO sensitive images are not bright in the LFO sensitive ones. It might be that these dark spots are effects of step lines going into the image plane, but this is uncertain as it is not known what is causing the step lines.

The only certain result from the DF imaging of CS samples is that orientational domains might be present. Therefore DF imaging of PV samples was conducted. In Fig. 4.9 mosaics of three DF series of the same film are presented (the original DF images are presented in Appendix C). These images serve to prove several important points regarding the domain structure of the film. It should first be mentioned that the various DF series presented in Appendix C (Figs. 6.6 and 6.7) prove that the inner and outer reflections are equivalent in terms of DF imaging, and that they are in agreement with the annotated simulated DP in Fig. 2.11c in the theory chapter. Next it is valuable to note that the domains are observed in the tripod edge of F4.3 as well as the FIB ditches of F4.3 and F4.4, indicating that they are not induced by sample preparation. The shape of the domains is irregular, and their sizes vary from tens to thousands of square nanometres. An equal amount of A, B, and C domains are observed. Sample F4.3 was glued to a grid using a thermal hardening glue, and was heated at elevated temperatures after thinning. In principle this may have altered the structure of the film. Sample F4.4 however was not heated after thinning and because this sample show similar results as to F4.3 one may conclude that heating a thinned tripod wedge at 150° for approximately two hours does not affect the domain structure, except maybe at the very tripod edge where not data have been acquired. It might be interesting to examine how the domains evolve if a sample is heated *in situ* to even higher temperatures, and if this will change the shape/size of the domains. Unfortunately there was no time for this kind of experiment to be designed and performed.

A set of reflections present in the DP of Fig. 4.9d cannot be explained by the assumptions made in the theory section, and some of these are marked with purple circles. Even if one allows for double diffraction between domains and the substrate no reciprocal lattice vector is found for these "purple" reflections. However, as this DP is of the tripod edge which is quite severely bent, LFO and/or STO reciprocal lattice vectors that are not perpendicular to $[111]_{STO}$ may be in Bragg. These additional reflections were not seen for other electron DPs, from tripod edges or FIB ditches, making it seem reasonable that the additional reflections are an artefact only present in this area, and that this is connected to the bending at the tripod edge.

The most striking feature in all DF images is the presence of dark lines within some domains, which will be referred to as internal domain boundaries (IDBs). All of the three domain types show the presence of IDBs, and they appear to be parallel with the in-plane axis of their respective domains. However, some of these IDBs appear to change direction and bend slightly. To discuss this feature Fig. 4.10 is helpful. In this illustration, two equally probable nucleation orientations of an A domain are illustrated. In principle all domains may be rotated by 180° about the out-of-plane axis and still produce the same reflections in a DP, hence they will not be distinguishable by DF imaging. However, if two such domains meet, they will not be compatible with one another as the illustration clearly shows. Planes along the $[\bar{2}11]_{STO}$ direction, which are perpendicular to the $(111)_{STO}$

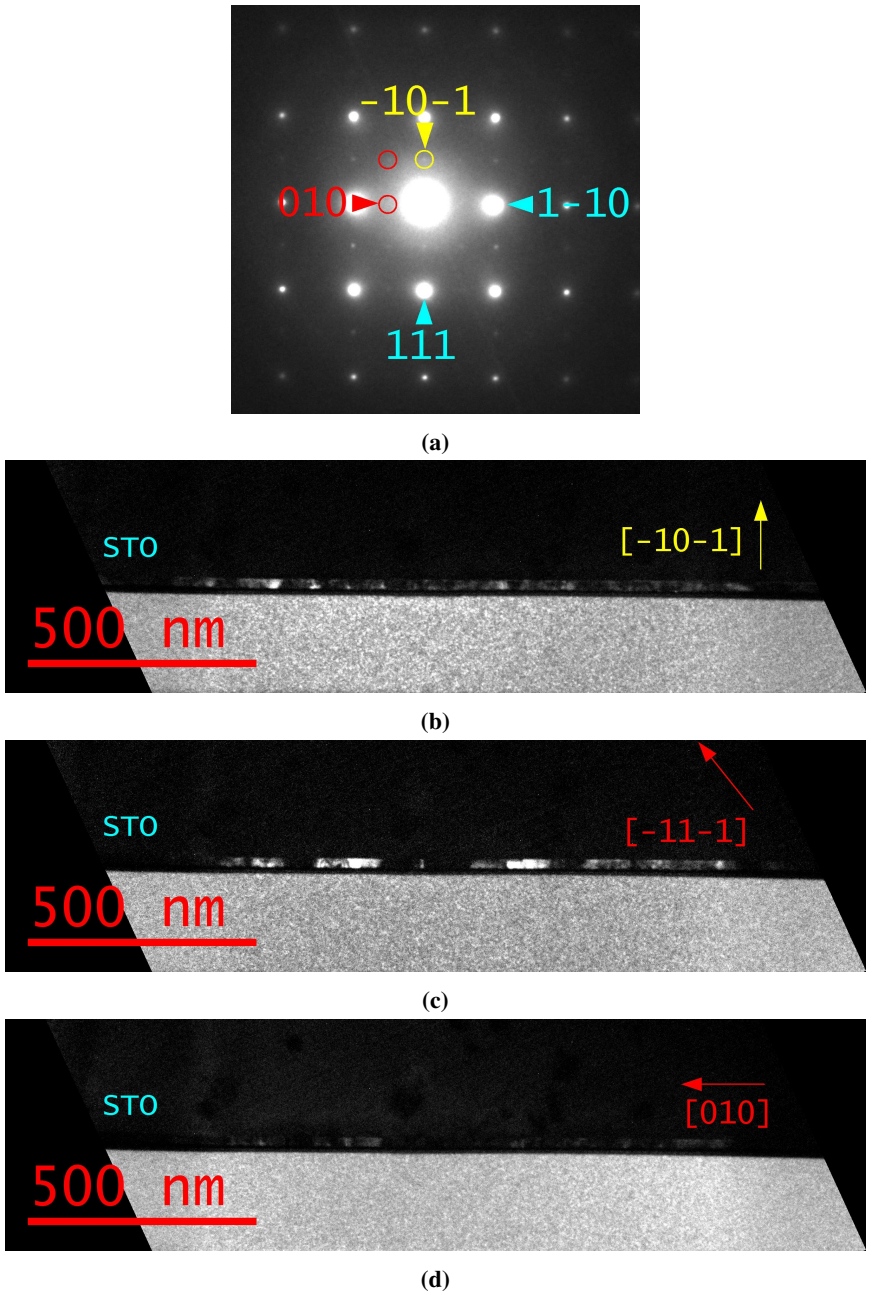

Figure 4.6: TEM DF images of sample F4.1. In a) the electron DP pattern is presented, it is indexed as a $[11\bar{2}]_{STO}$ zone axis with red and yellow arrowheads pointing to $(010)_C$ and $(\bar{1}0\bar{1})_{LFO}$ respectively. The circled reflections has been used for the DF images in b), c) and d) with the direction and (hkl) values of the imaged $\vec{G}$ shown. Acquired on the 2100.

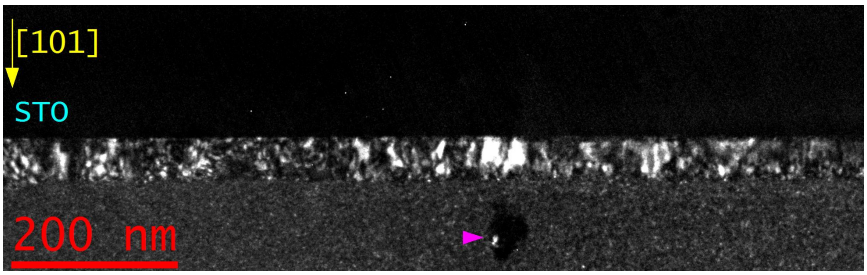

(a)

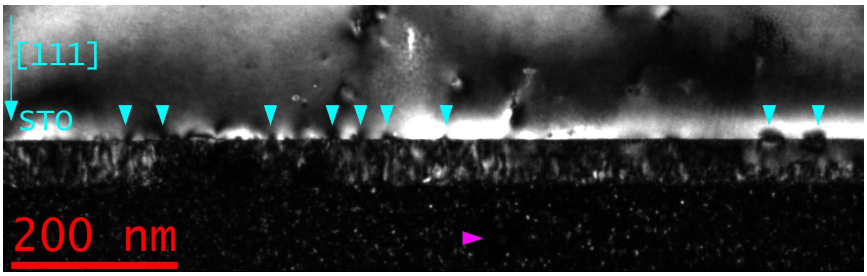

(b)

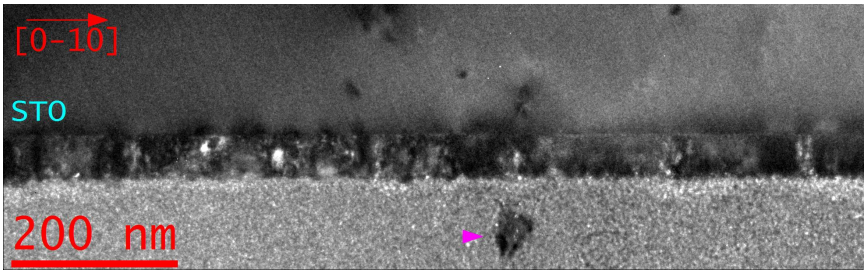

(c)

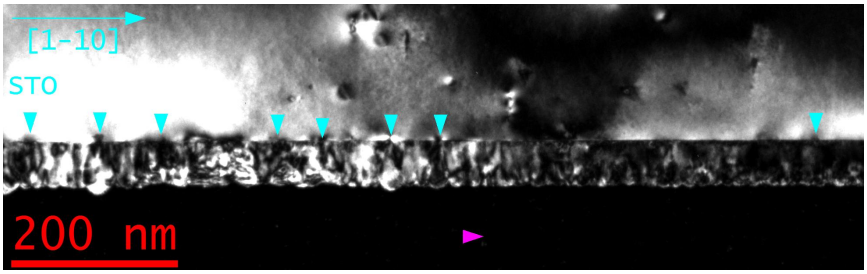

(d)

Figure 4.7: DF images of F3.1 using both LFO reflections a) $(101)_{LFO}$ and c) $(010)_C$ as well as STO/LFO reflections b) $(111)_{STO}$ and d) $(1\bar{1}0)_{STO}$. Substrate is to the left in each image, and the protective layer is to the right. The direction of the $\vec{G}$ imaged is indicated by the arrow in the top left corner of each image along with its hkl values. The lengths of the arrows are not to scale with each other. Purple arrowheads mark the same reference feature in each image. Teal arrowheads mark points of interest in the substrate/film interface region. Acquired on the 2100F.

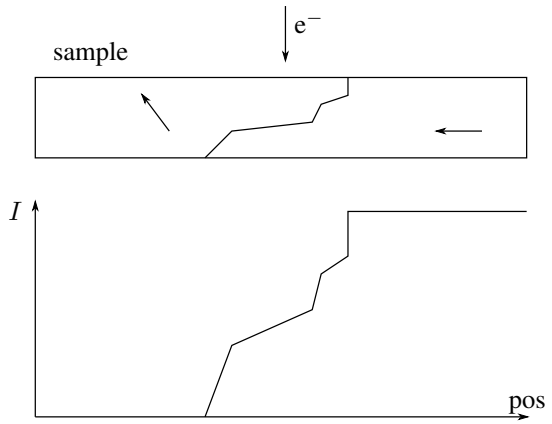

Figure 4.8: Figure suggesting how the intensity of a diffracted beam vary along the interface of a CS sample. The incident beam direction is indicated by the top vector, and can e.g. be $[11\bar{2}]_{STO}$. The film (labelled "sample" in the figure) is seen along a $< 111 >_{STO}$ direction, and has two different orientation, the resulting grain boundary is drawn as an irregular line. To the right the sample satisfies the Laue equation for this incident beam direction, while to the left it does not, the vectors in the two regions signifying the direction of the in-plane orthorhombic axis. Below the sample an illustrative plot of the intensity in the e.g. $(010)_{LFO}$ diffracted beam is drawn, showing a gradual decrease due to the different volume fractions satisfying the Laue conditions.

plane, are in this figure labelled "A", "B", and "C" (not to be confused with domains with similar symbols in italic or the usual stacking notation of planes along the $[111]_{pc}$ direction). The stacking sequence along this direction is "ABCABC" in one grain and "CBACBA" in the other. In the boundary between the two grains however, the stacking is "CABAC" which is not a coherent boundary. This boundary will therefore introduce an increased amount of strain, which in turn may cause the local region of the boundary to not scatter to the usual A domain reflections. As the only real requirement for these boundaries is that they must be parallel to the in-plane axis, the boundary need not be perpendicular to the film surface. According to this figure a similar boundary may appear perpendicular to the in-plane axis direction, however this illustration has assumed the LFO unit cells to exhibit perfect six fold symmetry around the $[111]_{STO}$ axis. The LFO domains exhibit a twofold rotation symmetry about this axis however, which is the reason why these twin boundaries can only be along the direction of the in-plane axis. It is therefore very probable that the IDBs are perpendicular (at least very close to being so) to the film surface normal, and that they are due to strain caused by the two adjacent domains of the same type, but with their in-plane component of the $\vec{c}$ axis in opposite directions.

Interesting contrast is observed in the HAADF STEM images of sample F4.3 presented in Figs. 4.11a and 4.11b. These two images were acquired with two different camera lengths, and are opposites to one another in the way that bright areas in one are dark in the other, and *visa versa*. To make comparisons easier, a mosaic of the images is presented in Fig. 4.11c, where the STEM image in a) have been coloured red and the one in b) have been

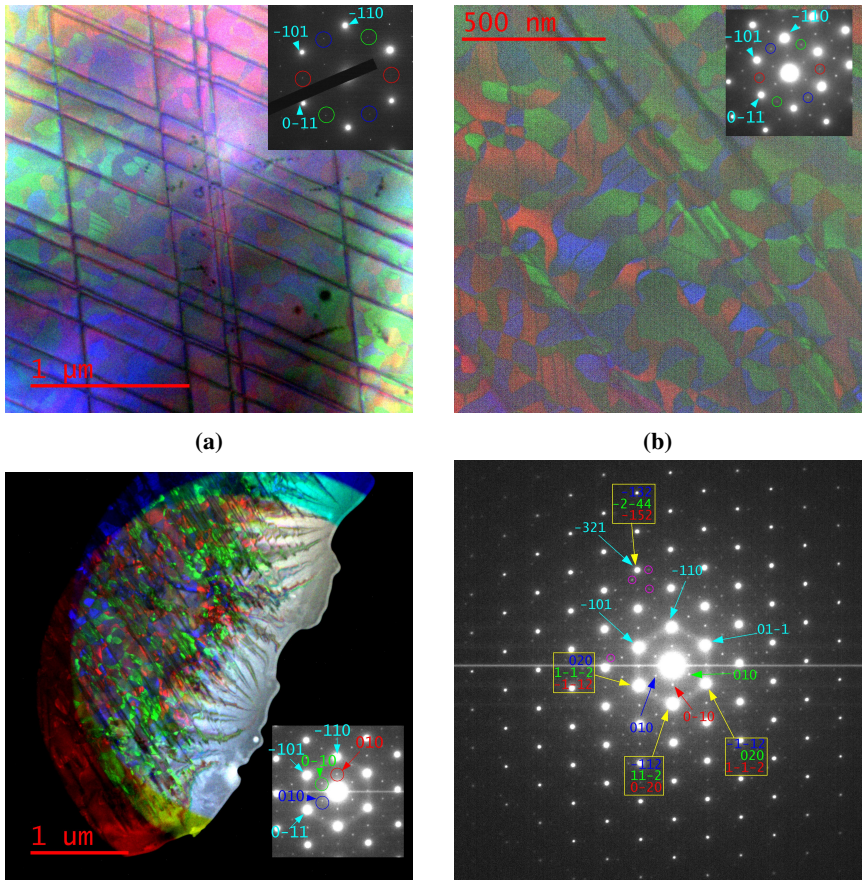

(a) **(b)**

(c) **(d)**

Figure 4.9: DF mosaics of different samples and areas. In a) a mosaic of DF images of sample F4.4 is presented (originals in where the step lines are not seen to affect the different domains differently. A similar mosaic is presented in b), this being based on a DF series on the FIB ditch of F4.3. In c) a DF mosaic of a series acquired of the tripod edge of F4.3 is presented. The DP inset in c) is shown in a larger format in d), as there are some interesting reflections to be seen. The indexing of this DP is transferable to the DPs in the insets. See Appendix C, Figs. 6.5, 6.6, and 6.9 for the DF series used in a), b), and c) respectively. a) has been acquired on the 2100F, the others on the 2100.

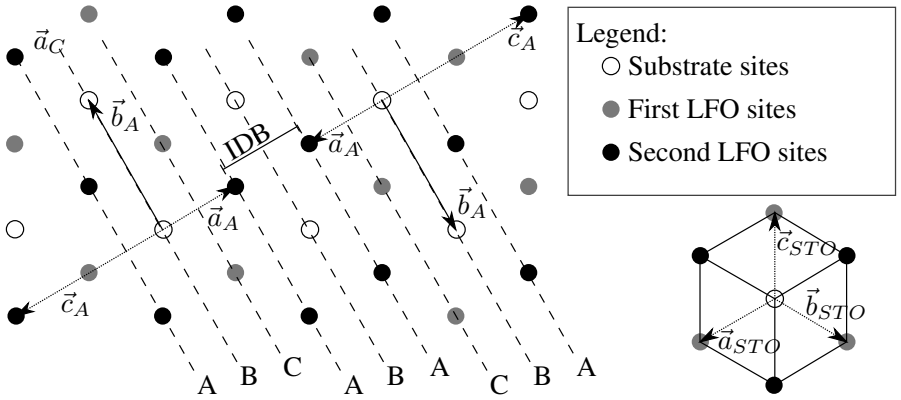

Figure 4.10: Illustration of LFO growth on (111) oriented STO by assuming $a_{LFO} = b_{LFO} = \sqrt{2}\,a_{STO}$ and $c_{LFO} = 2a_{STO}$. Circles mark the sites of the STO surface, the lighter dots mark the first layer of LFO sites, while the dense dark dots mark the second layer of LFO sites. Dotted vectors refer to vectors with a positive angle to the paper plane (angled out of the paper plane), dashed lines refer to stacking layers along the $[\bar{2}11]_{STO}$ direction.

coloured green. Comparing this mosaic to the mosaic of a DF series of the same sample presented in Fig. 4.11d, reveals that the features seen in the STEM images are connected to domains. However the connection is not straightforward, which is evident by comparing the areas circled by the green and red circle in both mosaics. The C domain circled by the green ring appear red in the STEM mosaic, however the C domain in the right part of the red circle appear green in the STEM mosaics. This inconsistency can be explained by the combination of the two fold symmetry of the domains and eventual misalignment of the annular detector. Figure 4.12 illustrates the principle. A misalignment of the detector and the CBED centre may cause more diffracted/scattered electrons of one domain to hit the detector than other domains. It is a common issue when doing STEM (at least with *JEOL* microscopes) that the diffraction centre changes as a function of probe position, when doing STEM over large areas. Therefore, one may suspect that a domain being "favoured" in one region of the image is disfavoured in the other. Additionally the CBED centre may change when changing camera lengths, hence the two STEM images are opposites. Additionally, the sample is probably slightly bent, and as STEM has very short depth of focus, the difference in sharpness in the different parts of the image may be attributed to sample bending. This result is not directly relevant to the present work, but it is an important and possibly useful result for future work, as it provides yet another way to observe possible orientational domains.

The HR STEM HAADF image of the FIB ditch in F4.3, presented in Fig 4.13a, show atomic columns in what appears to be a six-fold network. The FFT spectrum of this image, which is presented in Fig. 4.13b, reveal that the total symmetry is not perfectly six-fold. It appears that two domains have a different lattice parameter (the other lies within the noise lines and it is not possible to consider the exact position of this component). This is very

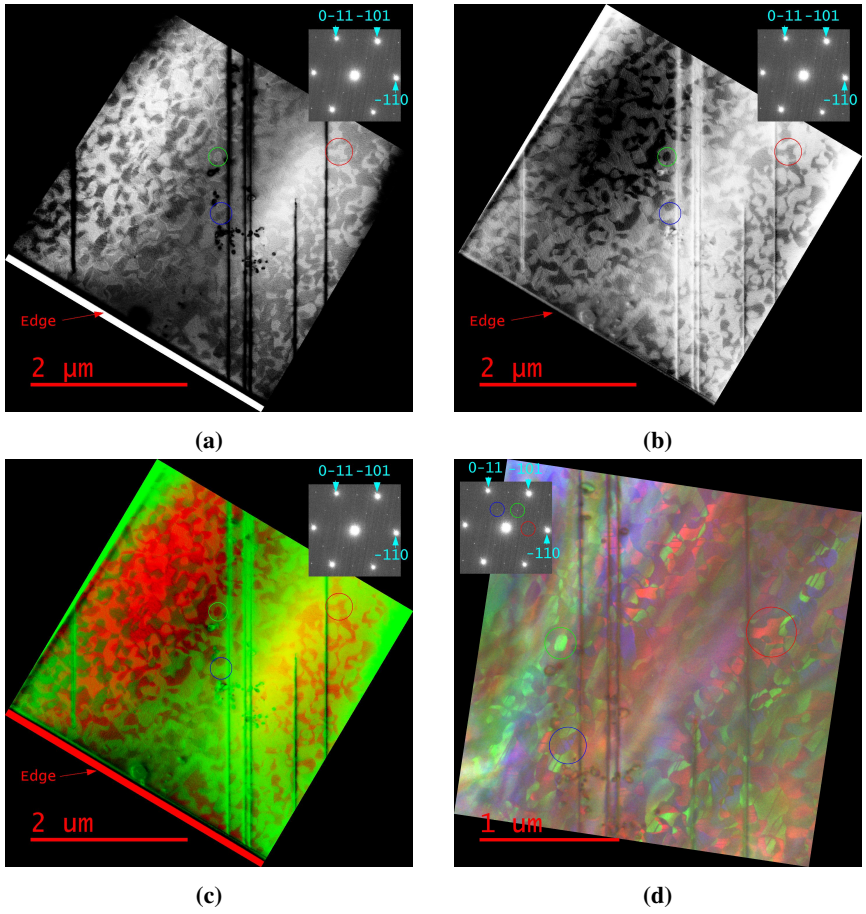

Figure 4.11: Comparison of STEM and DF results from the FIB ditch in F4.3. In a) and b) HAADF STEM images with (uncalibrated) camera lengths 150 mm and 120 mm respectively are shown. In c) a mosaic where a) is coloured green and b) has been coloured red. A mosaic of a DF series (presented in Fig. 6.8 in Appendix C) of the same area is presented in d) allowing comparisons between STEM and DF contrast. The blue, green, and red circles in the real space images refer to easily identifiable A, B, and C domains respectively. The C domain circled by the green ring appear red in the STEM mosaic, while the C domain in the right part of the red circled area appear green, the contrast connection is thus not direct. Acquired on the 2100F.

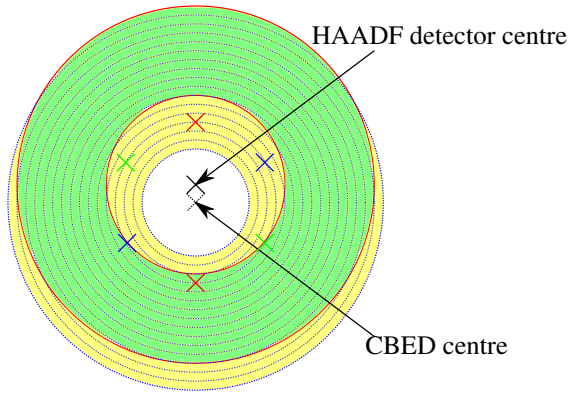

Figure 4.12: Illustration of HAADF detector misalignment. The edges of the HAADF detector are represented as red rings, only the reflections inside the green area are detected. The CBED pattern is illustrated as concentric, blue, dashed lines. The HAADF detector and CBED centre are marked by a solid and a dashed cross respectively. The reflections in the yellow areas are not detected. The twofold symmetry of the different LFO domain diffraction patterns is indicated by the crosses in blue, green, and red. The misalignment of the HAADF detector may cause some reflections to be favoured more than others, thus making the contrast sensitive to different domains.

interesting as it could mean that one of the domains have the longer $\vec{b}$ axis as its in-plane axis, while the other have the shorter $\vec{a}$ axis in-plane, thus making the spatial frequencies slightly different. A more likely reason however is that the sample was drifting during the very large scan, possibly making the lattice parameter closest to the drift direction seem different from the others. By using the inner frequency components in the three different directions to FFT filter the original image, the images in Figs. 4.13c, 4.13d, and 4.13e were achieved. These filtered images reveal that the STEM image is able to pick up the orthorhombic structure of the film, and show that high resolution imaging of the domains, and even IDBs, are possible using STEM. The fact that STEM is able to image domains mean that atomic resolution EELS analysis of e.g. oxygen vacancies can be performed over specific points of interest, such as IDBs and domain boundaries. The TEM samples studied in this thesis were too thick for such techniques however. HRTEM of PV samples revealed domains as well, but as no additional useful information could be gleaned from these, they are not presented.

How the presence of orientational domains affects the functional properties of LFO is uncertain. Czekaj *et al.* show that the AFM easy-axis is determined by the crystallographic domain structure, and so eventual AFM easy-axes of the three different domains will have in-plane components that are angled 60° to one another, unless the easy axis is out-of-plane [67]. According to Seo *et al.*, smaller AFM domains in LFO results in enhanced exchange bias, and it would be interesting to examine how this relates to the threefold orientational domains in the LFO thin films studied in the present work. Folven *et al.* have shown that it is possible to engineer stabilized AFM domains along the edges of embed-

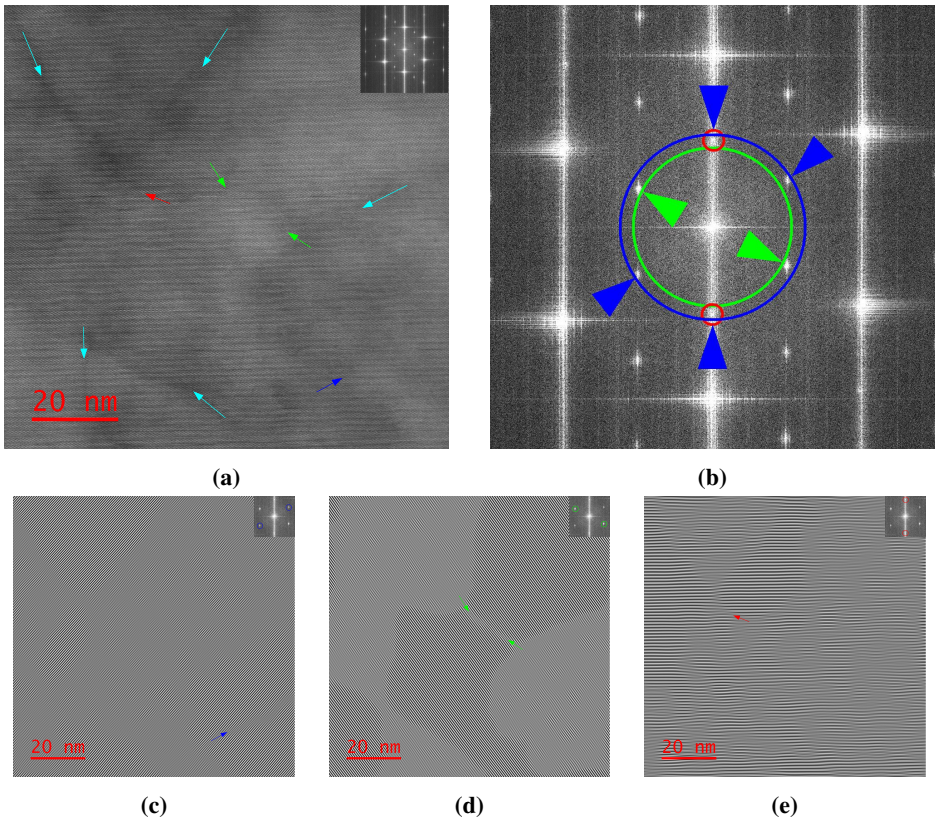

Figure 4.13: High resolution STEM image and FFT analysis showing orientational domains. In a) a (4096×4096) pixel STEM HAADF image aquired on the ARM is presented. The teal arrows mark where the FFT filtered images indicate that domain boundaries exist, while the other arrows mark IDBs of various domains. The centre of the FFT spectrum of a) is presented in b), showing that the spatial frequency in at least two different directions are not the same. FFT filtered images are presented in c), d), and e) where the frequency used is marked in the inset FFT spectra.

ded nanostructures, and that this relies on the direction of the AFM easy-axis [17, 18]. If LFO/STO(111) exhibit AFM easy axes in different directions with respect to each other, embedding of nanostructures in such films may give options to engineer even more complex and detailed devices. However this would require control of the sizes, and possibly the shapes, of the orientational domains.

Lyubutin *et al.* hypothesized that the Neél temperature of LFO drops when the Fe-O-Fe bonds straightens, i.e. when the octahedra tilts of the system is altered [41]. In thin films of LFO on LAO (001) substrates, Grepstad *et al.* observed a drop in Neél temperature to 645 K, and by relaxing the films through annealing in oxygen-rich environments, a further drop to 610 K was observed [56]. If the boundaries between the domains seen in the present work strains the LFO unit cell, which seems likely, it could be that the Neél temperature in these regions is quite different from that of the domain interior. How this will affect the functional properties of the film itself is difficult to predict without knowing the structure of these boundaries. Further TEM experiments, as well as simulations (such as Density Functional Theory (DFT) calculations), may shed some light on the boundary structure, and hence the AFM properties in these regions.

An important question to ask is how the domains in these LFO thin films affect the functional properties of other materials and heterostructures. One of the most important and used tool for tailoring the properties of oxide heterostructures is by strain and strain engineering [51, 52, 62, 68]. If multilayer structures involving LFO thin films on three- or six-fold symmetries can be achieved, it is possible that a threefold symmetry in the nearby oxide layers will appear. For example, if a LSMO/LFO/STO (111) multilayer structure is engineered, would the domain structure of LFO prevail? And if so, would this domain structure induce a threefold strain field in-plane at the LSMO/LFO interface, and thus affect e.g. the oxygen valence of LSMO in any way? Of course the same questions can be asked for any other oxide than LSMO as well. Therefore it may be that the domains observed in the LFO thin films studied in this thesis offer new ways to tailor properties of oxide multilayers by strain. However, it must be emphasized that this discussion is highly speculative, and that further investigations is required.

4.4 Film structure and quality

By the HRTEM image of sample F3.1 in Fig. 4.14 it is obvious that the film is crystalline, and measures about 55 nm. All the film visible in this image is of the same structure, which is evident by the FFT insets. In the out-of-plane direction, the lowest spatial frequency in the film is $d_{hkl}^{LFO} \approx 2d_{111}^{STO} = 4.509$ Å. Only $d_{101}^{LFO} = 4.538$ Å and $d_{011}^{LFO} = 4.542$ Å are viable choices for this d-spacing when assuming bulk LFO structure, these having mismatches of 0.6% and 0.7%, respectively. The lowest spatial frequency in-plane is due to planes with $d_{hkl}^{LFO} \approx 2d_{1\bar{1}0}^{STO} = 5.523$ Å. Viable planes for such frequencies are $d_{100}^{LFO} = 5.556$ Å and $d_{010}^{LFO} = 5.565$ Å, with mismatches 0.6% and 0.8%, respectively. Since $d_{100}^{LFO}/d_{1\bar{1}0}^{LFO}$ has lowest mismatch, it is most likely that the $\vec{a}$ axis lies in-plane, and hence the normal to d_{011}^{LFO} will align with the out-of-plane direction. This is in exact

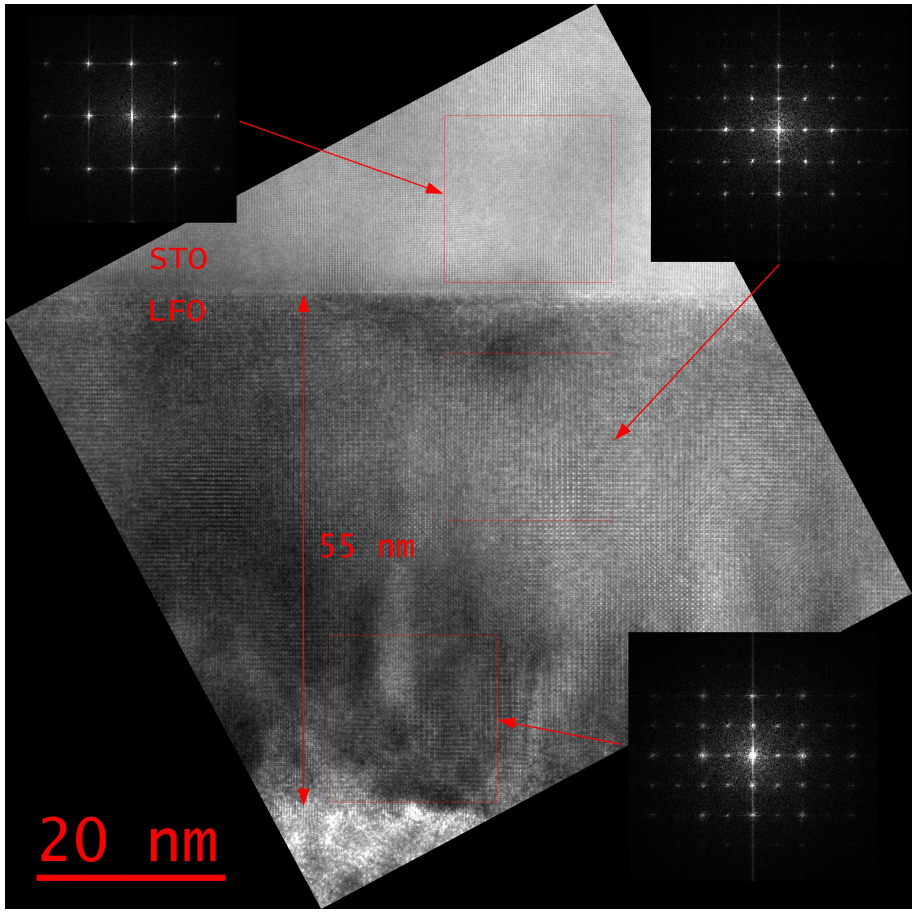

Figure 4.14: HRTEM study of F3.1. The image reveals that the F3 film thickness is ≈ 55 nm. FFT spectra of the squares in the substrate and in the film are shown as insets. The structure of the film is the same throughout the film seen in this image. Acquired on the 2100F.

agreement with the DF results and the theory section.

What is interesting about the HRTEM image of F3.1 is that the surface of this sample should be very rough and cracked, according to the STEM HAADF image in Fig. 4.4. Films thicker than 30 nm exhibit more $3\mathbb{D}$ surface atomic force microscopy data, and this film is no exception judging by the atomic force microscopy data in Appendix A [19, 20]. The crystallinity and the homogeneous structure evident in the HRTEM image may therefore be an indication of the robustness of the film structure.

In Fig. 4.15 a HRTEM study of sample F1.2 is presented. As mentioned earlier this image show that the top ~ 8 nm of film have turned amorphous. It is clear from the FFT spectra that the film structure is different from the substrate. Furthermore it is clear that a domain

boundary is present, as the FFT spectra of two different regions of the film are different. To the right a C domain is present, which exhibits the same spatial frequencies as the film in F3.1. An A or B domain (or a combination) is seen to the left of the C domain. In the A/B domain the spatial frequency along the in-plane direction is the same as for $[1\bar{1}0]_{STO}$, meaning that $d_{hkl}^{LFO} = d_{1\bar{1}0}^{STO} = 2.761$ Å in this region. A likely match for this d spacing, assuming bulk LFO parameters, is $d_{11\bar{2}}^{LFO} = 2.780$ Å, as this has a mismatch of 0.7%. The resulting domain boundary forms a kind of triple point (a triple "line" really) with the substrate. As the profile plot in Fig 4.15b indicates, this triple point seems to induce a distortion of the substrate in the out-of-plane direction. The profile plot show that the repeating contrast pattern in the $[111]_{STO}$ direction becomes that of two peaks, one high and one low. This can be explained by the contrast mechanisms of HRTEM, as different reciprocal distances in the sample (i.e. spatial frequencies) will receive different HRTEM contrast due to the oscillatory property of the objective system transfer function. Within the error margins estimated from the pixel width of the profile plot, the periodicity in the disturbed regions in Fig. 4.15a is half that of the bulk substrate. It should however be mentioned that such profile analysis should be subject to some scepticism as the difference in chemistry and structure at interfaces may play some tricks on HRTEM contrast.

The same out-of-plane elongation of the STO unit cell around triple points is found in the HRTEM image of F4.1 presented in Fig. 4.16. In this image it can be seen that the film is 22 nm thick and crystalline. More importantly, a domain boundary is present. Sadly the HRTEM image is not good enough in order for an advanced analysis of the boundary itself, but by applying FFTs and profile plots some interesting information may be gleaned. First of all, the profile plot of the interface region presented in Fig. 4.16b, exhibits much of the same attributes as the one found for F1.2, such as the change in relative intensity between two adjacent peaks of the substrate close to the interface. Secondly, the FFT spectra of the substrate close to the interface, which is inset in the figure, reveal a frequency component in the out-of-plane direction. A corresponding FFT spectra of the substrate some distance away reveal no such component. This is a very strong indication that a real distortion of the substrate is taking place in the vicinity of the domain boundary. From this it seems very likely that the triple points between domain boundaries and substrate induces out-of-plane strain in the substrate.

By inspection it seems like the substrate distortion is slightly present at the point where the thickness label terminates, and is increasing in substrate-depth towards the domain boundary. Assuming the distortion is highest at the domain boundary it would seem that the total range of the distortion is ~ 20 nm, this is a very inaccurate measurement and it should only be taken as a rough estimate. Nevertheless, this width matches the maximum length of the dark regions in the DF images of F3.1, but as this is not the same sample, or indeed the same film, this observation should not receive too much attention either. The distortion reaches only about $5-7$ regular STO unit cells into the substrate. It is therefore not surprising that this distortion is not detectable in the DF imaging of this sample.

When the STO unit cell becomes distorted, its unit cell will lose some symmetries. LFO increases its symmetry towards cubic through the rhombohedral group $R\bar{3}c$, and as such

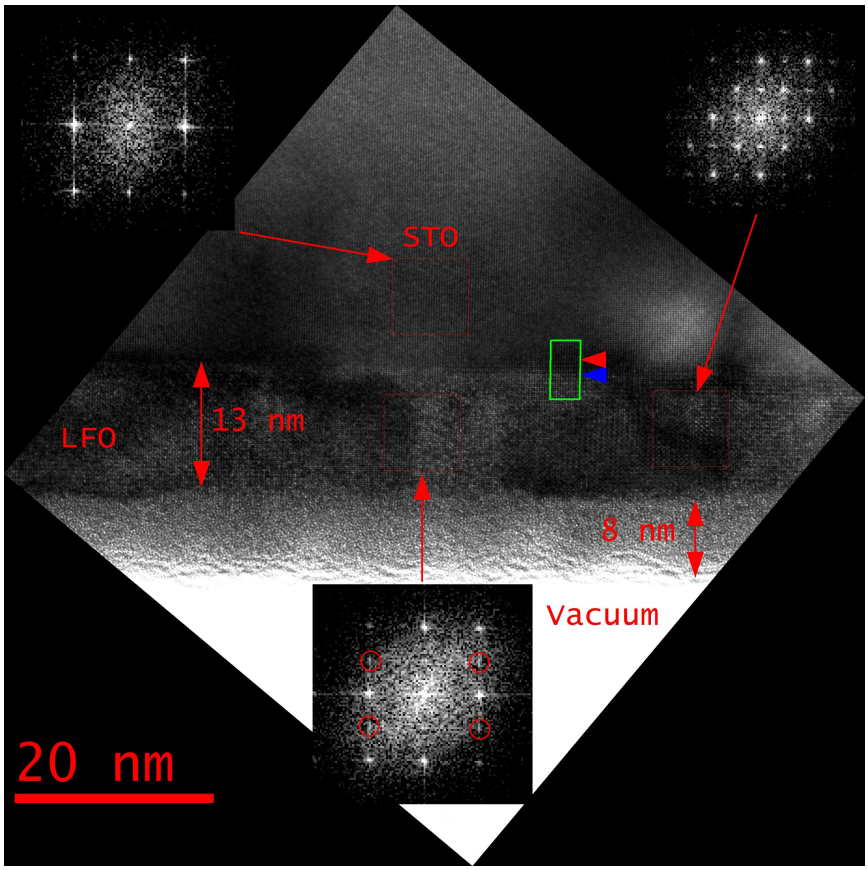

(a)

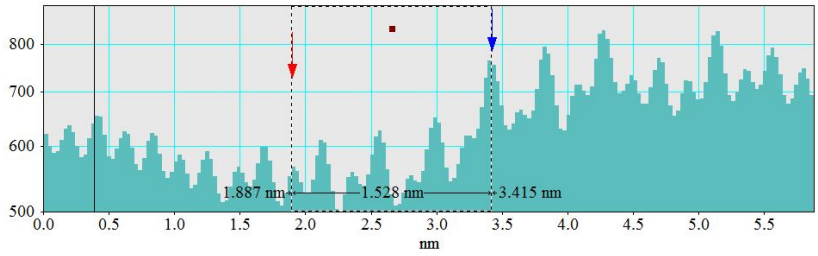

(b)

Figure 4.15: HRTEM study conducted on the ARM of the film thickness and quality of F1.2. In a) two layers are observed, where one is thought to be the crystalline film with a thickness of $\approx$ 13 nm and the other is an amorphous layer with thickness $\approx$ 8 nm. The logarithmic profile plot in b) show the intensity profile of the red rectangle along the $[111]_{STO}$ direction. Blue and red arrowheads mark the interface and the start of substrate disturbance respectively, forming an $\approx 1.53 \pm 0.06$ nm long region close to the interface. Inset FFT spectra in the HRTEM image indicate that a domain boundary is present, and that the substrate is strained in close to the resulting triple point.

one may hypothesize that the distorted structure of the STO substrate close to triple points, belong to a rhombohedral group. Even though this is a very simple and superficial argument, it is compatible with the FFT spectra, as rhombohedral structures, such as LAO, would give rise to a super reflection halfway between the $(111)_{STO}$ reflection if its pseudo cubic cell had the same lattice parameters as STO [69]. However, a monoclinic structure may also be possible. Further research and studies are required in order to determine the distorted structure.

Other perovskite heterostructures, such as the ones studied by Gazquez *et al.* and Nord *et al.*, have shown that the substrate may couple into certain epitaxial films [62, 68]. In these works, an out-of-plane elongation of the film unit cell is found, and is thought to be connected with oxygen vacancies and their ordering. It is therefore not unlikely that in certain systems, the film may couple to the substrate and distort it. In the case of STO, which normally is an insulator at room temperature, strain has been found to induce conductivity and ferroelectricity [52]. It may therefore be speculated that the domain boundaries in LFO creates a network of conductivity "channels" in the substrate, which may have future applications in devices. This is of course highly hypothetical, and further research is required to investigate the properties of triple points.

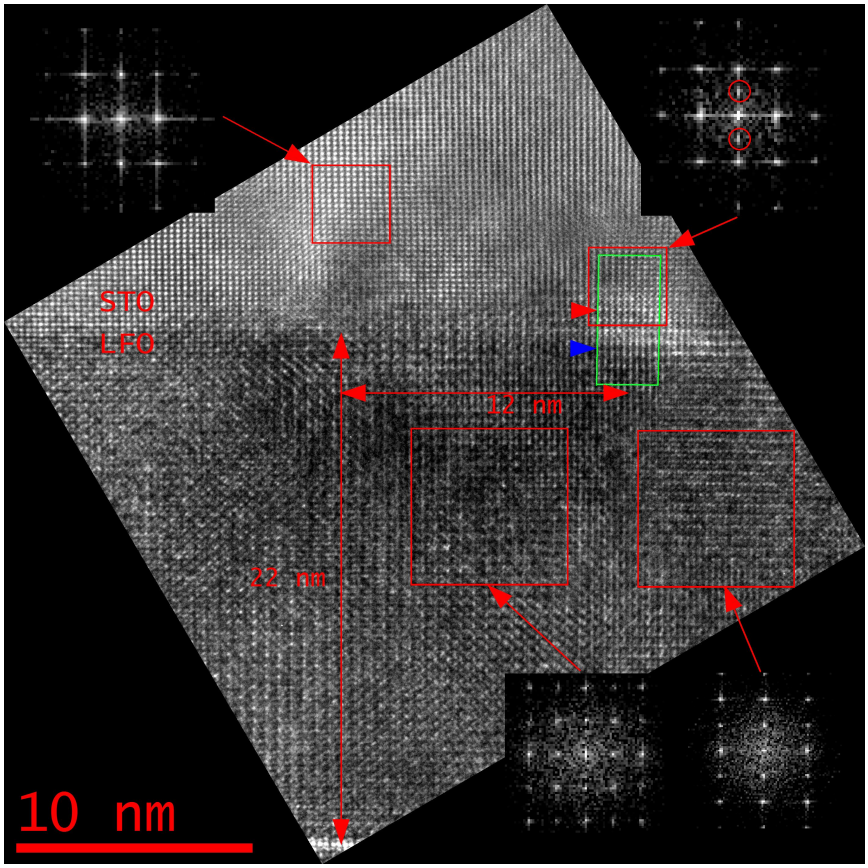

(a)

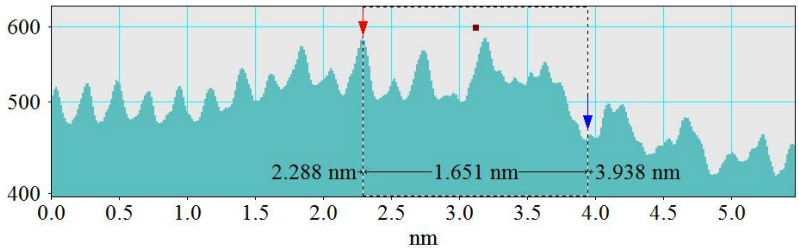

(b)

Figure 4.16: HRTEM study of interface disturbance in F4.1. In a) a HRTEM image aquired from the 2100F show the LFO/STO interface. The logarithmic profile of the green rectangle across the interface is presented in b). Blue and red arrow heads are reference markers to help connect the two images, with the red arrow pointing to what seems to be the beginning of the disturbed region and the blue arrow marking the interface. The disturbed region measures $\approx 1.65 \pm 0.06$ nm in length. FFT spectra of various regions are shown as insets. The disturbed region exhibits a doubling in the $[111]_{STO}$ direction, and it seems like this region is seeded by a domain boundary, evident by the FFT spectra of the film.

Chapter 5

Conclusion

5.1 Sample preparation

Tripod PV samples are viable for the study of domain structures in LFO/STO (111) as they allow for a fast, efficient and cheap way of investigating orientational domains in this material system. Tripod CS samples are achievable by following Monsens [7] and Ebergs [65] previous work. It is advised that the wedge angle for both PV samples and CS samples is set to $4°$. It is suspected that tripod polishing render the film amorphous in thin regions of the sample. This mechanism is attributed to mechanical stress from the polishing providing the film with enough energy to relax.

FIB preparation of CS samples is highly effective and yields good samples. When preparing samples with this kind of instrument, great care should be taken initially, and several areas should be prepared with electron deposited protection layers before the ion source is turned on to avoid ion beam damage to the film. Improving PV samples by FIB is strongly advised for the LFO/STO (111) system as this provides large electron transparent areas with only slight bending, making DF imaging relatively straightforward.

5.2 Film quality and domain structure

The thickness's of the films p30804 (F1), p40207 (F2), p40903 (F3), and p41204 (F4) were measured to be $13 - 21$ nm, 55 nm, and 22 nm, respectively. FFT analysis and DPs indicate that the structure of the film is orthorhombic with one axis in-plane and the other two having components both in and out-of-plane. In turn this causes the film to form orientational domains, having in-plane axes angled $\pm 60°$ to each other. These domains are of irregular shapes and vary from tens to thousands of square nanometres in area. Furthermore, internal strain boundaries parallel to the in-plane axis within domains are observed, and are credited to the in-plane components of the long $\vec{c}$ axis of two adjacent domains

being antiparallel. Because of the three orientational domains, it is thought that the AFM easy-axis of different domains in LFO/STO (111) thin films will either be out-of-plane, or have in-plane components angled 60° to each other.

It is found that slight misalignments of the HAADF detector in STEM may enable low-mag imaging of the observed domains. Additionally, the orientational domains are observable in high resolution HAADF STEM, possibly allowing advanced EELS analysis of domain boundaries, if thin enough samples can be produced.

Long straight lines following crystallographic directions are observed, and are thought to be due to substrate surface preparation, or some other aspect of the substrate. The orientational domains of the thin film seem to be unaffected by these lines.

The film is found to locally distort the substrate, causing an out-of-plane elongation of the STO unit cell. This is attributed to the increased strain field in triple points between two (or more) domains and the substrate. Such film-substrate coupling might be of interest in future applications.

Chapter 6

Further work

For further work, it is recommended to study boundaries between orientational domains, using EELS, in order to elucidate the orbital structure in these areas. Such investigations should also be made of the internal domain boundaries and triple points. High resolution STEM and EELS should be applied to study the film-substrate coupling in more detail, and the structure of the distorted STO unit cell should be determined. Experiments should be designed with the purpose of examining eventual functional properties in such triple points.

An examination of how film thickness affects the domain structure should also be done, and how this domain structure affects multilayer structures with the same surface symmetry as STO (111). Studying the evolution of the domain configuration as a function of temperature may also be of interest, and *in situ* heating experiments in a TEM are recommended.

The domain structure should be seen in context with AFM domains measured by PEEM. Special attention should be paid to the study of the magnetic properties in proximity to domain boundaries, as it is possible that uncompensated spins, or eventual strain between domains, can affect the magnetic properties of LFO.

Preparing TEM samples of STO substrates only, in order to examine if the step lines are present before and after growth might be a good idea.

Bibliography

[1] E. J. Baran. Structural chemistry and physicochemical properties of perovskite-like materials. *Catalysis Today*, 8:133–151, 1990.

[2] A. Y. Borisevich, H. J. Chang, M. Huijben, M. P. Oxley, S. Okamoto, M. K. Niranjan, J. D. Burton, E. Y. Tsymbal, Y. H. Chu, P. Yu, R. Ramesh, S. V. Kalinin, and S. J. Pennycook. Suppression of octahedral tilts and associated changes in electronic properties at epitaxial oxide heterostructure interfaces. *Phys. Rev. Lett.*, 105:087204, Aug 2010. doi: 10.1103/PhysRevLett.105.087204.

[3] K. Dziatkowski, Z. Ge, X. Liu, J. K. Furdyna, and A. Twardowski. Asymmetric magnetization reversal in the exchange-biased mno/(ga,mn)as heterostructure studied by ferromagnetic resonance. *Acta Physica Polonica A*, 110:319, 2006.

[4] Y-M. Kim, A. Kumar, A. Hatt, A. N. Morozovska, A. Tselev, M. D. Biegalski, I. Ivanov, E. A. Eliseev, S. J. Pennycook, J. M. Rondinelli, S.V. Kalinin, and A. Y. Borisevich. Interplay of octahedral tilts and polar order in bifeo3 films. *Advanced Materials*, 25(17):2497–2504, 2013. ISSN 1521-4095. doi: 10.1002/adma.201204584.

[5] N. Nakagawa, H. Y. Hwang, and D. A. Muller. Why some interfaces cannot be sharp. *Nature Materials*, 5(3):204–209, 2006. doi: 10.1038/nmat1569.

[6] M. Mochizuki and M. Imada. G-type antiferromagnetism and orbital ordering due to the crystal field from the rare-earth ions induced by the gdfeo$_3$-type distortion in rtio$_3$ where r = la, pr, nd and sm(condensed matter : Electronic structure, electrical, magnetic and optical properties). *Journal of the Physical Society of Japan*, 73(7):1833–1850, jul 2004. ISSN 00319015. doi: 10.1143/JPSJ.73.1833. URL `http://ci.nii.ac.jp/naid/110001954901/en/`.

[7] Å. Monsen. TEM Characterization of $LaFeO_3$ thin films. Master's thesis, Norwegian University of Science and Technology, June 2006.

[8] J. W. Seo, E. E. Fullerton, F. Nolting, A. Scholl, J. Fompeyrine, and J.-P. Locquet. Antiferromagnetic $LaFeO_3$ thin films and their effect on exchange bias. *Journal of Physics: Condensed Matter*, 20(26):264014, 2008.

[9] N. Setter and R. Waser. Electroceramic materials. *Acta Materialia*, 48(1):151 – 178, 2000. ISSN 1359-6454. doi: http://dx.doi.org/10.1016/S1359-6454(99)00293-1.

[10] S. A. Wolf, D. D. Awschalom, R. A. Buhrman, J. M. Daughton, S. von Molnr, M. L. Roukes, A. Y. Chtchelkanova, and D. M. Treger. Spintronics: A spin-based electronics vision for the future. *Science*, 294(5546):1488–1495, 2001. doi: 10.1126/science.1065389. URL `http://www.sciencemag.org/content/294/5546/1488.abstract`.

[11] I. Žutić, Jaroslav F., and S. Das Sarma. Spintronics: Fundamentals and applications. *Rev. Mod. Phys.*, 76:323–410, Apr 2004. doi: 10.1103/RevModPhys.76.323.

[12] Scientific background on the nobel prize in physics 2007. URL `http://www.nobelprize.org/nobel_prizes/physics/laureates/2007/advanced-physicsprize2007.pdf`. Accessed May 2015.

[13] J. Nogus and I. K. Schuller. Exchange bias. *Journal of Magnetism and Magnetic Materials*, 192(2):203 – 232, 1999. ISSN 0304-8853. doi: http://dx.doi.org/10.1016/S0304-8853(98)00266-2.

[14] M. Ziese. Extrinsic magnetotransport phenomena in ferromagnetic oxides. *Reports on Progress in Physics*, 65(2):143–249, 2002. doi: 10.1088/0034-4885/65/2/202. cited By 353.

[15] M. Ziese. Study of the micromagnetic structure of a la0.7sr 0.3mno3 film. *Physica Status Solidi (B) Basic Research*, 243(6):1383–1389, 2006. doi: 10.1002/pssb.200541447. cited By 5.

[16] I. Hallsteinsen, E. Folven, F. K. Olsen, R. V. Chopdekar, M. S. Rzchowski, C. B. Eom, J. K. Grepstad, and T. Tybell. Crystalline symmetry controlled magnetic switching in epitaxial (111) la0.7sr0.3mno3 thin films. *APL Materials*, 3(6):062501, 2015. doi: http://dx.doi.org/10.1063/1.4907877.

[17] E. Folven, T. Tybell, A. Scholl, A. Young, S. T. Retterer, Y. Takamura, and J. K. Grepstad. Antiferromagnetic domain reconfiguration in embedded $lafeo_3$ thin film nanostructures. *Nano Letters*, 10(11):4578–4583, 2010. doi: 10.1021/nl1025908. URL `http://dx.doi.org/10.1021/nl1025908`. PMID: 20942384.

[18] Folven E, Takamura Y, and Grepstad J. K. X-peem study of antiferromagnetic domain patterns in lafeo3 thin films and embedded nanostructures. *Journal of Electron Spectroscopy and Related Phenomena*, 185(10):381 – 388, 2012. ISSN 0368-2048. doi: http://dx.doi.org/10.1016/j.elspec.2012.07.001. Photoelectron microscopy, Time resolved pump-probe {PES}.

[19] J. V. Wasvik. Initial growth of $lafeo_3$ on (111)-oriented substrates. Master's thesis, Norwegian University of Science and Technology, June 2013.

[20] I. Hallsteinsen, J.E.a Boschker, M.b Nord, S.c Lee, M.d Rzchowski, P.E.e Vullum, J.K.a Grepstad, R.b Holmestad, C.B.c Eom, and T.a Tybell. Surface stability of epitaxial la0.7sr0.3mno 3 thin films on (111)-oriented srtio3. *Journal of Applied Physics*, 113(18), 2013. doi: 10.1063/1.4804312. cited By 1.

[21] P. C. Hemmer. *Faste Stoffers Fysikk*. Tapir Forlag, 1987.

[22] M. De Graef and M. E. HcHenry. *Structure of Materials*. Cambridge University Press, 2007.

[23] J. Als-Nielsen and D. McMorrow. *Elements of Modern X-ray Physics*. Wiley, 2011. ISBN 9781119970156.

[24] C. Kittel. *Introduction to Solid State Physics*. Wiley, 2004. ISBN 9780471415268.

[25] R. J. D. Tilley. *Crystals and Crystal Structures*. Wiley, 2006. ISBN 9780470029534.

[26] D. B. Williams and B. C. Carter. *Transmission Electron Microscopy, A Textbook for Materials Science*. Springer, 2009. doi: 10.1007/978-0-387-76501-3.

[27] T. Hahn and P. Paufler. *International Tables for Crystallography Vol. A*. Springer, 2005.

[28] J. Nelson. *The Physics of Solar Cells*. Series on Properties of Semiconductor Materials. Imperial College Press, 2003. ISBN 9781860943492.

[29] Y.-M. Kim, J. He, M. D. Biegalski, H. Ambaye, V. Lauter, H. M. Christen, S. T. Pantelides, S. J. Pennycook, S. V. Kalinin, and A. Y. Borisevich. Probing oxygen vacancy concentration and homogeneity in solid-oxide fuel-cell cathode materials on the subunit-cell level. *Nat Mater*, 11:888–894, 2012. doi: doi:10.1038/nmat3393.

[30] J. Singh. *Smart Electronic Materials: Fundamentals and Applications*. Cambridge University Press, 2005. ISBN 9780521850278.

[31] H. F. Kay and P. C. Bailey. Structure and properties of $CaTiO_3$. *Acta Crystallographica*, 10(3):219–226, Mar 1957. doi: 10.1107/S0365110X57000675.

[32] S. Sasaki, C. T. Prewitt, J. D. Bass, and W. A. Schulze. Orthorhombic perovskite $CaTiO_3$ and $CdTiO_3$: structure and space group. *Acta Crystallographica Section C*, 43(9):1668–1674, Sep 1987. doi: 10.1107/S0108270187090620.

[33] A. M. Glazer. The classification of tilted octahedra in perovskites. *Acta Crystallographica Section B*, 28(11):3384–3392, Nov 1972. doi: 10.1107/S0567740872007976.

[34] Y. Wang, F. Guyot, A. Yeganeh-Haeri, and R. C. Liebermann. Twinning in $MgSiO_3$ perovskite. *Science*, 248(4954):468–471, 1990.

[35] Y. Wang and R. C. Liebermann. Electron microscopy study of domain structure due to phase transitions in natural perovskite. *Physics and Chemistry of Minerals*, 20(3): 147–158, 1993. ISSN 0342-1791. doi: 10.1007/BF00200117.

[36] K. Momma and F. Izumi. Visualization for Electronic and STructural Analysis (VESTA), ver. 3.2.1, 2014. URL http://jp-minerals.org/vesta/en/.

[37] S. Geller and E. A. Wood. Crystallographic studies of perovskite-like compounds. I. Rare earth orthoferrites and $YFeO_3$, $YCrO_3$, $YAlO_3$. *Acta Crystallographica*, 9(7): 563–568, Jul 1956. doi: 10.1107/S0365110X56001571.

[38] S. M. Selbach, J. R. Tolchard, A. FFossdal., and T. Grande. Non-linear thermal evolution of the crystal structure and phase transitions of $LaFeO_3$ investigated by high temperature x-ray diffraction. *Journal of Solid State Chemistry*, 196(0):249 – 254, 2012. ISSN 0022-4596. doi: http://dx.doi.org/10.1016/j.jssc.2012.06.023.

[39] V. L. Moruzzi and M. W. Shafer. Phase equilibria in the system la2o3iron oxide in air. *Journal of the American Ceramic Society*, 43(7):367–372, 1960. ISSN 1551-2916. doi: 10.1111/j.1151-2916.1960.tb13673.x.

[40] A. M. Glazer. Simple ways of determining perovskite structures. *Acta Crystallographica Section A*, 31(6):756–762, 1975. ISSN 1600-5724. doi: 10.1107/S0567739475001635.

[41] I. S. Lyubutin, T. V. Dmitrieva, and A. S. Stepin. Dependence of exchange interactions on chemical bond angle in a structural series: Cubic perovskite-rhombic orthoferrite-rhombohedral hematite. *Journal of Experimental and Theoretical Physics*, 88(3):590–597, 1999. ISSN 1063-7761. doi: 10.1134/1.558833.

[42] H. A. Jahn and E. Teller. Stability of polyatomic molecules in degenerate electronic states. i. orbital degeneracy. *Proceedings of the Royal Society of London A: Mathematical, Physical and Engineering Sciences*, 161(905):220–235, 1937. ISSN 0080-4630. doi: 10.1098/rspa.1937.0142.

[43] Evgeny Y. Tsymbal and Elbio R. A. Dagotto and Chang-Beom E. and Ramamoorthy R. *Multifunctional Oxide Heterostructures*. Oxford University Press, 2012. ISBN 13: 9780199584123. doi: 10.1093/acprof:oso/9780199584123.001.0001.

[44] Y. Tokura and N. Nagaosa. Orbital physics in transition-metal oxides. *Science*, 288 (5465):462–468, 2000. doi: 10.1126/science.288.5465.462. URL http://www.sciencemag.org/content/288/5465/462.abstract.

[45] R. L. White. Review of recent work on the magnetic and spectroscopic properties of the rareearth orthoferrites. *Journal of Applied Physics*, 40(3):1061–1069, 1969. doi: http://dx.doi.org/10.1063/1.1657530.

[46] S. Stølen, F. Grønvold, H.Brinks, T. Atake, and H. Mori. Heat capacity and thermodynamic properties of $lafeo_3$ and $lacoo_3$ fromt=13 k tot=1000 k. *The Journal of Chemical Thermodynamics*, 30(3):365 – 377, 1998. ISSN 0021-9614. doi: http://dx.doi.org/10.1006/jcht.1997.0309.

[47] M. Eibschütz, S. Shtrikman, and D. Treves. Mössbauer studies of Fe^{57} in orthoferrites. *Phys. Rev.*, 156:562–577, Apr 1967. doi: 10.1103/PhysRev.156.562.

[48] S. Phokha, S. Pinitsoontorn, S.and Maensiri, and S. Rujirawat. Structure, optical and magnetic properties of $LaFeO_3$ nanoparticles prepared by polymerized complex method. *Journal of Sol-Gel Science and Technology*, 71(2):333–341, 2014. ISSN 0928-0707. doi: 10.1007/s10971-014-3383-8.

[49] J. Lüning, F. Nolting, A. Scholl, H. Ohldag, J. W. Seo, J. Fompeyrine, J.-P. Locquet, and J. Stöhr. Determination of the antiferromagnetic spin axis in epitaxial $LaFeO_3$ films by x-ray magnetic linear dichroism spectroscopy. *Phys. Rev. B*, 67:214433, Jun 2003. doi: 10.1103/PhysRevB.67.214433.

[50] H. Liu, J. Zhu, and D. Xiao. Preparation and characterization of $LaFeO_3$ thin films on (100) $SrTiO_3$ substrates by pulsed laser deposition. *Journal of Advanced Dielectrics*, 01(03):363–367, 2011. doi: 10.1142/S2010135X11000379. URL `http://www.worldscientific.com/doi/abs/10.1142/S2010135X11000379`.

[51] K. J. Choi, M. Biegalski, Y. L. Li, A. Sharan, J. Schubert, R. Uecker, P. Reiche, Y. B. Chen, X. Q. Pan, V. Gopalan, L.-Q. Chen, D. G. Schlom, and C. B. Eom. Enhancement of ferroelectricity in strained batio3 thin films. *Science*, 306(5698):1005–1009, 2004. doi: 10.1126/science.1103218. URL `http://www.sciencemag.org/content/306/5698/1005.abstract`.

[52] J. H. Haeni, P. Irvin, W. Chang, R. Uecker, P. Reiche, Y. L. Li, S. Choudhury, W. Tian, M. E. Hawley, B. Craigo, A. K. Tagantsev, X. Q. Pan, S. K. Streiffer, L. Q. Chen, S. W. Kirchoefer, J. Levy, and D. G. Schlom. Room-temperature ferroelectricity in strained $srtio_3$. *Nature*, 430(7001):758–761, 2004. doi: 10.1038/nature02773.

[53] G. Rupprecht and W. H. Winter. Electromechanical behavior of single-crystal strontium titanate. *Phys. Rev.*, 155:1019–1028, Mar 1967. doi: 10.1103/PhysRev.155.1019.

[54] A. Scholl, J. Sthr, J. Lning, J. W. Seo, J. Fompeyrine, H. Siegwart, J.-P. Locquet, F. Nolting, S. Anders, E. E. Fullerton, M. R. Scheinfein, and H. A. Padmore. Observation of antiferromagnetic domains in epitaxial thin films. *Science*, 287(5455):1014–1016, 2000. doi: 10.1126/science.287.5455.1014. URL `http://www.sciencemag.org/content/287/5455/1014.abstract`.

[55] Y. Wang, F. Guyot, and R. C. Liebermann. Electron microscopy of (Mg, Fe) SiO_3 perovskite: evidence for structural phase transitions and implications for the lower mantle. *Journal of Geophysical Research: Solid Earth (1978–2012)*, 97(B9):12327–12347, 1992.

[56] J. K. Grepstad, Y. Takamura, A. S., I. Hole, Y. Suzuki, and T. Tybell. Effects of thermal annealing in oxygen on the antiferromagnetic order and domain structure of epitaxial $lafeo_3$ thin films. *Thin Solid Films*, 486(12):108 – 112, 2005. ISSN 0040-6090. doi: http://dx.doi.org/10.1016/j.tsf.2004.10.056. WOE-11, 2004 Proceedings of the 11th International Workshop on Oxide Electronics (WOE- 11), Hakone, Japan, October 35, 2004.

[57] Crystalkitx, 9999. URL http://www.totalresolution.com/CrystalKitX.htm.

[58] M. Karlik. Lattice imaging in transmission electron microscopy. *Materials Structure*, 8(1):3–16, 2001.

[59] R.W.G. Wyckoff. *Crystal Structures*. Number v. 1 in Crystal Structures. Wiley, 1963. ISBN 9780470968604.

[60] Mineralogy database. URL http://webmineral.com/. Accessed May 2015.

[61] URL http://en.wikipedia.org/wiki/File:Scheme_TEM_en.svg. Accessed May 2015.

[62] M. Nord, P. E. Vullum, M. Moreau, J. E. Boschker, S. M. Selbach, R. Holmestad, and T. Tybell. Structural phases driven by oxygen vacancies at the la0.7sr0.3mno3/srtio3 hetero-interface. *Applied Physics Letters*, 106(4):041604, 2015. doi: http://dx.doi.org/10.1063/1.4906920.

[63] X-ray data booklet, 2000. URL http://xdb.lbl.gov/.

[64] Andor Technology plc. An introduction to pulsed laser deposition. URL http://www.andor.com/learning-academy/pulsed-laser-deposition-an-introduction-to-pulsed-laser-deposition. Accessed May 2015.

[65] E. Eberg, A. F. Monsen, T. Tybell, A. T. van Helvoort, and R. Holmestad. Comparison of tem specimen preparation of perovskite thin films by tripod polishing and conventional ion milling. *J Electron Microsc (Tokyo)*, 57(6):175–179, 2008. doi: 10.1093/jmicro/dfn018.

[66] Gatan inc., April 2015. URL http://www.gatan.com/products/tem-analysis/gatan-microscopy-suite-software.

[67] S. Czekaj, F. Nolting, L. J. Heyderman, K. Kunze, and M. Krüger. Antiferromagnetic domain configurations in patterned lafeo$_3$ thin films. *Journal of Physics: Condensed Matter*, 19(38):386214, 2007.

[68] J. Gazques, S. Bose, M. Sharma, M. A. Torija, and A. J. Pennycook. Lattice mismatch accomodation via oxygen vacancy ordering in epitaxial $la_{0.5}sr_{0.5}coo_{3-\delta}$ thin films. *APL Mater.*, 1(012105), 2013. doi: 10.1063/1.4809547.

[69] J. M. Zuo and J.C. Mabon. Web-emaps. URL http://emaps.mrl.uiuc.edu/emaps.asp. Accessed May 2015.

Appendix A - AFM and X-ray data

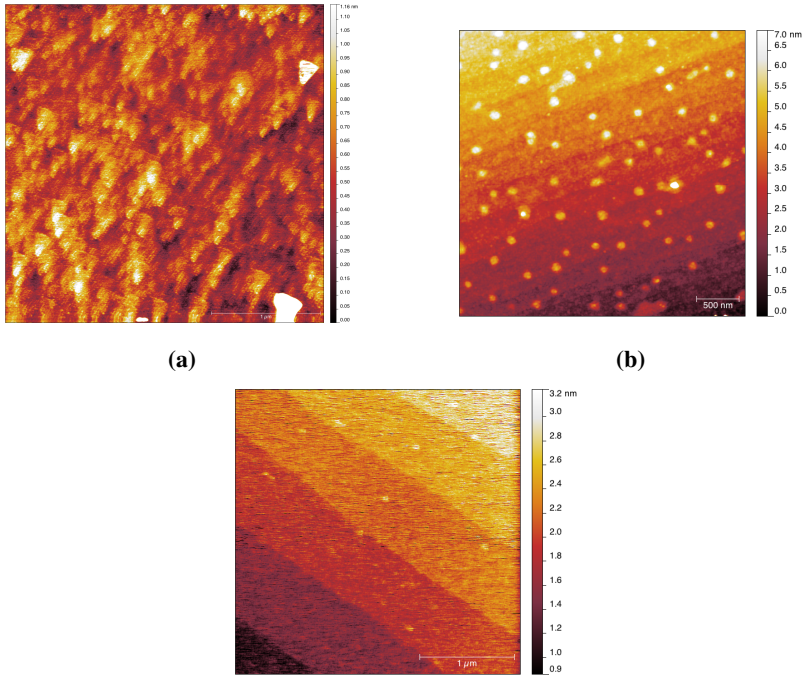

Figure 6.1: Atomic force microscopy data of a) F2 (p40207), b) F3 (p40903), and c) F4 (p41204).

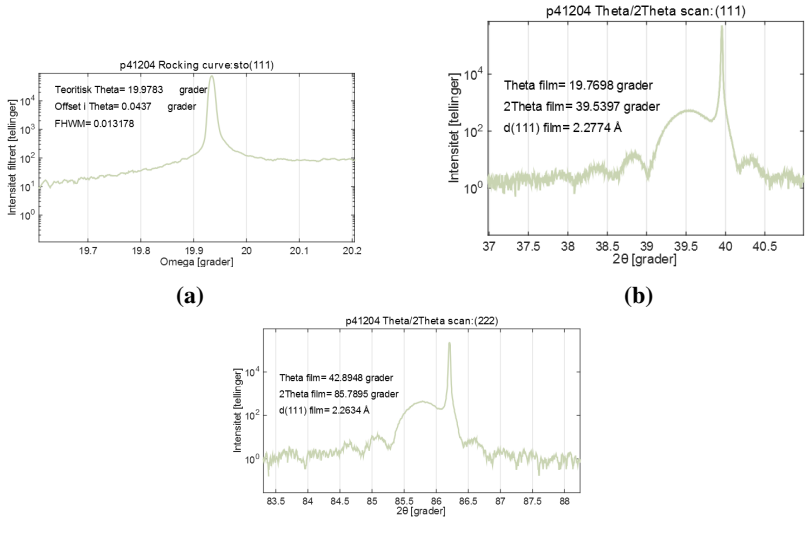

Figure 6.2: XRD data of film F4 (p41204). a) rocking scan of (111) peak. b) θ-2θ scan of (111) peak, and c) θ-2θ scan of (222) peak.

Appendix B - TEM calibrations

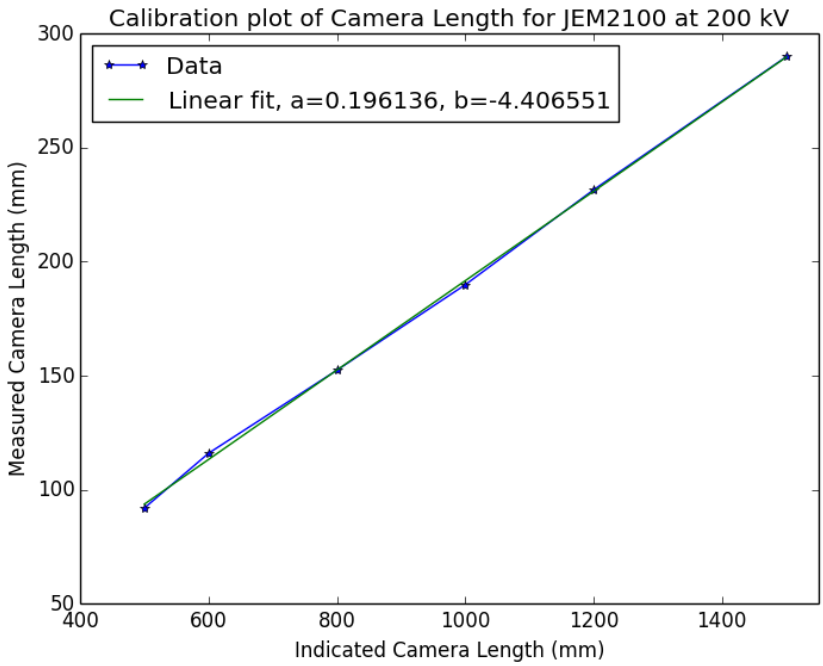

Figure 6.3: Calibration plot of the camera lengths of the 2100 microscope at 200 kV. The calibration sample used was polycrystalline Ag.

Appendix C - Supporting results

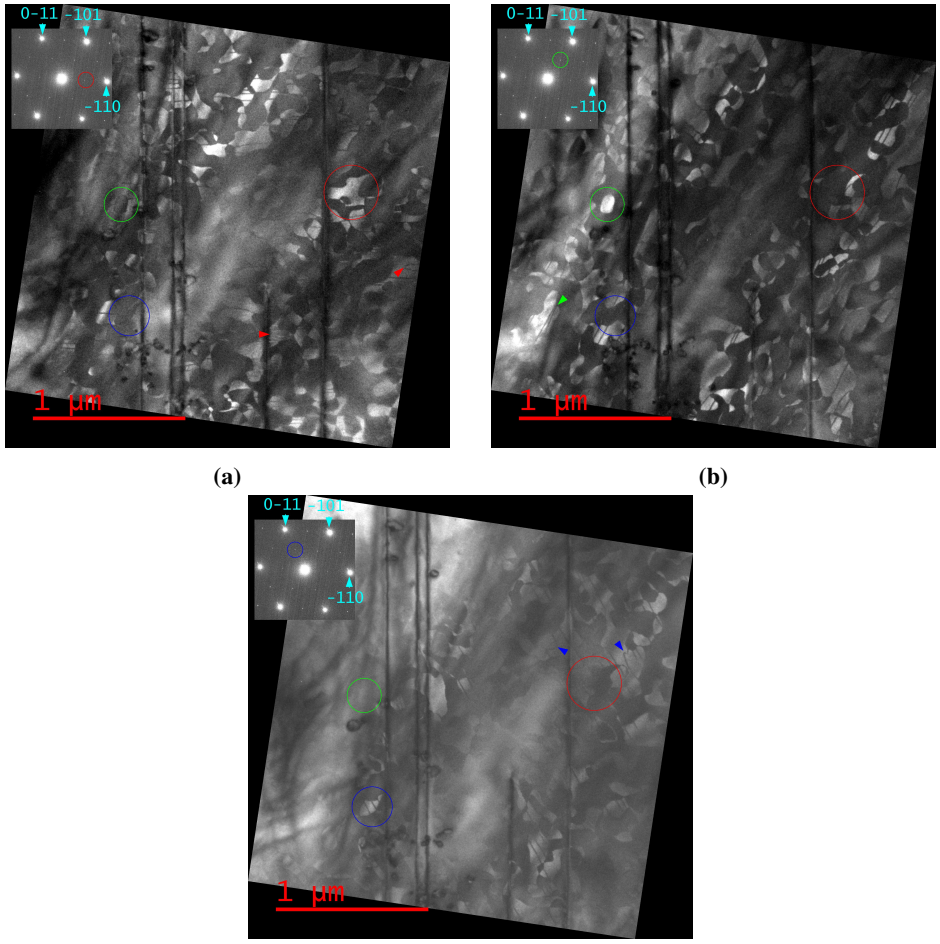

(a) **(b)**

(c)

Figure 6.4: DF series acquired on the 2100F microscope of the same area of F4.3 as the HAADF STEM images in Figs. 4.11a and 4.11b. The blue, green, and red rings mark sharp and easily recognizable domains to aid in the comparison between the different images. Arrowheads are used to mark some interesting features of the dark lines within a domain.

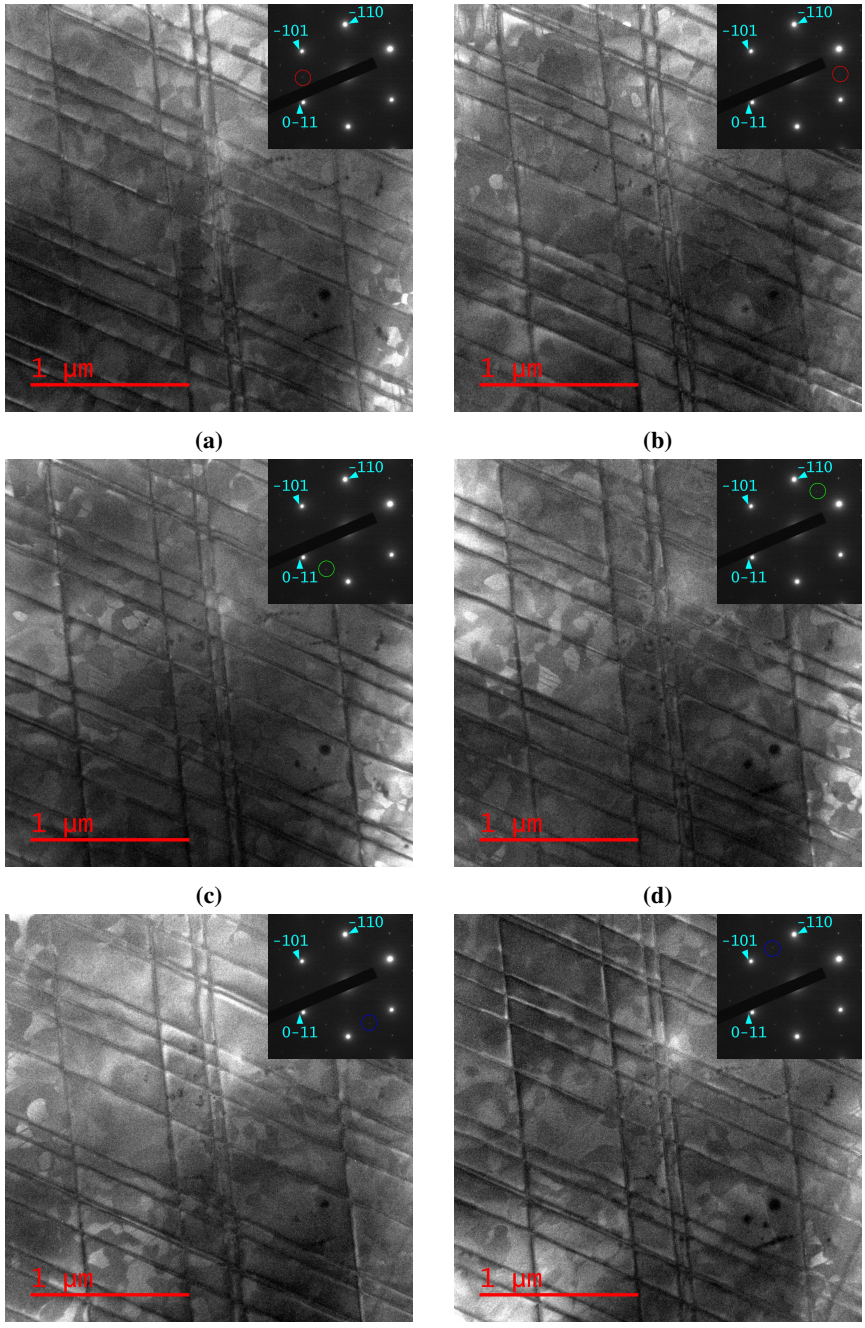

Figure 6.5: DF image series acquired on the 2100F of sample F4.4.

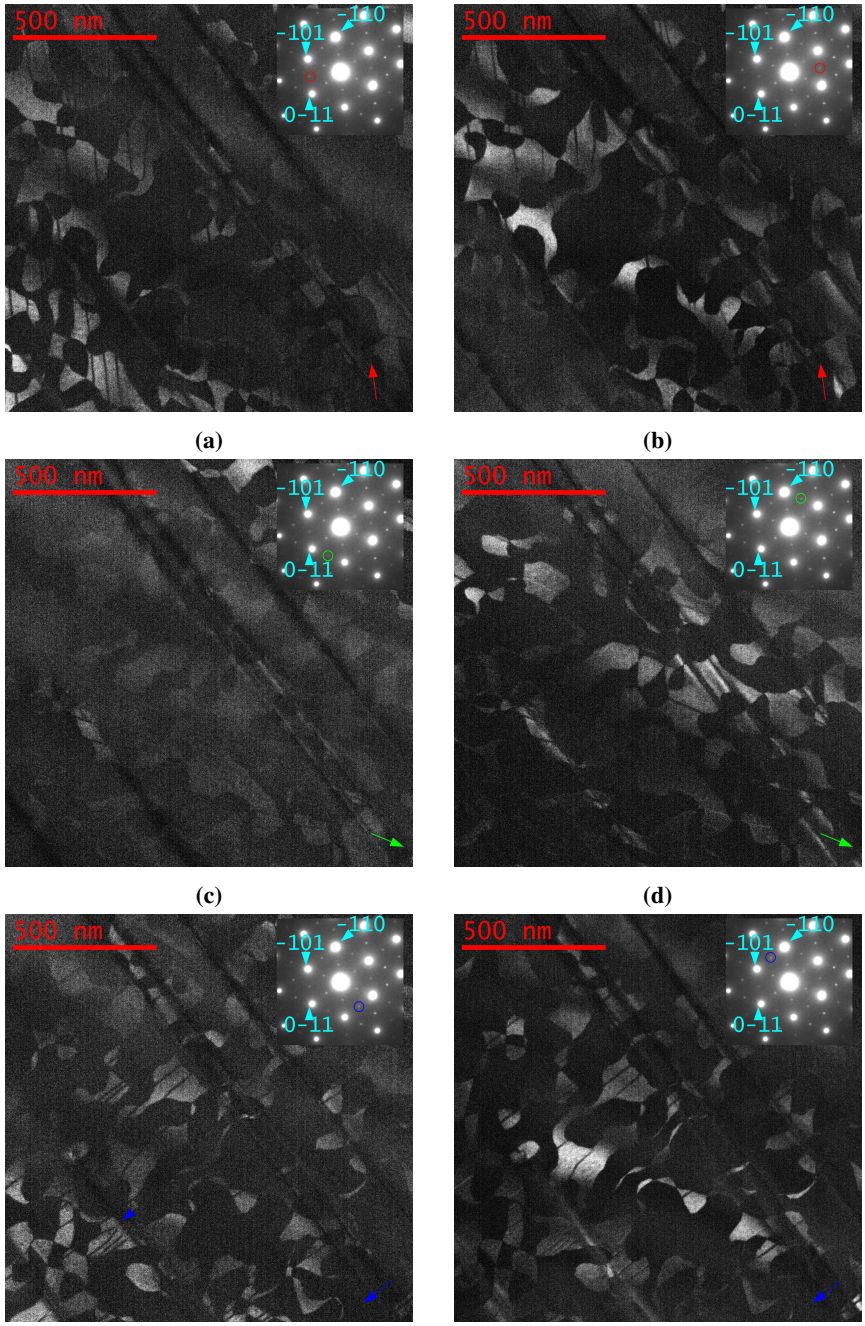

Figure 6.6: DF image series of same area as in Fig. 6.7 acquired on the 2100 using the ”outer” super reflections of LFO. Arrows indicate direction of in-plane unit cell axis, arrowhead mark interesting features.

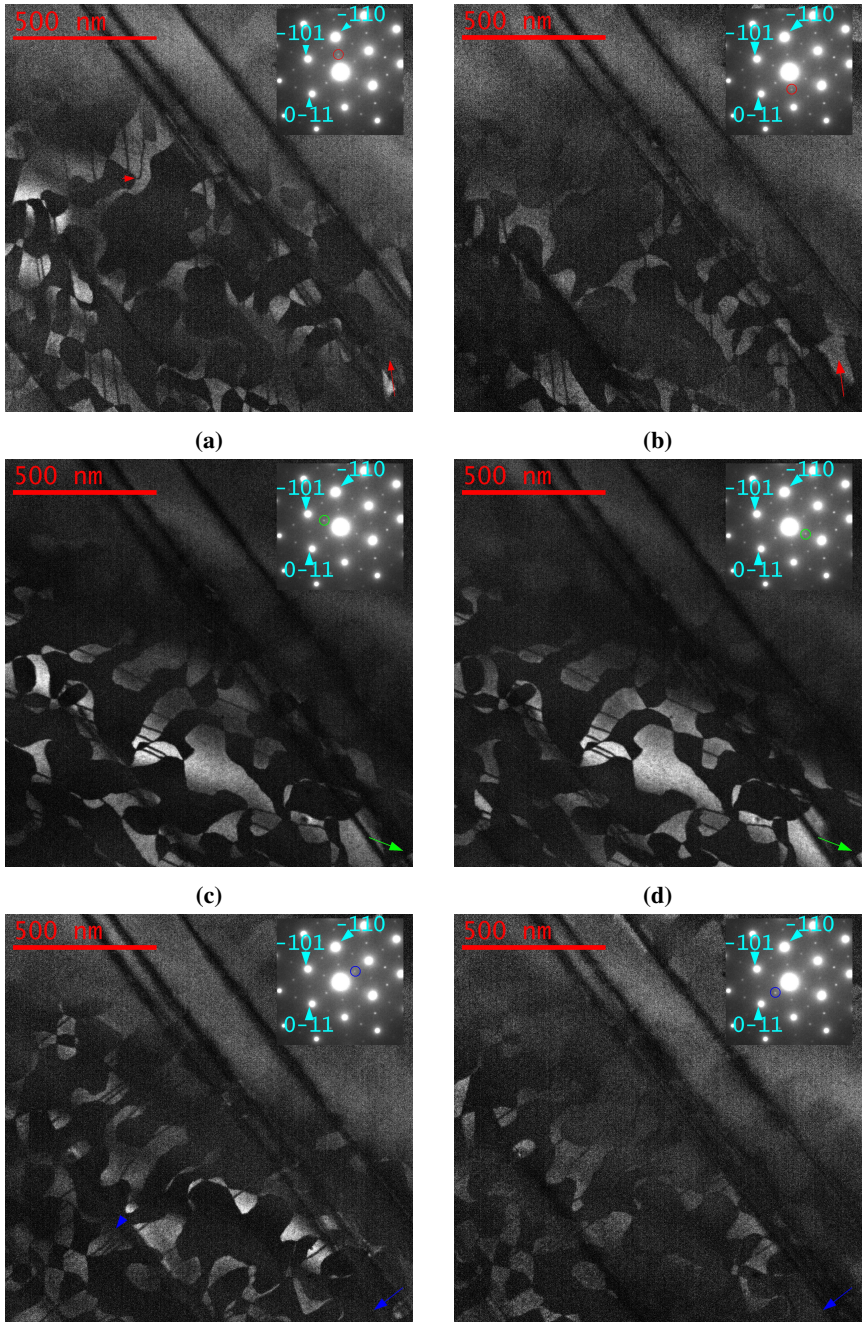

Figure 6.7: TEM DF image series of FIB ditch of F4.3 acquired on the 2100 using the ”inner” super reflections of LFO. Arrows indicate direction of in-plane unit cell axis, arrowhead mark interesting features.

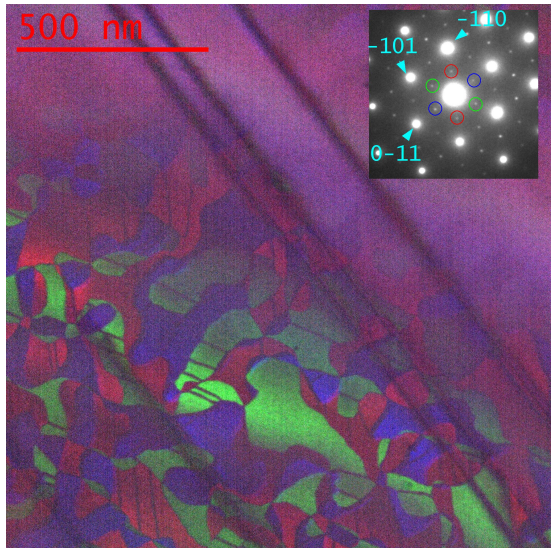

(a)

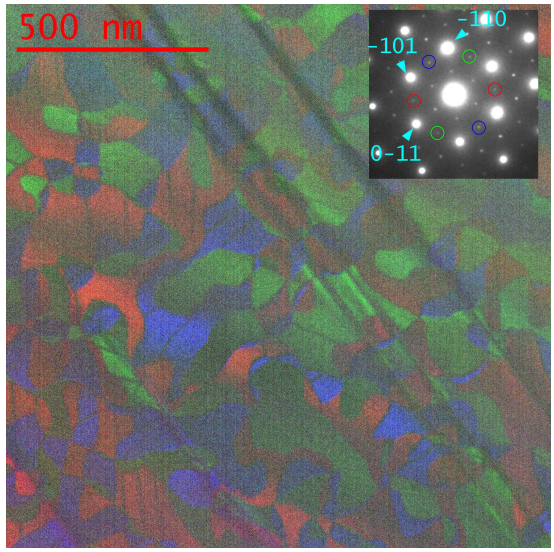

(b)

Figure 6.8: Mosaic of the two different DF image series presented in Figs. 6.7 and 6.6. In a) the mosaic of areas reflecting the inner reflections is presented, while in b) the outer ones are used.This serves to illustrate that the two sets of reflections are equivalent.

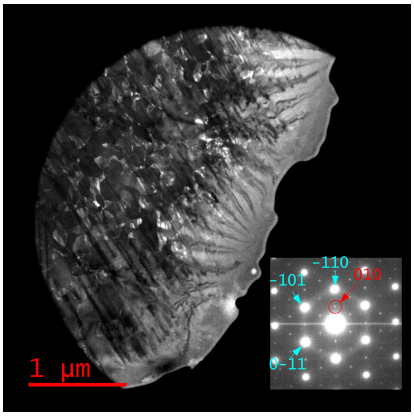

(a) DF image using the first super reflection along $[\bar{1}10]_{STO}$.

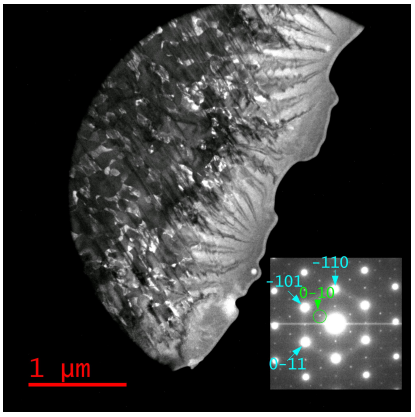

(b) DF image using the first super reflection along $[\bar{1}01]_{STO}$.

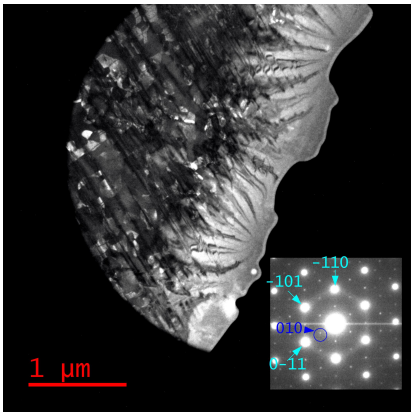

(c) DF image using the first super reflection along $[0\bar{1}1]_{STO}$.

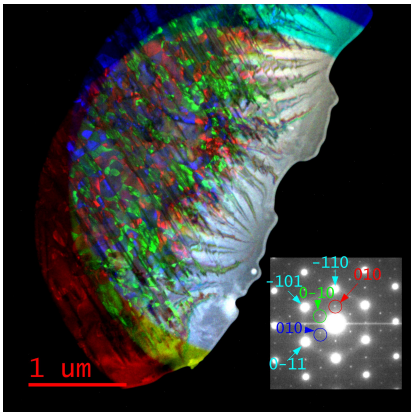

(d) Mosaic of a), b), and c), coloured blue, green, and red respectively.

Figure 6.9: TEM DF image series of the tripod edge of F4.3 acquired on the 2100 microscope. In a), b), and c) DF images using the reflection marked in each inset are presented. The inset has been indexed by applying the assumptions presented in the theory section. A mosaic of all three DF images are shown in d), where blue, green and red refer to the DF images a), b), and c) respectively.

Appendix D - Ruined samples

In this appendix TEM images of ruined samples are presented to show what became of the samples not being discussed in the rest of the thesis. In the case of F2.2 the preparation procedure using ion milling is also given.

F2.2

Sample F2.2 was of very poor quality after tripod polishing. It was too thick, bent and one half of the sandwich at the interface broke off after the first TEM session. Therefore this sample was ion milled by Ar ions in a *Gatan Precision Ion Polishing System* (PIPS) to attempt to thin it further. This is an instrument where a sample mounted on a rotating stage may be bombarded by Ar^+ ions from adjustable angles. Because this will heat the sample the stage may be cooled by liquid nitrogen to prevent thermally induced changes in the sample. For the ion milling of F2.2 the Ar beams were angled 4° from the top and facing the edge of the tripod (single modulation), the sample rotated at 3 RPM, and was cooled by liquid nitrogen during milling. Ion beam accelerating voltages of 3, 2.5, 2.0, and 1.5 keV was used in decreasing steps, each step lasting 1 min.

After inspection in the TEM this sample was still deemed too thick and it was decided to explore the possibility of using the *OXFORD Chemical Assisted Ion Beam Etcher* (CAIBE) at NTNU NanoLab to thin it further. This instrument is usually utilized when uniform etching over large areas are needed. The basic components of the instrument is a sample stage and a neutralized ion beam source. The stage can be set to an angle with respect to the ion beam and to rotate around its surface normal. This will increase the uniformity of the etching. As the etching will increase the temperature of the sample the sample stage can be cooled by a stream of He gas from below. A standardized 4 in wafer is used as a carry-wafer in order to load small samples.

Sample F2.2 was attached to the middle of a 4 in Si carry-wafer with a small piece of 120°C thermal double tape. This wafer was loaded into the CAIBE, where the stage temperature was set to hold 20°C. To achieve a uniform etch the stage was rotated at 20 RPM and had an angle of 30° to the ion beam . The etching itself was done by Ar^+ and used a current, voltage, and accelerator voltage of 500 mA, 500 V, and 300 V respectively for the beam. A neutralizer current of 600 mA was used to keep the ion beam neutral and preserve uniformity. The Si carry-wafer was cooled by He from below. The sample was etched for a total of 1 min.
The images in Fig. 6.10 of sample F2.2 suggest that the sample is too thick for HRTEM to be achieved, even after the sample was ion milled (b). However some slight signs of

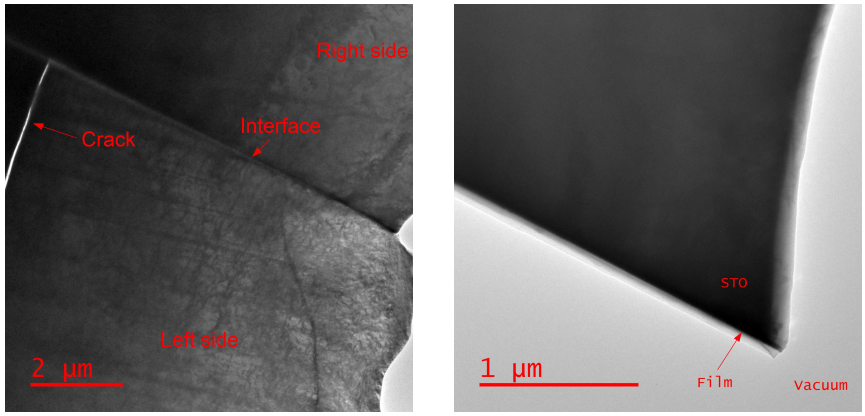

(a) **(b)**

Figure 6.10: TEM images of sample F2.2. The image in (a) is taken right after tripod prep. The sample is much too thick, and one side of the sandwich is cracked and about to fall off (labelled "left side"). After ion milling the sample in the PIPS and CAIBE the sample was still too thick as the image in b) shows. The "left" side has fallen off during the ion milling. This image was acquired almost a year after the PIPS and CAIBE prep.

crystallinity are detected at the very edge (not shown). Away from the ROI the substrate was very thin and HRTEM was possible (not shown). No amorphous surface layers were detected in these thin areas.

From the TEM image presented in Fig. 6.11 it can be gleaned that the apparent thickness of the film is $\approx$ 32 nm. This image is acquired over a year after it had been ion milled in the CAIBE, the sample was plasma cleaned for 20 secs before the TEM experiment. The glue layer is still intact at the tip, even if the other half of the sandwich have fallen off. Because the sample is too thick, as evident by the featureless contrast, no other TEM experiments was conducted on this sample.

It is evident from the images of sample F2.2 that the relatively short ion milling in the PIPS and CAIBE was not enough to thin this sample to electron transparency (see Fig 6.10). The substrate away from the ROI was thin enough for electron transparency and did not contain any amorphous layers. This suggests that the CAIBE may be useful for milling perovskite samples, but more exploration with this instrument is required in order to estimate the milling rate. However it should be mentioned that it is not known how the CAIBE will treat the wedge geometry and if redepostion from the copper grid or the Si carry wafer will occur. Due to the other highly efficient and well tested sample preparation procedures it is not advisable to invest much time and effort in investigating the CAIBE process.

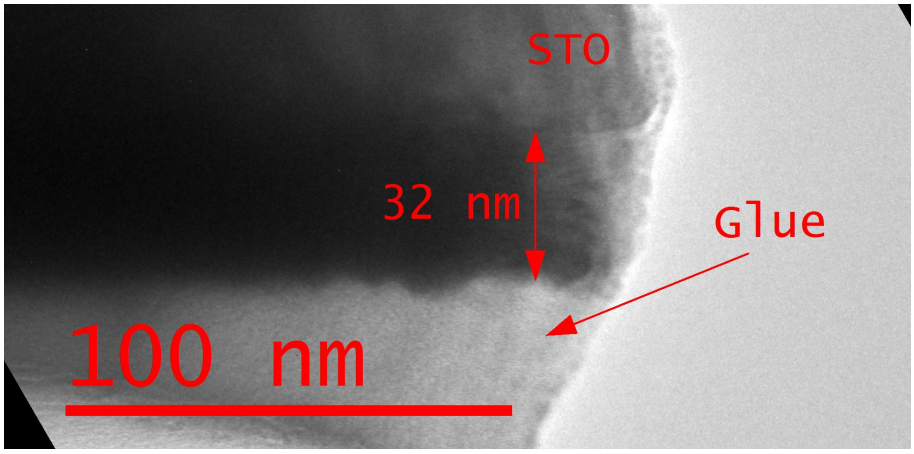

Figure 6.11: TEM image of F2.2 acquired from the 2100F, showing the substrate and what appears to be an $\approx$ 32 nm thick film with an amorphous glue layer at its surface. The sample is very thick as evident by the low contrast.

F4.2

Figure 6.12 show a low-mag TEM image of sample F4.2 where the tip of the sample has broken off. A small ROI is still present. The protective layer is gone from the surface of the film in the thin region probably due to the tip having fallen off. Two TEM images of sample F4.6 is presented in Fig. 6.13 to give an overlook of the sample. In a) it is evident that a large electron transparent region is present, however the top $\approx$ 16 nm part of the film of this region is amorphous as seen in b). Due to the damage to the films in these two samples further studies of these are not performed.

F4.6

The film of sample F4.6 is completely destroyed as evident by Fig. 6.14. An $\approx$ 16 nm thick amorphous layer is present in between the substrate and Pt/Pd and C/Pt protective layers, where the film was expected to be. The substrate is still crystalline with the DP (b) showing no anomalies. The interface between the substrate and what remains of the film appear to be sharp although.

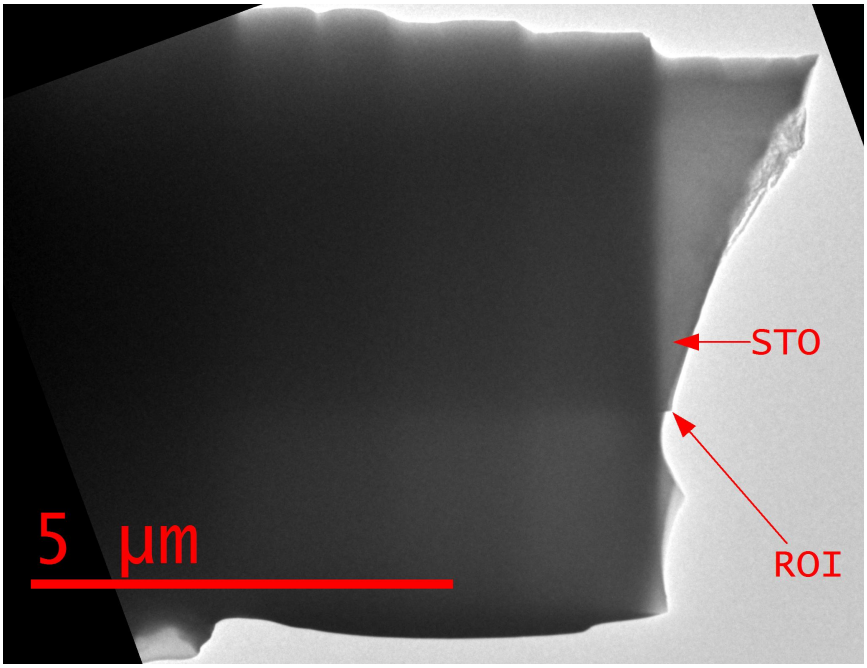

(a)

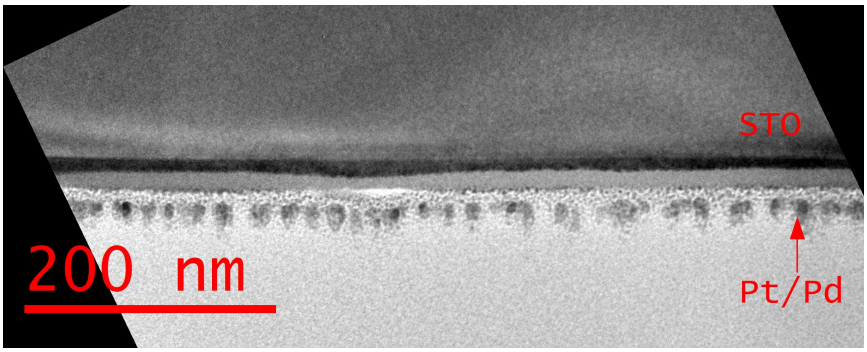

(b)

Figure 6.12: TEM images taken on the 2100 of F4.2. The electron transparent part of the staircase has broken off as a) shows. In b) a TEM image show that after a new area had been prepared the film in this region has become amorphous.

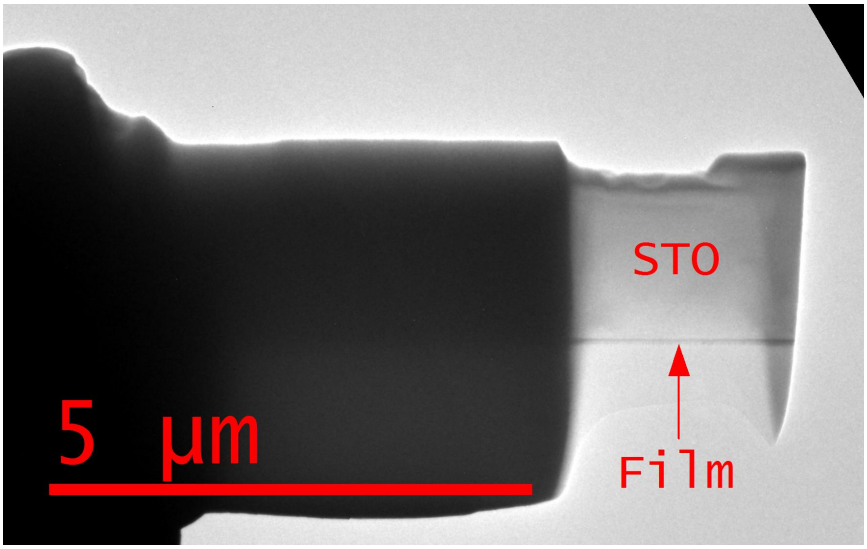

(a)

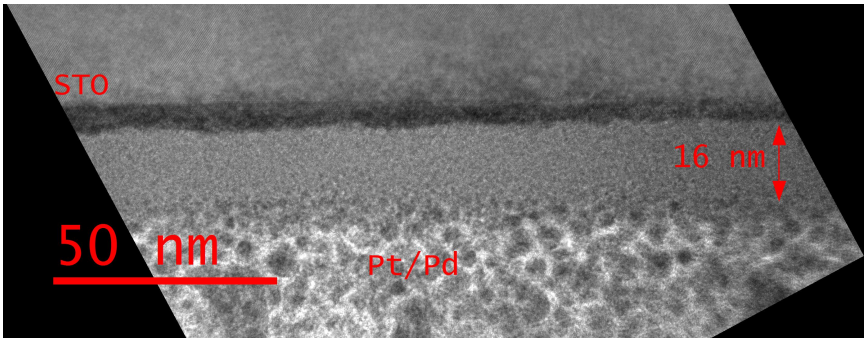

(b)

Figure 6.13: TEM image s taken on the 2100 of F4.6. In a) it is seen that the FIB prep. has made a large electron transparent area. However in b) it is clear that most of the film has become amorphous.

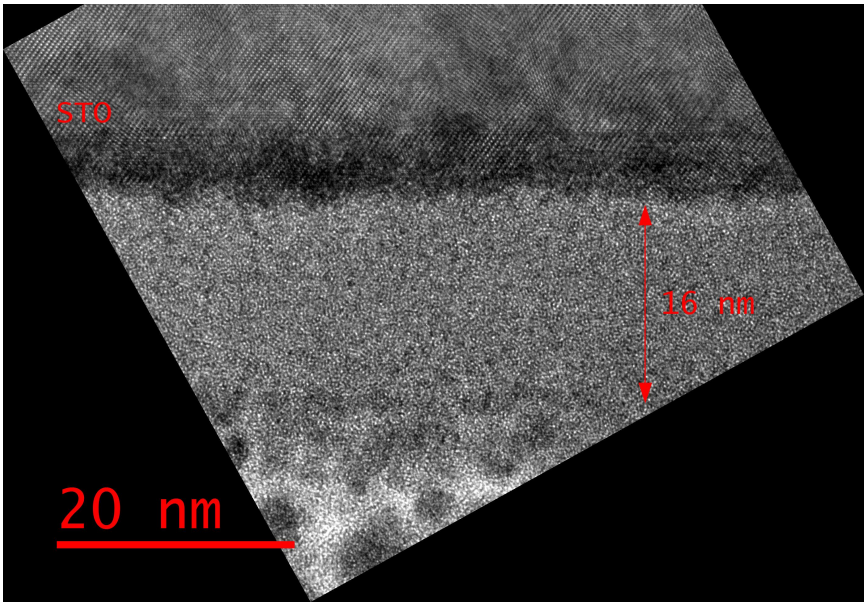

(a)

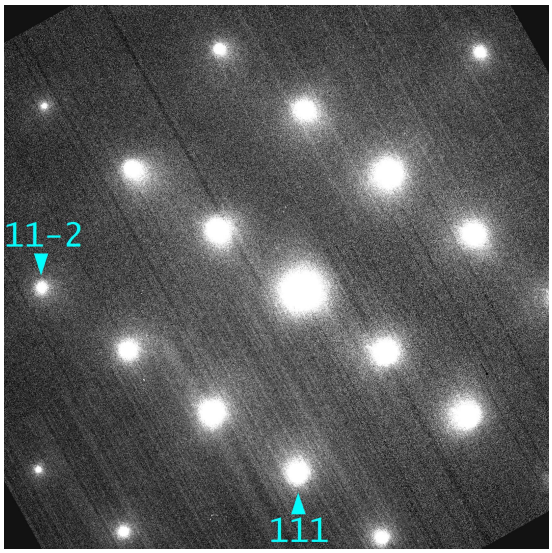

(b)

Figure 6.14: HRTEM image (a) and DP (b) taken on the 2100F of F4.6. The ≈ 16 nm thick film is destroyed, but the substrate remains crystalline. The DP is as expected for STO